# VERIFICATION OF AN ACTIVITY-METHOD APPROACH TO DETERMINE THE $\alpha$-PARTIAL WIDTH OF THE 4.03 MEV STATE IN $^{19}$Ne

By
Spencer Manwell,
B.Sc, University of Guelph

A Thesis
Submitted to the School of Graduate Studies
in Partial Fulfillment of the Requirements
for the Degree
Master of Science

McMaster University

| | |
|---|---|
| MASTER OF SCIENCE (2013) | McMaster University |
| (Physics) | Hamilton, Ontario |

| | |
|---|---|
| TITLE: | Verification of an Activity Method Approach to Determine the $\alpha$-Partial Width of the 4.03 MeV State of $^{19}$Ne |
| AUTHOR: | Spencer Manwell, B.Sc. (University of Guelph) |
| SUPERVISOR: | Professor Alan A. Chen |
| NUMBER OF PAGES: | IX, 101 |

# Abstract

It is well established that the dominating contribution to energy production in stars comes from nuclear reactions. A large portion of a star's lifetime is characterized by the fusion of hydrogen nuclei into helium through various methods. At temperatures above 0.1 GK, helium production is dominated by a series of cyclical nuclear reactions involving carbon, nitrogen, and oxygen. These isotopes are used as catalysts that transform the hydrogen into helium in one of three processes that are referred to as the hot CNO cycles. As temperatures increase within the hydrogen burning region of the star alternative nuclear reactions become energetically allowed. These breakout reaction paths lead to thermonuclear runaway and nucleosynthesis of ions heavier than the A = 20 mass range via the rapid-proton capture (rp) process.

The breakout process is common in many stellar environments and can occur by way of several nuclear reactions. One current topic of discussion is how the rate of the breakout process affects the behaviour of Type I X-ray bursts. Type I X-ray bursts are explosive events that take place on the surface of neutron stars that accrete matter from a nearby binary companion star. The surface of the neutron star becomes a hydrogen rich environment as matter is accreted onto it giving way to hydrogen burning via the HCNO cycles. Once temperatures increase beyond 0.5 GK breakout from the HCNO cycles are thought to be controlled by the $^{15}O(\alpha,\gamma)^{19}Ne$ resonant reaction rate. The breakout then initiates thermonuclear runaway that is observed as explosions at x-ray wavelengths. The star cools afterwards as new

matter is accreted and the burst repeats. The resonant $\alpha$ capture reaction of $^{15}$O proceeds predominately through the 4.03-MeV state at x-ray burst temperatures. Understanding the rate of the breakout step through this energy level in $^{19}$Ne is critical to predicting and modelling the behaviour of these explosive events.

The $^{15}$O($\alpha$,$\gamma$)$^{19}$Ne reaction rate cannot, however, be measured directly in current laboratories. There are no radioactive ion beam facilities capable of producing an $^{15}$O beam with high enough intensity to measure the rate in a feasible amount of time. Experimentalists must then turn to indirect methods of determining the reaction rate. The Breit-Wigner cross section, which depends on the partial decay widths, is needed to determine resonant reaction rates. For this particular reaction the partial $\alpha$ and $\gamma$ decay widths are needed, or similarly the $\alpha$-branching ratio $B_{alpha}$. By populating excited states of $^{19}$Ne of astrophysical importance with various reactions, the decay products can be counted and used to calculate $B_\alpha$. All attempts to date, however, have either been unsuccessful or contained too much uncertainty in their determination of $B_\alpha$ (for the 4.03 MeV state) to provide an $^{15}$O($\alpha$,$\gamma$)$^{19}$Ne reaction rate of sufficient accuracy.

This thesis describes a new experimental approach that has been designed to determine the $\alpha$-branching ratio of the 4.03-MeV excited state of $^{19}$Ne. $B_\alpha$ will be measured by the detection of the $\beta^+$ activity of the associated $\alpha$-decay product. This activity method has been modelled using two separate simulations. The first, a Monte Carlo code to simulate the reaction process and energy distributions of the decay products. Secondly, a GEANT4 simulation was created to predict the detector response to the $^{15}$O $\beta+$ activity. Along with the simulations two NaI(Tl) detectors, which were customized to this experiment's geometric constraints, have been tested and their response and resolution have been determined. The results of this work will be used to refine the experimental setup such that the proposed test run and eventual $B_\alpha$ measurement of the 4.03-MeV state will be successful. With the results of the simulations and subsequent yield calculations, it has been found that reasonable statistical significance in the $^{15}$O yield from the 4.03-MeV excited state in $^{19}$Ne can be achieved within 10 days of beamtime.

*To My Family.*
*Hopefully this explains what I have*
*been doing for the past two years.*

# Acknowledgments

There are many individuals that deserve mention who have provided me with help and support throughout this process. I am afraid that a simple acknowledgement will not convey my sincere appreciation to these people, but I will try nevertheless.

I would primarily like to express my thanks to my supervisor, Dr. Alan Chen, who agreed to take me on as a graduate student and has given extensive guidance, support, and reassurance throughout my degree. The extent to which you engaged in my project and learning was incredible, and I could not have asked for a better supervisor to work with. I would also like to thank my office mates: Kiana Setoodehnia, and Dan Irvine, for sharing their knowledge and experiences with me, in many forms that are certainly not limited to this thesis. So to address all the members of my research group, thank you for your friendship and encouragement during our time together.

A note of appreciation is also deserved to my fellow graduate students at McMaster University. Being able to share this time with you has certainly made this experience much more enjoyable and rewarding. I simply hope that I have impacted your lives here in the same way you have mine.

I would like to extend my thanks to two of our research collaborators; Dr. Anuj Parikh, and Dr. Richard Longland, with whom I was fortunate enough to meet and learn from. Sharing conversations with you both have certainly helped guide me in my life and career goals for the future.

To my family, I must extend a deep and sincere thank you. You all have always encouraged me in choosing my own path and have always supported me in my endeavours. Much of who am I today is the result of your love and support, thank you for everything.

Finally, I want to thank Robyn and Charlee, without you my life would be inconceivably different. Thank you for your ongoing love and support, and for giving me a much needed escape from work and school. My experience and memories of this stage in my life will forever be bettered for having you in them.

# Table of Contents

# List of Figures

# List of Tables

Chapter 1

# Introduction

The dark lines that appeared in Fraunhofer's spectrum of the sun gave, for the first time, a means of comparing the chemical composition of stars in the universe [1]. The ability to show that these goliaths of legend and myth are actually composed of so many of the same materials that allow life on Earth to exist is, in my humble opinion, nothing short of astounding.

In an address made in 1920 at Cardiff University by Sir Arthur Eddington titled *The Internal Constituents of Stars*, Eddington spoke fiercely about the role that the "transmutation" of atoms must undoubtedly play in the energy production of stars. He discussed recent work by Sir Ernest Rutherford involving isotopes and nuclear reactions and said that,

> "Sir Ernest Rutherford has recently been breaking down the atoms of oxygen and nitrogen, driving out an isotope of helium from them; and what is possible in the Cavendish laboratory may not be too difficult in the Sun."

Within this comment Eddington facetiously regards the ability of Rutherford to fuse atoms together as comparable to that of the Sun's. He goes on to remark that

stars must, in fact, be the cauldrons in which the universe "cooks" the atoms that are found everywhere in the universe. The idea that thermonuclear reactions are the primary means by which stars produce energy led to the formation of the field of Nuclear Astrophysics. This field is defined by the pursuit of knowledge related to how nuclear structure and interactions affect the behaviour and lifetimes of stars. In this chapter, the role of stellar nuclear reactions and nucleosynthesis will be discussed to provide the framework that motivated this project.

## 1.1 Nuclear Astrophysics

At around the time of Eddington's 1920 address, it was commonly believed that the source of a star's energy production was in contraction and the release of its gravitational energy [2], a process which is governed by the Virial Theorem [3]. This notion, although very popular, predicted that the Sun was approximately 20 million years old. Eddington spoke out strongly about not clinging to convention for tradition's sake and discussed how the energy released from the fusion of hydrogen into helium within the Sun would be able to sustain its output for 15 billion years, an estimate much closer to its actual age [4]. The acceptance of the nuclear description of stellar energy production was driven by the isotope mass measurements of F. W. Aston and how the mass of of a helium nucleus was less than the summed mass of the nucleons that must form it[5]. This discrepancy in mass, explained by a release in energy, provided a means through which stars could generate heat.

Since 1920, nuclear research has been closely linked to astrophysics as nuclear physics provided a theoretical framework with which stellar observations, like energy production and elemental abundances, could be explained. To motivate the proposed experiment of this project, the essential mechanisms involved in the energy production and nucleosynthesis in x-ray bursts will be discussed. In the following sections, some relevant information regarding reaction rate calculations, and previous measurements of the specific $\alpha$-branching ratio, which is needed for the $^{15}\mathrm{O}(\alpha,\gamma)^{19}\mathrm{Ne}$ reaction rate calculation, will also be given.

### 1.1.1 Energy Production in Stars

The nuclear reaction mechanisms through which main sequence stars generate energy were first laid out in Hans Bethe's *Energy Production in Stars* [6]. In this article the beginnings of many nuclear processes and burning mechanisms were described. This comprehensive list of nuclear reactions includes many fusion processes involving hydrogen, helium, carbon, nitrogen, and oxygen [7, 8]. Several of these mechanisms will aid in the following description of the astronomical events, Type I x-ray bursts, that are significant to this project. To this end, a description of the hot Carbon-Nitrogen-Oxygen (HCNO) cycles , the triple-alpha process, and the rapid-proton capture (rp) process will be given.

**The Hot CNO Cycles**

For stars with sufficient abundances of carbon, nitrogen, and oxygen in regions where the temperature is between 0.1 and 0.4 GK (1 GK = $10^9$ K), the energy production is dominated by the HCNO cycles. There are three distinct HCNO cycles that have several commonalities. All three processes convert four hydrogen nuclei in to one helium nucleus, use CNOF material as catalysts, and display temperature independent energy production [9]. Energy production via HCNO cycles is only sensitive to the abundances of the catalyst materials [10].

The HCNO cycles are considered to be $\beta$-limited, as their energy production rates are constrained by the $\beta$-decay lifetimes of the $^{14}$O, $^{15}$O and $^{17}$F waiting points. The oxygen waiting points do not have competing proton-capture reaction channels as $^{15}$F and $^{16}$F nuclei are unstable via proton emission [9] and must await greater temperatures for faster alternatives to become available. As temperatures increases beyond 0.4 GK CNO abundances can be lost through various breakout reactions. The lowest temperature breakout, which is of primary concern to this project, is the $^{15}$O($\alpha$,$\gamma$)$^{19}$Ne reaction. As reference, a map of the three HCNO cycles is given in Figure 1.1.

**The Triple-$\alpha$ Process**

As hydrogen is consumed within the star the energy production from hydrogen burning becomes insufficient to produce the pressure needed to sustain collapse.

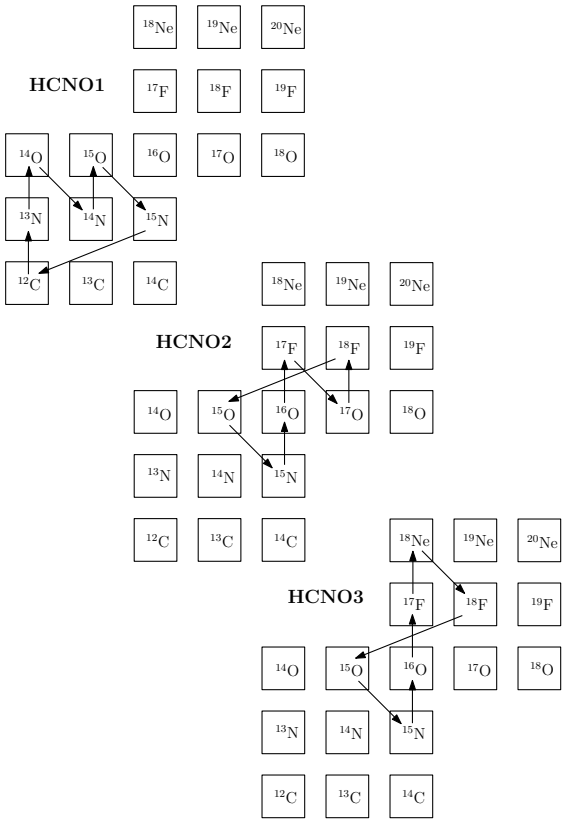


Figure 1.1: Reaction processes included in the three HCNO cycles.

As stars contract and release gravitational energy, the internal temperatures and densities become large enough to allow helium burning processes to proceed [9].

Helium becomes the new fuel for which the star may produce energy and prevent further collapse. There is a two-step process through which helium nuclei are fused into $^{12}$C and release energy [11]. The helium burning reactions are given below.

$$^4He \; + \; ^4He \rightarrow \; ^8Be, \quad Q \; = \; -92 \; keV$$

$$^4He \; + \; ^8Be \rightarrow \; ^{12}C \; + \; \gamma, \quad Q \; = \; 7400 \; keV$$

As the intermediate $^8$Be nucleus is unstable it will decay into two $\alpha$ particles with a half-life of $6.7 \cdot 10^{-17}$ s. As this initial step becomes more frequent the production and decay rate of $^8$Be balance and small abundances exist that allow the second step to proceed. The triple-$\alpha$ process is responsible for generating much of the carbon used in the HCNO cycles. As well, further $\alpha$ capture reactions take place

that can produce $^{16}$O, $^{20}$Ne and $^{24}$Mg. These become less likely, however, as the increased proton number also increases the Coulomb barrier that resists the subsequent capture of positively charged $\alpha$ particles [9].

**The rp - Process**

The rapid-proton-capture (rp) process was originally defined by Wallace and Woosley in 1981. This process was proposed to describe explosive hydrogen burning in novae, super-massive stars and x-ray bursts [12]. The rp-process consists of a complicated network of proton capture reactions (p,$\gamma$) and $\beta^+$ decays. The series of rapid proton capture reactions stem from breakout reactions from the HCNO cycles and lead mass-abundance flows away from the valley of stability towards the proton drip line. Along the proton drip line further proton captures are unfavourable and compete with $\beta^+$ decays to allow further proton captures to proceed. The unfavourability of (p,$\gamma$) reactions are due to negative Q-values, unstable nuclei that have very short $\beta$ decay lifetimes, or the fact that if the occur they are quickly followed by photo-disintegrations.

It was found that the rp-process would result in a much larger energy production rate than the HCNO cycles in hydrogen-rich environments at temperatures of $\sim$ 1 GK [12]. This work also showed that the rp-process was capable of sufficient energy production at the relevant time scales to be able to generate x-ray bursting behaviour on neutron stars that accrete matter in a close binary system. This latter feature is specifically relevant to this project and will be discussed further in Section 1.1.2.

### 1.1.2 Type I X-ray Bursts

X-ray bursts were discovered in 1975, although other x-ray bursters had been observed previously but had not been distinguished as unique x-ray sources [13]. X-ray bursts are characterized by sharp, periodic increases in the luminosity of stellar x-ray sources. These explosive events are the most frequent kind of thermonuclear stellar explosion in the Galaxy and the third most energetic, following supernovae and classical novae [14]. Type I x-ray bursts occur in close binary systems in which a compact neutron star accretes hydrogen- and helium-rich material from a low mass

companion star. Companion stars are typically low-mass main sequence or red giant stars [15].

Soon after the discovery of x-ray bursts, other bursting sources (e.g., the Rapid Burster - MXB 1730-335) were discovered that displayed a much more rapid bursting recurrence time. As these explosive events did not appear to be driven by the same processes a distinction was made between typical x-ray bursts (Type I) and those that are more rapid (Type II x-ray bursts). Of these two classes, the following discussion will include the former - Type I x-ray bursts - as the latter have bursting mechanisms that are not relevant to this project. Typical bursting behaviour for Type I x-ray bursts includes luminosity peaks and rise times of $10^{38}$ erg·s$^{-1}$ and $\sim$ 1 - 10 s [14], i.e., luminosities that are approximately five orders of magnitude greater than the solar luminosity. Following the fast increase in luminosity during the explosion, the energy output decreases slowly to the quiescent rate in a time that ranges from 10 s to several minutes. The period of explosions, while depending on many variables like H/He abundance and accretion rate, range from one to several hours [13].

Type I x-ray bursts are believed to arise as a result of unstable thermonuclear runaway in the thin shell of accreted matter in the surface of a compact neutron star [14]. This idea was first theorized by Maraschi and Cavaliere [16] and Woosley and Taam [17]. As hydrogen and helium are accreted onto the surface of the neutron star the density and temperature of the thin layer increase. This accreted envelope becomes weakly electron degenerate and is not capable of expansion to maintain temperature [13], and as a result densities and temperatures increase to $\sim 10^6$ g·cm$^{-1}$ and $\sim 10^9$ K, respectively. With such high temperature and density conditions, nuclear burning ignites. This is exhibited primarily by the Triple-$\alpha$ process and the slow, hot CNO cycles. Energy production on the neutron star is dominated by the hot CNO cycles as they are preferred over reaction processes with slower $\beta$-decay waiting in higher temperature environments [18]. With stable nuclear burning of hydrogen and helium the temperature within the envelope continues to increase until a critical point where breakout from the hot CNO cycles occurs [10]. The breakout reactions from the hot CNO cycles that drive mass-abundance flows out of the A $< 20$ region are the $^{15}$O($\alpha$,$\gamma$)$^{19}$Ne and $^{18}$Ne($\alpha$,$p$)$^{21}$Na reactions. The former

dominates the breakout process for lower temperatures ($\lesssim$ 0.6 GK) [19] and thus has a larger effect on the hydrogen abundance at the commencement of the burst. This early control over the hydrogen mass fraction implies this reaction also has a strong influence over the bursting behaviours, recurrence times, and nucleosynthesis end point [15].

The breakout reaction, i.e., the $^{15}$O($\alpha$,$\gamma$)$^{19}$Ne reaction, acts as a funnel or gateway through which abundance flows must pass into the rp-process. The rp-process, as described in Section 1.1.1, is the dominant energy production mechanism that produces the unstable H-burning and intense x-ray emission that characterize Type I x-ray bursts. Along with some interplay with the Triple-$\alpha$ process and the $\alpha p$-process, the rp-process drives abundance flows and nucleosynthesis beyond the A = 20 range far from the valley of stability and toward the proton drip line. The end point of nucleosynthesis is thought to be in the SnSbTe-mass range [14], although the end point remains a topic of much discussion [20]. The end point is brought about by the depletion of hydrogen fuel: as the abundance flow approaches the nucleosynthesis end point, subsequent proton capture reactions dwindle as the hydrogen fuel is all but spent. The slow, exponential decay-like, decline in the x-ray burst luminosity is driven by $\beta^+$ decays of the nuclear ashes [14].

The nucleosynthesis of x-ray bursts are not believed to contribute to galactic abundance of heavy nuclei as the escape velocity of neutron stars is too great [14]. The remaining nuclear ashes of the rp-process are thought to sink to the neutron star surface, or crust, and are then covered and compressed by new accreted material. The x-ray burst may then repeat once favourable conditions are met once again. The current hydrodynamic models of the nuclear reaction and abundance flows that are performed to model x-ray burst behaviour rely on the nuclear data of hundreds of nuclides and thousands of nuclear reactions [13]. The reaction rate data used in many of these studies are based on highly uncertain theoretical predictions or measurements[14]. Therefore, it is very important to further constrain the uncertainty in these input parameters through precise experimental measurement. To this end, this thesis presents a description of a novel measurement technique that has been designed to measure the $\alpha$-branching ratio of the 4.035-MeV excited state in $^{19}$Ne, which is thought to be the dominant resonance involved in the $^{15}$O($\alpha$,$\gamma$)$^{19}$Ne

breakout reaction. The $\alpha$-branching ratio of this particular level has been a topic of much research [21, 22, 23, 24, 25, 26] for nearly 25 years, but until recently [26] only experimental upper limits have been reported. As such, more experimental work is needed to measure this quantity with greater precision [27]. The previous results of this measurement will be discussed in greater detail in Section 1.3, but before this a treatment of the resonant reaction rate formalism will be given in the following section to motivate the significance of a measurement of the $\alpha$-branching ratio of the excited state of interest in $^{19}$Ne.

## 1.2 Resonant Reaction Rates

The nuclear structure parameters within the equations that are used to describe reaction rates in stellar environments drive much of the experimental efforts in nuclear astrophysics. A brief treatment of the reaction rate formalism, particularly in the case of resonant reaction rates, is given here to motivate the experimental measurement that is the subject of this project.

Within stellar environments the reaction rate between two nuclei is described by the product of the number densities of the nuclei involved, the probabilistic cross section for having the reaction occur, and the relative velocity of the two nuclei. The relative velocities of nuclei within stars is described by the thermal Maxwell-Boltzmann (MB) distribution $P(v)$. For the reaction $0 + 1 \rightarrow 2 + 3$, the reaction rate definition is given as,

$$r_{01} = N_0 N_1 \sigma(v) v. \tag{1.1}$$

The probability of an ion pair having a relative velocity between $v$ and $v+dv$ is given by $P(v)dv$. Averaging over the distribution of velocities gives the mean reaction rate per ion pair,

$$< \sigma v >_{01} = \int v P(v) \sigma(v) dv. \tag{1.2}$$

The MB distribution has the following velocity-dependent form,

$$P(v)dv = \left(\frac{m_{01}}{2\pi kT}\right)^{3/2} e^{-m_{01}v^2/2kT} 4\pi v^2 dv \tag{1.3}$$

where $m_{01}$ represents the reduced mass of the 0 + 1 system, $k$ is the Boltzmann constant, and $T$ is the temperature. This expression applies to the case where the nuclei in the star are non-relativistic and non-degenerate. By expressing the velocities in Eq. 1.3 in terms of the relative kinetic energies between the nuclei in the centre-of-mass frame a more convenient energy-dependent MB distribution can be derived. With $E = m_{01}v^2/2$ and $dE/dv = m_{01}v$ one can see that,

$$P(E)dE = \frac{2}{\sqrt{\pi}} \frac{1}{(kT)^{3/2}} \sqrt{E} e^{-E/kT} dE. \tag{1.4}$$

Recasting Eq. 1.2 in terms of energy gives then the reaction rate per ion pair that is explicitly dependent on the relative kinetic energies between the reaction products,

$$< \sigma v >_{01} = \left(\frac{8}{\pi m_{01}}\right)^{1/2} \frac{1}{(kT)^{3/2}} \int E\sigma(E) e^{-E/kT} dE \tag{1.5}$$

To better understand the physical parameters involved in the reaction rate calculations, a functional form of the cross section must be included. In general, the cross section contains the nuclear structure information that describes the overlap in wavefunctions of the two reaction products. At typical temperatures related to the breakout from the HCNO cycles the total reaction rate of the $^{15}$O($\alpha$,$\gamma$)$^{19}$Ne reaction is dominated by contributions from resonant reactions that populate excited states in $^{19}$Ne that just lie above the $\alpha$-decay threshold. To a good approximation the reaction rate can be calculated by ignoring the non-resonant contributions and employing only the resonant rate formalism [12]. To this end, the one-level Breit-Wigner cross section, Eq. 1.6, is implemented here:

$$\sigma_{BW} = \frac{\lambda^2}{4\pi} \frac{(2J+1)(1+\delta_{01})}{(2j_0+1)(2j_1+1)} \frac{\Gamma_0\Gamma_2}{(E_r - E)^2 + \Gamma^2/4} \tag{1.6}$$

For clarity, the definitions of the variables included in Eq. 1.6 are listed below.

- $\lambda$ represents the de Broglie wavelength of the 0 and 1 nuclei in the entrance channel.

- $J$, $j_0$, and $j_1$ represent the spins of the compound nucleus 0 + 1, the projectile 0, and the target nucleus 1, respectively.
- The $(1+\delta_{01})$ term is included to generalize the expression for identical particles in the entrance channel, 0 and 1 in this case.
- $\Gamma_i$ represent the partial decay widths in the entrance and exit channels.
- $\Gamma$ represents the total decay width of the excited compound nucleus, and
- $E_r$ and $E$ give the resonance energy and the relative 0 + 1 energy in the centre-of-mass frame, respectively.

Turning back to Eq. 1.5, by rewriting the de Broglie wavelength as $2\pi\hbar/\sqrt{2m_{01}E}$ and substituting Eq. 1.6 for $\sigma$ we arrive at the definition of the contribution to the reaction rate per ion pair of a single resonance corresponding to the resonance energy $E_r$ in the compound nucleus 0 + 1.

$$< \sigma v >_{01} = \frac{\sqrt{2\pi}\hbar^2}{(m_{01}kT)^{3/2}}\,\omega \int \frac{\Gamma_0\Gamma_2}{(E_r - E)^2 + \Gamma^2/4} e^{-E/kT} dE \tag{1.7}$$

where,

$$\omega = \frac{(2J+1)(1+\delta_{01})}{(2j_0+1)(2j_1+1)} \tag{1.8}$$

When considering narrow resonances, i.e. $\Gamma < 0.1E_r$, several assumptions can be made to solve the integral of Eq. 1.7 analytically. First, it is assumed that all resonances are isolated and do not overlap and second, the partial widths do not vary appreciably over the range of energy in which they are non-zero. With these assumptions the decay widths are taken as constant and can be removed from the integral; similarly the MB factor can be evaluated at the resonance energy $E_r$ as all other values of $E$ will not contribute to the integration. The integral is left in the form of a Lorentzian integral which has a known solution. The result is the following,

$$< \sigma v >_{01} = \left(\frac{2\pi}{m_{01}kT}\right)^{3/2} \hbar^2 e^{-E_r/kT} \omega\gamma \tag{1.9}$$

The term $\omega\gamma$ is commonly referred to as the resonance strength due to the fact that this quantity is directly related to the area under the resonance cross section. This

can be demonstrated to be the product between the maximum cross section and the total width of the resonance [9],

$$\Gamma\sigma(E = E_r) = \Gamma\frac{\lambda^2}{\pi}\omega\frac{\Gamma_0\Gamma_2}{\Gamma^2} = \frac{\lambda^2}{\pi}\omega\gamma \tag{1.10}$$

The determination of the resonance strength for the 4.03-MeV excited state resonance in $^{19}$Ne is the end goal of this project. To do this one requires the spins of the particles in the entrance channel as well as the compound nucleus and measured values of the partial and total widths for the state. It is often the case however that more than one resonance is produced within the relevant stellar energy regime, referred to as the Gamow window. The resonances that are found in this region will provide the greatest contribution to the total reaction rate. For isolated narrow resonances, as was assumed previously, the reaction rate can be calculated by the incoherent addition of the individual resonance strengths; this is shown by Eq. 1.11.

$$< \sigma v >_{01} = \left(\frac{2\pi}{m_{01}kT}\right)^{3/2} \hbar^2 \sum_i (\omega\gamma)_i e^{-E_i/kT} \tag{1.11}$$

where $(\omega\gamma)_i$ and $E_i$ represent the individual resonance strengths and energies. To determine the size and position of the Gamow window in which resonances contribute to the total reaction rate one needs to consider the combined effects on the reaction rate of the MB velocity distribution and the probability of a charged particle to penetrate the Coulomb barrier of the target nucleus. Within the present reaction rate framework the effect of the Coulomb barrier is present in the definition of the partial width of the entrance channel. The partial width is defined theoretically in Eq. 1.12 [28],

$$\Gamma_l = \frac{3\hbar}{R}\left(\frac{2E}{m_{01}}\right)^{1/2} P_l\theta_l^2 \tag{1.12}$$

Here $\Gamma_l$ represents the partial decay width of a particle with angular momentum $l$, R represents the interaction radius of the particles in the entrance channel (0 and 1), $\theta_l^2$ gives the reduced partial width (which describes the degree to which the compound nucleus 0 + 1 can be described by the relative motions of the 0 and 1 particles), and $P_l$ is the penetration factor for the entrance particles to overcome the electrostatic

repulsion that exists between them.

$P_l$ can be found analytically by solving the Schrödinger equation for a Coulomb field and has the following form,

$$P_l = \frac{1}{F_l^2 + G_l^2}. \tag{1.13}$$

$F_l$ and $G_l$ represent the regular and irregular Coulomb wave functions and are given by modified Bessel functions [28]. To see the dependence on the Coulomb barrier more explicitly a first-order approximation can be taken for the $l = 0$ case, and the result is,

$$P_0 \propto e^{-2\pi\eta} \tag{1.14}$$

where $\eta$ is the probability of Coulomb transmission [29] and has the form,

$$\eta = \frac{Z_0 Z_1 m_{01} e^2}{2\hbar E}.$$

Here $Z_i$ represent the proton numbers of the interacting nuclei. When considering which resonances of the 0 + 1 compound nucleus have dominant contributions to the reaction rate we can examine the combined effects of the $e^{-E_r/kT}$ and $e^{-2\pi\eta}$ factors. The energy region that is found to maximize the product of these two factors is the Gamow window introduced previously. The resonances found within this window will comprise the dominant contributions to the total reaction rate. Figure 1.2 graphically displays this region.

The Gamow window displayed in Figure 1.2 represents the energy window for the $^{15}$O($\alpha$,$\gamma$)$^{19}$Ne reaction at T = 0.4 GK. In this case resonances between 350 and 800 keV are expected to dominate the reaction rate. Figure 1.3 displays the Gamow window for varying temperatures at which breakout from the HCNO cycles via the $^{15}$O $\alpha$-capture takes place.

The peak $E_0$ and the width $\Delta$ are calculated by taking a derivative of the $e^{-E/kT}e^{-2\pi\eta}$ product and by requiring that the second derivative from the left and the right are equal at $E_0$ [28]. The expressions for these quantities are given as,

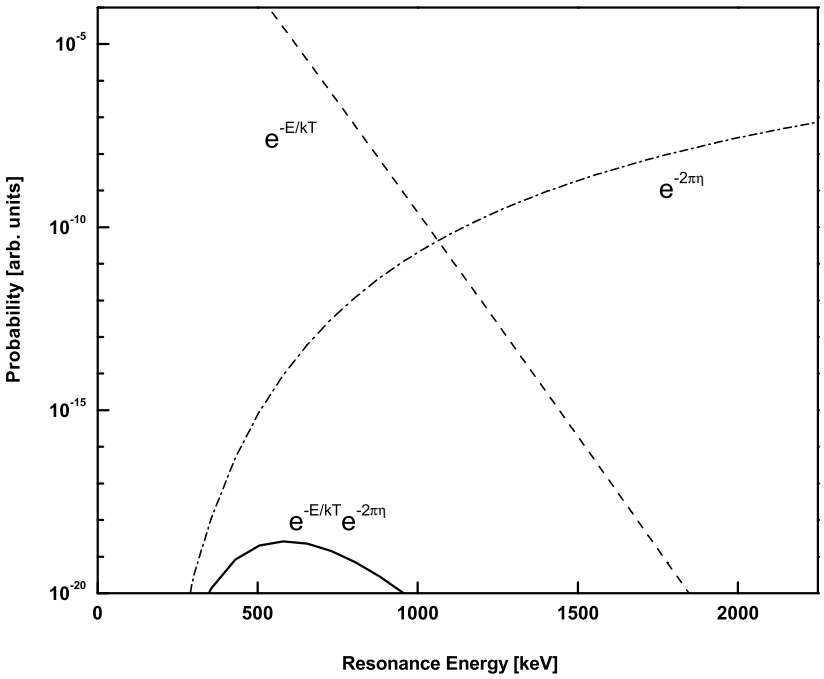


Figure 1.2: Maxwell-Boltzmann factor, Gamow factor and their product. The product denotes an energy region wherein resonances contribute most to the total reaction rate. This region is the Gamow window for the $^{15}$O($\alpha$,$\gamma$)$^{19}$Ne reaction at T = 0.4 GK.

$$E_0 = \left(\frac{bkT}{2}\right)^{2/3} \tag{1.15a}$$

$$\Delta = \frac{4}{\sqrt{3}}(E_0 kT)^{1/2} \tag{1.15b}$$

where,

$$b = 31.28 Z_0 Z_1 m_{01}^{1/2}.$$

Until the introduction of the Gamow window, this treatment of the resonant reaction rate formalism was generalized to some charged-particle induced two-body nuclear reaction. The reaction of significance to this project, however, is the $^{15}$O($\alpha$,$\gamma$)$^{19}$Ne reaction. For this reaction, the particles in the entrance channel that create an excited $^{19}$Ne nucleus are $^{15}$O and an $\alpha$ particle. The excited states of in-

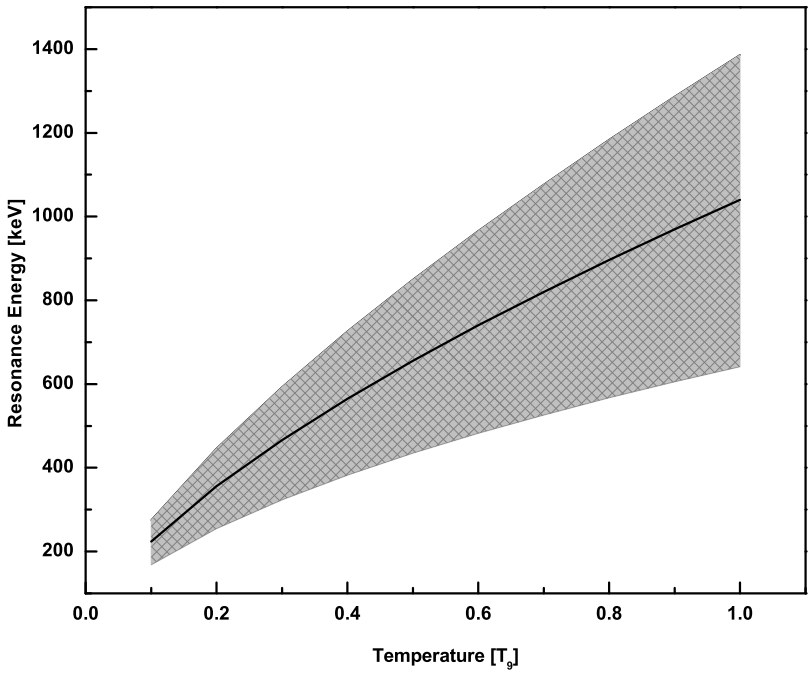


Figure 1.3: Temperature dependence of the Gamow window for the $^{15}$O($\alpha$,$\gamma$)$^{19}$Ne reaction within a range relevant to Type I x-ray bursts. The bold line denotes the Gamow peak within the window.

terest, i.e. the energy levels in $^{19}$Ne corresponding to rate-contributing resonances between $^{15}$O and $\alpha$ nuclei, can be calculated as $E_X = E_r + Q$, where Q is the $\alpha$-decay threshold and $E_r$ are the centre-of-mass frame resonance energies between $^{15}$O and the $\alpha$ particles.

For a stellar temperature of 0.4 GK, the Gamow window has a full energy-width of 344 keV centred at 560 keV. This window implies that at 0.4 GK the energy levels of $^{19}$Ne that contribute to the reaction rate are found between $E_X = 3.911$ MeV and 4.255 MeV. An energy level diagram of $^{19}$Ne is given in Figure 1.4 that displays the Gamow window and the rate contributing resonances at 0.4 GK. There are three levels, at 4.03-, 4.14-, and 4.20-MeV, that lie within the Gamow window and as such these excited states represent the excited states in $^{19}$Ne that will contribute to the $\alpha$ capture reaction rate. It can also be seen that the lowest excited state at 4.03-MeV lies closest to the Gamow peak indicating that the $^{15}$O($\alpha$,$\gamma$) reaction predominantly

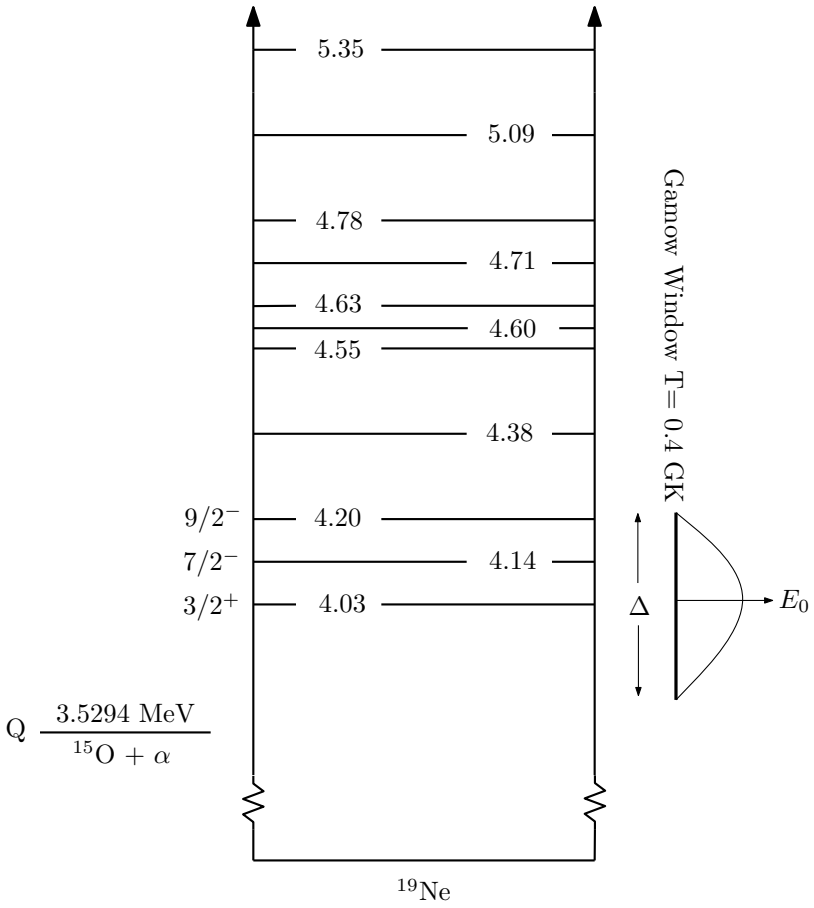


Figure 1.4: Energy levels of $^{19}$Ne above the $\alpha$-decay threshold, and Gamow window at T = 0.4 GK.

occurs via this excited state. The experimental measurement of the $\alpha$-partial width of this state is the subject of this project. It will be determined by firstly calculating the $\alpha$-branching ratio by measuring the $\alpha$-decay yield of the 4.03-MeV excited state and the cross section for populating the state. Secondly, as $\Gamma_\alpha = B_\alpha \Gamma$ and $\Gamma = \hbar/\tau$, measurements of the known lifetime for this state and $B_\alpha$ will be used to determine the $\alpha$ partial width. Before the proposed measurement technique is introduced, a review of the previous experimental attempts at measuring this quantity will be given in the following section.

## 1.3 Review of Measurements of $B_\alpha$(4.03-MeV)

A direct measurement of the $^{15}O(\alpha,\gamma)^{19}Ne$ reaction rate has not been made to date. Due to the fact that the cross section for this reaction has been estimated to be on the order of 100 pb and current intensities of radioactive $^{15}O$ beams are far too low [23], a direct measurement of this kind is not yet feasible. As a result, experimental efforts to measure pertinent information regarding the relevant resonance in $^{19}Ne$ (see Section 1.2) have focused on indirect measurements. These typically consist of bombarding a target to produce transfer reactions that populate excited states in $^{19}Ne$, and then observing the decay products. This approach provides information that allows calculations of the branching ratios of the $^{19}Ne$ excited states. Due to poor statistics, however, most previous indirect attempts have not been successful in observing the $\alpha$-decay of the 4.03-MeV excited state which has been shown to dominate the $^{15}O(\alpha,\gamma)$ rate. This has resulted in reports of experimental upper limits that constrain the $\alpha$-branching ratio for this state but the actual $B_\alpha$ value may be much lower.

The purpose of this thesis is to outline a novel measurement of the $\alpha$ partial width of the 4.03-MeV excited state in $^{19}Ne$ and in this section the results and downfalls of the previous measurements will be discussed so that the inherent difficulties of this measurement can be made clear. Starting at the beginning, the earliest experimental attempt to describe the partial decay width in the 4.03-MeV excited states in $^{19}Ne$ relied on analogous measurements made on the mirror nucleus of $^{19}Ne$, $^{19}F$ [30]. It has been shown, though, that using partial widths from analog states in mirror nuclei can produce large uncertainties in the reported widths [31].

The results of six measurements of decay widths in excited states of $^{19}Ne$ have been included in this discussion, and are given in Table 1.1. While all of these attempts began by populating excited states of $^{19}Ne$, the reactions, detection methods, and sensitivities to the low lying $\alpha$-unbound states vary. Half of the previous attempts made use of normal kinematics reactions to populate states in $^{19}Ne$, i.e., Magnus et al.,[21] Visser et al.,[25] and Tan et al.,[32] bombarded heavy target nuclei with light projectile species. All of these groups used a $^3He$ beam and a $CaF_2$ target to produce a $^{19}F(^3He,t)$ reaction. The work of the others involved inverse kinematics

reactions to populate excited states in $^{19}$Ne, i.e., heavy ion beams bombarding light targets. Laird et al.,[22] Rehm et al.,[23] and Davids et al.,[24] populated excited states in $^{19}$Ne via d($^{18}$Ne,p), $^{3}$He($^{20}$Ne,$\alpha$), and p($^{21}$Ne,t) reactions, respectively.

All attempts discussed here were successful in populating the relevant excited states in $^{19}$Ne. All of the results, however, report low or null statistics for observing the $\alpha$-decay of the excited states that lie just above the $\alpha$-decay threshold in $^{19}$Ne. In fact, only one group (Tan et al.,[32]) reported observations of $\alpha$-decay from the rate dominating 4.03-MeV state that were in excess of the background (although, their reported measurement has been disputed [15]). The inherent difficulty in observing the $\alpha$-decay from the state at the 4.03 MeV excitation energy has been caused by several factors. The primary reason is due to that fact that the $\alpha$-branching ratio $B_\alpha$ is expected to be $\sim 10^{-4}$. This value is so small that when coupled with typical beam intensities, experiment durations, and small reaction cross sections the likelihood of observing an event, in excess of the background, is nearly zero for the approaches used before.

These indirect methods rely on coincidence measurements to uniquely identify the decay products from the different excited states that have been populated. All of the groups except Rehm et al.,[23] and Davids et al.,[24] measured coincident detector hits of reaction ejectiles (tritons or protons) and the $\alpha$ particles from the $^{19}$Ne decay. This approach becomes extremely difficult for the case of the important states that are just above the $\alpha$-decay threshold as these states generate the lowest-energy $\alpha$ particles possible. These decay products can be emitted with such low energy that they are stopped in the inactive front layer of the detectors and are never observed. It was typical, however, that accurate branching ratios measurements were reported for the higher lying states, i.e., $E_r > 4.5$ MeV for groups that experienced the low-energy $\alpha$ detection problem. This issue was directly addressed in the work of Tan et al., by using a unique silicon array detector that had a significantly thinner inactive layer so as to not stop incident $\alpha$ particles which contributed to their $B_\alpha$ measurement of the 4.03-MeV excited state. This was also a non-issue for Rehm et al., and Davids et al., as they did not attempt to detect the low-energy $\alpha$ particles, but rather the heavy decay products ($^{15}$O and $^{19}$Ne$_{g.s.}$) with a spectrograph.

| Group | $B_\alpha$ - 4.03-MeV | Remarks |
|---|---|---|
| Magnus[21] | $\approx 10^{-4}$ | Data from mirror nucleus $^{19}$F. |
| Laird[22] | $< 0.01$ | Low beam intensities. High background. |
| Rehm[23] | $< 6{\cdot}10^{-4}$ | Insufficient beam time to acquire detections. |
| Davids[24] | $< 4.3{\cdot}10^{-4}$ | Too few coincidences cf. fragmentation background. |
| Visser[25] | N/A | Low energy $\alpha$-particles stopped in dead layer. |
| Tan[32] | $2.9{\pm}2.1{\cdot}10^{-4}$ | Sensitive TOF detector to identify low energy $\alpha$'s. |

Table 1.1: Summary of measured $\alpha$-branching ratios for 4.03-MeV excited state in $^{19}$Ne.

Another issue which was common to all measurements is that due to the inherently low probability of $\alpha$-decay detections, the background level in the coincidence spectra could not be made low enough to accommodate such a sensitive measurement. The sources for background radiation vary greatly depending on the specific target, beam species, beam energy, and detector type that were used during the experiments mentioned previously, so a detailed discussion will not be given here. It can be remarked, however, that the greatest source of background was due to the low-energy tail of $\alpha$ particles from the decay of excited states above the 4.03-MeV energy level. Any novel attempt at measuring the $\alpha$-branching ratio of the 4.03-MeV excited state in $^{19}$Ne should, therefore, be designed to minimize background activity during the experiment. As the precision to which this measurement can be made via the typical indirect approach seems to be at a standstill, further reduction in uncertainty may require a new approach. To this end, a novel experiment has been designed to measure, with greater precision than that of Tan et al., the $\alpha$-branching ratio of the 4.03-MeV state of $^{19}$Ne that may be used to constrain the $^{15}$O($\alpha$,$\gamma$)$^{19}$Ne reaction rate. This experimental approach is outlined in the next section and presented in detail in Chapters 2 and 3.

## 1.4 $\beta^+$ Activity Measurement

With the understanding of the difficulties involved in previous attempts at measuring the elusive $\alpha$-branching ratio of the 4.03-MeV excited state of $^{19}$Ne, a novel approach has been devised that has the capacity to circumvent the typical challenges in this measurement. By avoiding geometric efficiencies issues, coincidence detection

limitations, and high background from beam-related reactions and $\alpha$-decay from higher energy levels, the measurement challenges discussed in Section 1.3 can be surmounted.

In this approach, hereafter referred to as the $\beta^+$ activity technique, $\alpha$-decay from the 4.03-MeV state in $^{19}$Ne will be detected via the $\beta^+$ activity of the $^{15}$O recoil nucleus. To do this, the 4.03-MeV excited state will be populated at threshold, such that no other $\alpha$-unbound states are populated, with the p($^{19}$F,n) reaction, using a $^{19}$F beam and a hydrogen gas cell target. The decay products of $^{19}$Ne will be filtered such that the $\alpha$-decay products ($^{15}$O) will be selected and allowed to proceed from the target region. After the $^{15}$O nuclei exit the hydrogen gas cell target they will impinge upon a tantalum foil designed to stop them. Within the tantalum catcher foil the $^{15}$O nuclei will $\beta^+$ decay and emit positrons, isotropically, that are expected to annihilate within the tantalum and emit back-to-back 0.511 MeV $\gamma$-rays. The catcher foil will be mounted on a rotating disk that will relocate the foil to a region in between two face-to-face NaI(Tl) detectors that will measure the 0.511 MeV signature of the $^{15}$O nuclei. This measurement is technically similar to that of Tang et al., (2010) [33] and will take place at Argonne National Laboratory.

By this mechanism the $^{15}$O yield from the 4.03-MeV state, exclusively, will be determined. A cross section measurement for populating the 4.03-MeV excited state in $^{19}$Ne will be performed in a separate experiment which will generate the data needed to calculate the $\alpha$-branching ratio for the 4.03-MeV excited state. Along with recent lifetime measurements [34, 35, 36], the $\alpha$ partial width can also be determined and used to evaluate the $^{15}$O($\alpha$,$\gamma$)$^{19}$Ne reaction rate. The lifetime measuremnets were calculated using measured partial $\gamma$-decay widths and theoretical partial $\alpha$-decay widths for the 4.03-MeV state. The measurements by references 34, 35, and 36 employed a doppler shift attenuation analysis of $^{19}$Ne $\gamma$ decays to produce their results.

Since an inverse kinematics reaction is used to populate the 4.03-MeV excited state in $^{19}$Ne, the reaction products and subsequent decay products emerge forward focused in the laboratory frame. A beam of $^{19}$F will impinge on an $H_2$ gas cell with a HAVAR entrance window foil and a gold exit window foil. The $^{15}$O nuclei will be selected from the forward focused decay products by the gold exit window foil as

its thickness will be such that the $^{19}Ne_{g.s.}$ nuclei from $\gamma$-decay will be stopped and only $^{15}O$ nuclei will be able to pass through. Ranges in gold for each of these ions have been determined from energy-loss simulations and the results are discussed in Chapter 3. Given the fact that a small, known amount of $^{15}O$ will be stopped in the gold, an inverse kinematic reaction guarantees that the $^{15}O$ nuclei can be stopped in an isolated location which increases the detection efficiency of the following $\beta^+$ activity

As this technique has not been used previously to measure the $\alpha$-branching ratio of the 4.03-MeV state in $^{19}Ne$, beam time has been requested for the purposes of a test run to experimentally verify this approach. The test run will consist of populating higher excited states in $^{19}Ne$, specifically the 5.35-MeV state, as it has $B_\alpha$ values $\sim 1$ and will produce observable events in a significantly shorter time period. The purpose of this test will simply be to check that a 0.511 MeV $\gamma$-ray signature will be observed from the $\alpha$-decay products' $\beta^+$ activity. Should this prove successful, more beam time will be requested later on to proceed with the $B_\alpha$ measurement of the 4.03-MeV excited state and a measurement of the cross section for populating the 4.03-MeV state in $^{19}Ne$. The entire reaction and detection processes have been simulated to determine several experimental parameters. These consist of the thicknesses of the gold and tantalum foils, $^{15}O$ transmission through the gold foil, as well as the total and geometric detection efficiencies. This work is presented in Chapter 3 and demonstrates that this approach is feasible.

Chapter 2

# Experiment Design

In designing a nuclear astrophysics experiment a great deal of care must be taken in deciding the best approach to achieve what is desired. For the purposes of this project an experimental design is needed that leads to populating the 4.03-MeV and 5.35-MeV excited states in $^{19}$Ne and provides a means of detecting the $\alpha$-decay products all within a feasible amount of time. The design must also ensure that the $\alpha$-decay from other excited states is minimized. Within these requirements there is a great deal of freedom over the choice of beam, reaction, target, and detector arrangement.

In general one would want to choose a beam that can be generated with a stable current and energy. As well the reaction choice should be one with a relatively high cross section to increase the yield of important products, a task which is often difficult in the field of nuclear astrophysics due to inherently small reaction cross sections. A target should be chosen that is suitable for the desired current and that is low in contaminants so that the background in the spectra is minimized. The choice of detection method is also very important as a detector should be chosen that best suits the resolution, particle type, energy range, and cost requirements. Reliable electronics and signal digitizing devices are also very important, but these are typically owned and maintained by the ion beam facilities at which experiments of this nature are performed, and are not discussed here.

In this chapter the experimental details and design process of the $\beta^+$ activity measurement will be discussed. The following sections describe the ATLAS facility,

beam details, target description and detection methods.

## 2.1 The Beam at ATLAS

The Argonne Tandem Linear Accelerator System, or ATLAS, is aptly described in its name. To repeat the obvious, ATLAS is a tandem linear accelerator and the world's first superconducting linear accelerator (linac); it is located at the Argonne National Laboratory in Lemont, Illinois. ATLAS is capable of producing beam species in the range of hydrogen to uranium at energies of 7 to 17 MeV/nucleon. Light radioactive beams can also be produced via the in-flight technique at various target stations in the facility. Details of ATLAS and the beam required for our experiment are given in the following.

### 2.1.1 ATLAS

Originally built in 1978 with upgrades in 1985 and 1986, there are two sources in use at ATLAS that are referred to as "injector accelerators". They are the 9 MV Tandem Van de Graff and 12 MV Positive Ion Injector, the latter being comprised of a low velocity linac and an electron cyclotron ion source. The next segment of ATLAS is the "booster" accelerator which is a 20 MV linear accelerator. The last segment is the "ATLAS" accelerator which is also a 20 MV linac.

The entire apparatus makes use of sixty-four superconducting resonators, of which there are two kinds. While the Positive Ion Injector makes use of four varieties of quarter wave resonators, the booster and ATLAS linacs use two kinds of split-ring resonators. These resonators are housed in liquid helium cryostat units that maintain superconducting conditions. A floor plan of the ATLAS facility is given in Figure 2.1.

### 2.1.2 $^{19}$F Beam

A beam of stable $^{19}$F ions was chosen to initiate $^{1}$H($^{19}$F,$^{19}$Ne)n reactions to populate the excited states of interest in $^{19}$Ne. At ATLAS a $^{19}$F beam can be produced with a maximum energy of 334 MeV at a peak current of 10 pnA and

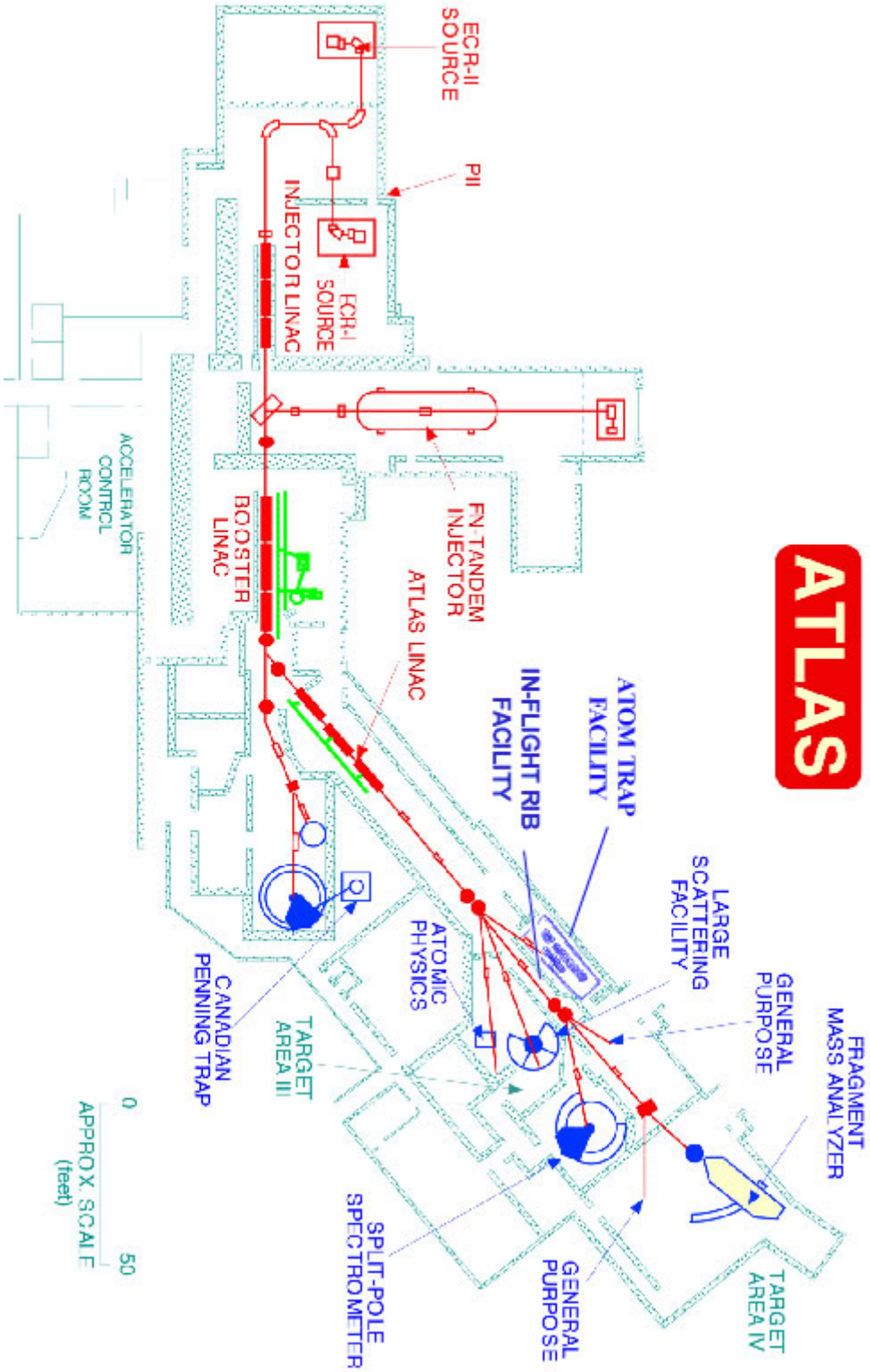


Figure 2.1: The ATLAS Facility (retrieved from the ATLAS webpage).

minimum energy of 114 MeV at 50 pnA. This information then begs the question, is this range of beam energies suitable for the desired reaction? In short, yes, but the experimental designer must ensure that this is the case by evaluating the reaction Q-value and comparing this to the centre-of-mass frame energy of the projectile-target system.

By definition the Q-value indicates whether any given nuclear reaction releases or consumes energy to proceed. The Q-value expresses the difference in mass-energy of the reactants and products in the centre-of-mass frame. A negative Q-value indicates that the reaction must be supplied energy to proceed and requires some initial contribution to the kinetic energy of the system, while a positive Q-value indicates that a reaction can happen spontaneously given entrance channel particles that come close enough to each other to interact. As the Q-value is computed as,

$$Q = (m_p + m_t - m_r - m_e)\, c^2, \tag{2.1}$$

we require values for the nuclear masses of the $\mathrm{m}_p(^{19}\mathrm{F})$, $\mathrm{m}_t(^{1}\mathrm{H})$, $\mathrm{m}_r(^{19}\mathrm{Ne})$ and $\mathrm{m}_e(n)$ nuclei. The National Nuclear Data Center website gives these masses as 18.99840 u, 1.00782 u, 19.00188 u, and 1.00866 u, respectively. As one atomic mass unit (u) is equivalent to 931.502 MeV/$\mathrm{c}^2$, we attain a value for Q of -4.023 MeV. These masses assume that the nuclei are in their ground state so it follows then that to calculate the Q-value for the reaction that populates excited states in $^{19}$Ne one needs to also incorporate the energy required to excite the $^{19}$Ne nucleus to the desired energy level. For the purposes of this experiment we calculate the reaction Q-values to be -8.058 MeV and -9.374 MeV for the two experimental phases that populate the 4.03-MeV and 5.35-MeV excited states in $^{19}$Ne, respectively.

The minimum laboratory-frame kinetic energy of the projectile can be calculated as

$$E_p = Q \cdot \frac{m_t + m_p}{m_t} \tag{2.2}$$

where Q represents the magnitude of the Q-value. Given the masses for $m_p$ and $m_t$, and the two relevant Q-values one can see that the necessary $^{19}$F beam energies are 160 MeV and 186 MeV. In reality one could use beam energies that are higher than

these but also less than the energy required to populate excited states that are just above the 4.03-MeV and 5.35-MeV levels, which are the 4.144-MeV and 5.424-MeV levels. These upper limits correspond to $^{19}$F beam energies at 162 MeV and 187 MeV, respectively.

As the maximum $^{19}$F beam energy is 334 MeV at ATLAS, the necessary beam energies for the experiment and its test run can be achieved. These beam energy requirements do not, however, take into account the fact that the target will be gaseous hydrogen and must be contained within a gas cell at constant pressure. The entrance window of the gas cell will result in an energy loss of the beam particles that needs to be calculated so that the necessary $^{19}$F beam energy can be determined. The effects on beam energy due to the hydrogen target and the gas cell will be described in the following section.

## 2.2 Gas Cell Reaction Targets

Choosing a target for an experiment can be a very involved process. Depending on whether the experiment requires a neutron-induced or charged particle reaction, there are various target options that may be suitable. For the purposes of this project the reaction involves charged particles in the entrance channel as well as an inverse kinematic approach, i.e., the projectile is heavier than the target nucleus. Considering these constraints a hydrogen gas cell target was chosen to perform this experiment.

### 2.2.1 Benefits and Shortcomings of Gas Cell Targets

As with any target option, gas cells are not without imperfection. However, there are various aspects of gas cell targets that make them the ideal candidate for the $^{1}$H($^{19}$F,$^{19}$Ne)n reaction. The eventual measurement of the $\alpha$-branching ratio of the 4.03-MeV state is a very challenging one and due to the small reaction cross section and the fact that the current estimate of $B_\alpha$ is on the order of $10^{-4}$, observation of the relevant $^{19}$Ne decay products will take place much less frequently than many alternate reaction channels. To minimize background radiation during this experiment it is favourable to have a target with a high purity.

A pure gas target can be prepared much more easily than a solid implanted target. Implanted targets are made by trapping target nuclei within a backing material. Carbon, tantalum, and nickel are common backing choices [9]. The stoichiometric values for these kinds of targets often indicate higher densities in the backing material than the target species. This deficiency in target material can result in low reaction yields. Also, solid targets often experience a build up of contaminants on its surfaces. This is often a result of exposure to air and moisture either during the experiment or in extended storage periods. Solid targets are also at risk of degradation from exposure to high beam currents. The heat caused by the power dissipated by the beam may destroy the target material if not cooled properly. These problems are non-issues for gas targets.

In the case of inverse kinematic experiments, it may not even be possible to create light ion solid targets with a reasonable purity [9]. Gas targets, however, can easily be prepared with a very high purity, thus reducing the possibility of contaminants and background radiation. Using gas as a target material is also favourable for higher beam intensities as the gas is indestructible compared to solid targets [1].

As indicated in the section title, however, there are many design concerns with the use of gas targets. Gas targets are typically enclosed in a cell with foil windows that are designed to allow the beam and reaction products to enter and exit. These are the most critical points in a gas cell [1]. The entrance foil for the beam has several concerning effects that consist of a reduction in beam energy, a broadening of the beam size, and increased background radiation from interactions between the beam and foil [9]. The foil materials must be chosen carefully so that the windows interact very weakly in the energy range of interest. If this is not possible, particularly in the case of high beam energies, materials should be chosen that cause radiation background that is highly separated, in energy, from the desired reaction products.

There are solutions to many of these problems with more complicated gas target designs. Gas jets may be used along with high velocity pumps to create a localized beam of gas particles, perpendicular to the beam, that does not destroy the vacuum of the system [1]. These alternative gas target designs are much more difficult to operate and expensive. For the purpose of this experiment, a tested 16

cm long hydrogen gas cell will be used [33]. The constraints on the gas target's mass thickness and foil window materials will be discussed in the following section.

### 2.2.2 Target and Window Constraints

The mass thickness of the target is easily controlled by adjusting the gas pressure in the cell. This can be done with very good precision, reducing target thickness uncertainty. The mass thickness of the target should be made no greater than that which disallows the population of the desired excited state. In other words, for a resonant charged particle reaction, the energy loss of the beam in the gas should be smaller than the separation between the excited state of interest and the next [9].

For the experiment and test run cases where the 4.03-MeV and 5.35-MeV excited states in $^{19}$Ne are populated, the ideal target mass thicknesses have been determined. The separations of the excited states of interest with their adjacent levels have been determined [22]. It was found that, in the centre-of-mass frame, the 4.03-MeV state is separated by 0.109 MeV from the next level above and the 5.35-MeV state is 0.073 MeV below the higher adjacent state. Substituting these values into Equation 2.2 for Q gives the energy level differences in the laboratory frame. Energy windows of 2.13 and 1.45 MeV were found for the 4.03-MeV and 5.35-MeV cases, respectively. On a side note, one need not consider lower excited states as no state exists between the 4.03-MeV state and the $\alpha$-decay threshold. Similarly for the test run, we are not concerned with populating lower excited states as our aim is to show whether the $\beta^+$ activity technique functions reliably, or not.

Thus, in choosing a mass thickness for the hydrogen gas target we must ensure that the beam's energy loss during transmission does not exceed these values, i.e. 2.13 MeV and 1.45 MeV. It was found using the LISE++ physical calculator tool that the maximum mass thicknesses of hydrogen gas for beam energies of 162 MeV and 187 MeV are 0.23 mg/cm$^2$ and 0.18 mg/cm$^2$. These thicknesses ensure that populating the energy levels of interest in $^{19}$Ne is energetically possible within the gas cell. For this project the mass thickness of 0.23 mg/cm$^2$ has been adopted for both the experiment and test run considerations.

The experimental control over the mass thickness of a gas target is in adjusting the pressure of the gas within the cell. Gas pressure can be related to mass thickness

by the Ideal Gas Law, which can be written in the form,

$$P = \frac{N}{V} \cdot kT. \tag{2.3}$$

Where P is the pressure of hydrogen gas within the cell, T is the gas temperature and $k$ is the Boltzmann constant. The $N/V$ factor describes the number of gas particles per cubic meter, i.e. the particle density. The mass density of the gas can quickly be determined as the mass thickness divided by the length of the gas cell, 16 cm. The number density of hydrogen can then be found as the mass density divided by the mass per hydrogen molecule. As the hydrogen molecule is diatomic its mass will be given as 2.01564 u, twice the proton mass given in the previous section. The Ideal Gas Law becomes,

$$P = \frac{\rho}{m(H_2)} \cdot kT. \tag{2.4}$$

Assuming an ambient temperature of 290 K one arrives at a gas cell pressure of $128.98 \approx 130$ Torr. To correct for unit discrepancies the following conversion factors were used: 1 u = $1.6605 \cdot 10^{-21}$ mg, 1 $cm^3$ = $10^{-6}$ $m^3$, and 1 Pa = $7.5006 \cdot 10^{-3}$ Torr. Thus we need to maintain a hydrogen gas pressure of 130 Torr to have a mass thickness of 0.23 mg/$cm^2$.

The ability to maintain constant pressure within the cell will largely depend on the state of the window foils that will be used. As the incident beam will deposit some energy into the entrance window of the foil, the dissipated power has the capacity to damage or destroy the windows. Not only would this affect the gas pressure in the cell, but it would also destroy the vacuum that must be maintained outside of the cell. In order to not destroy the windows during an experiment the beam current must be set to a reasonable intensity. Roughly speaking, the limit on this current is related to the inverse of the reaction cross section involved in stopping the beam ions [1]. The condition of the gas cell windows will be monitored closely during both experiments.

The energy loss of the beam through the entrance window must also be identified so that the beam energy can be set such that upon entering the gas cell the $^{19}F$ nuclei have the energy values discussed in Section 2.1.2. Experimentally this can be

done by using a calibrated $\alpha$ source with a sufficiently narrow decay energy, and observing the energy shift that results from the entrance window obstructing the path. This method can also be used to quantify the effects of straggling within the foil [1]. If $\alpha$ particles were stopped in the foil an alternative method would be to examine the attenuation of $\gamma$-rays passing through the foil. Energy loss calculators, like the LISE++ physical calculator, can be used beforehand to give an accurate estimate of this energy loss. Using this program the initial beam energy can be varied while holding the thickness constant until the resultant energy is equal to that which is required, 162 MeV or 187 MeV.

Given the considerations made above, the proposed material for the entrance window is 1.9 mg/cm$^2$ thick HAVAR foil. HAVAR foil is a high strength non-magnetic alloy patented by Goodfellow Ltd.; it is a typical energy degradation material used in many nuclear physics experiments [37]. Use of the LISE++ physical calculator resulted in a pre-gas-cell energies of 166.5 MeV and 191.5 MeV for the experiment and test run, respectively.

The exit window of the gas cell, through which reaction products pass, is another topic of crucial consideration. The mass thickness for this window is more complicated to determine as it is designed to stop the $^{19}$Ne $\gamma$-decay products and transmit the $\alpha$-decay products. A detailed treatment of this is given in Chapter 3 as the foil thicknesses are determined via Monte Carlo simulations. For now it will suffice to say that the exit window is a gold foil with a thickness around 60 - 70 mg/cm$^2$. The foil was chosen to be composed of gold as this heavy nucleus would reduce background due to charged particle-induced reactions due to its high Coulomb potential barrier. A characterization of the sources of background radiation will be given in Section 2.4. Before that, however, a description of the detection system will be given in the following section.

## 2.3 Detection Technique

Following the $^1$H($^{19}$F,$^{19}$Ne)n reaction that takes place within the gas cell, the excited $^{19}$Ne nuclei will decay. At the energy levels of interest in this project there are only two energetically possible options, $\gamma$ or $\alpha$ decay. In determining the $\alpha$-branching

ratio the focus is set on observing the $\alpha$-decay yield. A detection mechanism must be put into place that can accurately detect the low yield that is anticipated from the decay of the 4.03-MeV state in $^{19}$Ne. This experiment will employ the $\beta^+$ activity method as a means of measuring the $\alpha$-decay yield.

### 2.3.1 Catcher Foil

The $\beta^+$ activity of the $^{15}$O daughter nucleus from the $\alpha$-decay of $^{19}$Ne will be observed. Since the $\gamma$-decay product, $^{19}\text{Ne}_{g.s.}$, is also $\beta^+$ unstable, a gold exit window of the gas cell is needed that will stop all $\gamma$-decay products and transmit only $^{15}$O nuclei. The kinematic solutions of this reaction process demand that these nuclei emerge forward focused in the laboratory frame from the exit window. The transmitted $^{15}$O nuclei will travel towards a tantalum catcher foil that is sufficiently thick to stop any transmitted nuclei, i.e., $^{15}$O and $^{19}$F ions. The choice of tantalum for the catcher material was made as it is a high Z metal and will strongly interact with the $\beta^+$ particles from the decay of $^{15}$O. Tantalum, along with other high Z materials, is ideal for minimizing background from reactions between ions and the catcher foil due to a high Coulomb barrier.

$\beta$ particles are not emitted with a characteristic energy [38] but rather, in a continuous spectrum of energies. As such, it would be difficult to say with certainty that a detection of one implies the existence of an $^{15}$O nucleus. The annihilation of a $\beta^+$ particle and an atomic electron in the catcher foil, however, produces two back-to-back 511-keV photons. This energy indicator is very distinct and provides a more certain way of counting the $^{15}$O yield. Choosing a catcher foil material with a high Z value provides a higher density of atomic electrons for which a $\beta^+$ particle can interact and annihilate [39]. The ideal thickness of the catcher will be determined by simulated detector responses (Section 3.2.5) but it can be said at this point that the minimum thicknesses to stop the remaining beam particles must be 16 $\mu m$ and 27 $\mu m$ for the experiment and test run phases, respectively.

The catcher foil will be mounted onto a rotating disk whose symmetry axis is parallel to the beam axis, such that once it has been irradiated with $^{15}$O nuclei for the desired time it will be rotated to a space between two face-to-face NaI(Tl) detectors. By placing two foils at opposite positions on the disk, it can be assured

that the $^{15}$O collection is, effectively, a continuous process. This setup has been adapted from that of the $^{12}$C($\alpha$,$\gamma$)$^{16}$O cross section measurement of Tang et al. in 2010 [33]. Some design modifications to the rotating disk and vacuum chamber have been made to accommodate the use of two foils (rather than three) and our detector arrangement. A diagram of the setup is shown in Figure 2.2.

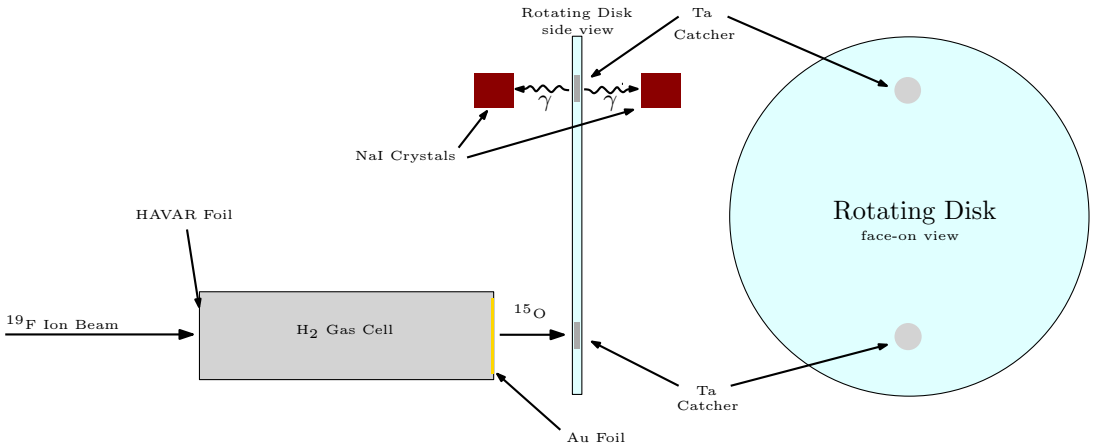


Figure 2.2: Schematic diagram of the experimental setup used to measure the $\alpha$-branching ratio of the 4.03-MeV excited state of $^{19}$Ne.

As the half life of the $\beta^+$-unstable $^{15}$O nucleus is known to be 122 s [40], some care needs to be taken in deciding the frequency of the rotating disk. In Chapter 5, the ideal exposure time will be calculated that takes into account the $^{15}$O half life and production rate.

### 2.3.2 Detector Arrangement

It was briefly mentioned in the previous section, without explanation, that the 511 keV $\gamma$-rays will be counted using two NaI(Tl) detectors. These detectors use scintillator crystals that transform the energy deposited by ionizing radiation into light [41]. The emitted light is converted into an electrical signal in a photomultiplier tube (PMT), and processed by various digital devices such that an output can be recorded for data processing.

The choice of detector type and size very much depends on the requirements of an experiment. Many factors like radiation species, energy/time resolution, and cost need to be considered before selecting an ideal detector. For the experiments

described in this project it is known that only the photons at 511 keV are of interest. The rate at which photon detections will be observed has been estimated to be 10 and $10^5$ photons/s for the 4.03-MeV and 5.35-MeV cases, respectively. These activity (A) estimates are based on the yield calculation,

$$A = I\sigma\rho\Delta t, \tag{2.5}$$

where the beam current I is measure in particles per second, $\sigma$ represents the cross section of the
$^1$H($^{19}$F,$n$)$^{19}$Ne*($\alpha$)$^{15}$O reaction, $\rho$ is the mass density of the target and $t$ represents its thickness ($\rho\Delta t$ is often referred to as the mass thickness). The half life of $^{15}$O, the loss of $^{15}$O ions in the exit window, and the catcher foil rotation frequency are accounted for to produce the previous activity estimates. The full calculation and results are given in the Chapter 5. The ideal detector must be sensitive to this energy of photons and have the resolution to distinguish them from background radiation sources. Since the reaction and detection apparatus will be placed within a small vacuum chamber there are also size constraints on the detectors that needed to be considered. The choice was made to use two sodium iodide detectors to satisfy the design constraints.

Sodium iodide crystals that are doped with thallium iodide, NaI(Tl), were first used in 1948 and produced a markedly intense light output compared to other scintillators [39]. Inorganic crystals, like NaI(Tl), rely on the semiconductor band gap configurations of electrons in crystal lattices to produce light. When ionizing radiation passes through the crystal lattice, valence electrons absorb energy and are excited into the conduction band. This is equivalent to an atomic electron escaping its atomic binding energy. These electrons will interact with a positively charged hole in the valence band and de-excite, emitting a photon in the process.

Pure crystals emit photons at energies that can not be seen, i.e., at wavelengths beyond the visible spectrum. By introducing activating impurities, like thallium, the energy levels between the valence and conduction bands are generated. These intermediate levels produce smaller gaps and nearer holes for electrons to de-excite to, resulting in fast acting steps down into the valence band. The smaller energy steps for electrons result in the emission of lower energy photons that give

rise to visible light [39].

When used in conjunction with a photomultiplier tube (PMT), the light emitted from the scintillator is converted into an electrical signal. This conversion process begins as incident photons interact with the photocathode of the PMT. The photons can excite valence electrons within the semiconductor photocathode that escape the material if they have enough energy to overcome the material's work function. Electrons that escape are typically low in energy and too few in number to create a feasible electrical signal. To remedy this, electrodes (known as "dynodes") are situated within the PMT that rely on secondary electron emission to increase the number of electrons contributing to the eventual output. The initial light pulse may produce $10^2$ free electrons; with the amplification of the dynodes, $10^{6-7}$ electrons will contribute to the output signal. Electrons incident on the dynodes collide with and free many bound valence electrons. The cumulative charge is collected at the PMT's anode and produces the electrical signal [39]. The outgoing current from these devices is proportional to the number of photons emitted by the ionizing particle's interaction with the crystal. As the number of photons emitted by the scintillator is proportional to the energy deposited by the ionizing particle, the ionizing particles' energy and time of interaction can be determined [42].

NaI(Tl) crystals are hygroscopic and absorb moisture from the surroundings. As such, they must be sealed in an environment that is free from moisture to prevent them from being damaged. Typical crystals are made to be cylindrical so that they are the same shape as a PMT. Particles generally enter these crystals through the flat face of the cylinder. Due to the spatial constraints in this project, these typical features are not desirable. The NaI(Tl) crystals to be used in our experiments have been constructed as cubes, with 2.54 cm side lengths. The cubic NaI(Tl) crystals have been mounted onto a cylindrical PMT, such that the diameter of the PMT is equal to the diagonal of the crystal (3.59 cm). The two detectors will be arranged such that the catcher foil will emit photons towards the side faces of the crystals. The two detectors will be oriented with a relative angle of $\approx 90^\circ$ between them. This arrangement places one crystal upstream and the other downstream from the catcher foil such that the two crystals mirror one another about the catcher foil. A schematic of this setup is given in Figure 2.3.

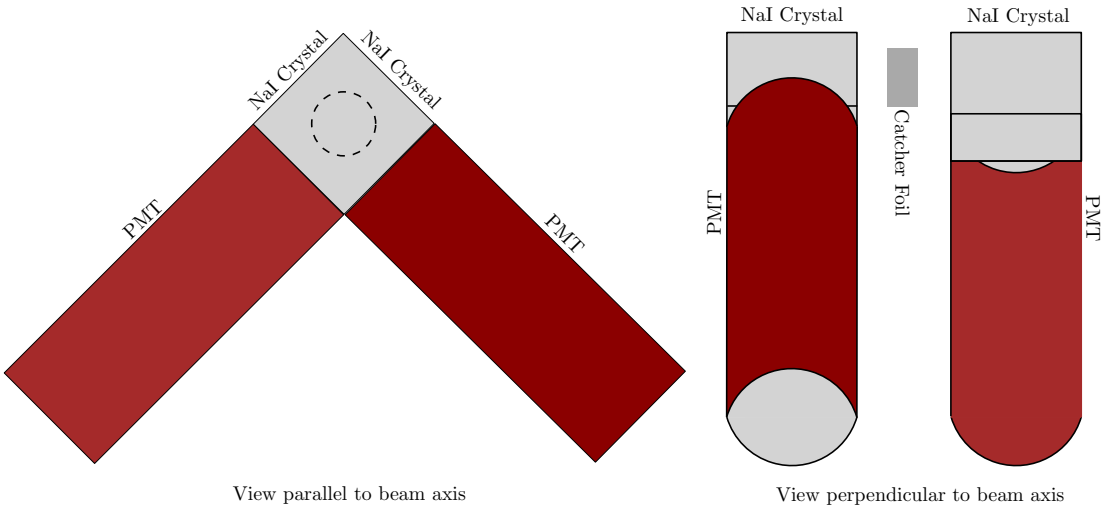


Figure 2.3: Schematic view of the detector arrangement.

In Figure 2.3, the catcher foil's thickness is drastically exaggerated for schematic purposes. The overall length of each detector is, roughly, 16 cm, the radius of the catcher foil will be 1 cm and the separation between the catcher foil and a shielded crystal has been estimated to be 0.8 cm. As the detectors have not, to date, been set within the vacuum chamber the separation length is only estimated based on the engineering sketch of the setup. This length is limited by the PMT diameter and the thickness of the rotating disk on which the catcher foil is mounted, as this disk must spin freely between the two face-to-face detectors.

This detection setup has been designed to observe the $\gamma$-ray signature of the $^{15}$O nuclei $\beta^+$ activity; however, no experiment setup is free of background radiation. In the following section some of the expected contributions to the background radiation will be discussed.

## 2.4 Background Radiation

There are many stages and interactions involved in this experimental setup. The beam's interaction with the various components of gas cell, standing radiation background from the facility and surroundings, and $\beta^+$ particles from the decay of $^{19}$Ne may all contribute radiation that is observed by the two face-to-face NaI(Tl) detectors. In the following some of the major sources and reduction techniques will be discussed.

The HAVAR entrance window, the gold exit window, and the tantalum catcher foil contain 21 possible isotopes with which the beam could interact. A ($^{19}$F,$^{15}$O) reaction could take place with any of these isotopes thus contributing to the yield of $^{15}$O nuclei. In Table 2.1, the products of the reactions with the most naturally abundant isotopes [43] are displayed along with a description of their stability and the reaction Q-value.

| Target Nuclei | Product | Stability | Q [MeV] |
|---|---|---|---|
| $^{52}$Cr | $^{56}$Mn | $\beta^-$ | -2.850 |
| $^{56}$Fe | $^{60}$Co | $\beta^-$ | -3.299 |
| $^{58}$Ni | $^{62}$Cu | $\beta^+$ | -1.773 |
| $^{59}$Co | $^{62}$Ni | $\beta^-$ | -1.059 |
| $^{184}$W | $^{188}$Re | $\beta^-$ | -11.034 |
| $^{181}$Ta | $^{185}$W | $\beta^-$ | -9.395 |
| $^{197}$Au | $^{201}$Hg | *Stable* | -7.821 |

Table 2.1: Foil-Beam Reactions Contributing to $^{15}$O Yield.

The decay modes were given in LISE++ and Q-values were determined using the CATKIN software. Given the beam energies at the appropriate locations in the setup, it was found that all of these reaction are energetically possible. Of these seven reactions only the $^{58}$Ni($^{19}$F,$^{15}$O)$^{62}$Cu reaction produces an extra $\beta^+$ emitter. It is expected that these reactions should have relatively low yields due to high Coulomb barriers and unfavourable multi-nucleon transfer reactions; however, in the case of populating the 4.03-MeV state in $^{19}$Ne the anticipated $^{15}$O yield is also very low. In this instance these reactions may contribute a large proportion of observed events. Another helpful consideration is that these reaction products will likely scatter at large angles or attenuate in the gas cell, such that these nuclei would not stop in the catcher foil. This may help prevent the extra $\beta^+$ particles from reaching the NaI(Tl) detectors. The background from the HAVAR entrance window will be characterized by running the $^{19}$F beam on the gas cell void of hydrogen gas.

There is also another gas-related reaction channel that may contribute to higher $^{15}$O yields: the $^{1}$H($^{19}$F,$\alpha$)$^{16}$O$^*$(n)$^{15}$O reaction. In this scenario the beam reacts with the hydrogen target and populates neutron-unstable states in $^{16}$O that can decay into $^{15}$O. Using reasonable estimates for the partial decay widths involved,

we estimate that the yield from the desired reaction channel is larger, by factors of $10^5$ - $10^7$, than the $(p,\alpha)(n)$ reaction channel described above.

The observed $\gamma$-ray background may also display contributions from the materials in the facility surrounding the experiment. Many common building materials contain some abundance of radioactive isotopes. The background $\gamma$-ray energies and count rates summarized in Table 2.2, were acquired from Knoll's "Radiation Detection and Measurement" textbook [39]. These spectrum data were generated using a 60 $cm^3$ Ge detector situated above the ground. Data had been recorded for 170 h [44].

| Source | $\gamma$ Energy [keV] | Count Rate [$min^{-1}$] |
|---|---|---|
| $^{214}$Pb | 295.2 | 3 |
| $^{212}$Pb | 301 | 2 |
| $^{214}$Pb | 352.0 | 3 |
| $^{228}$Ac | 410 | 1 |
| $^{125}$Sb | 427.9 | 1 |
| $^{228}$Ac | 463 | 1 |
| $^{7}$Be | 477.5 | 0.7 |
| $^{208}$Tl | 510.7 | 1.2 |
| $^{208}$Tl | 511 | 1.2 |
| $^{106}$Ru | 511.8 | 1.2 |
| $^{208}$Tl | 583 | 1.5 |
| $^{214}$Bi | 609.3 | 1.8 |
| $^{137}$Cs | 661.6 | 1.2 |
| $^{212}$Bi | 727.2 | 0.5 |
| $^{228}$Ac | 911 | 0.8 |
| $^{228}$Ac | 969 | 0.5 |

Table 2.2: Terrestrial Background $\gamma$-Ray Sources

Omitted from this table are the data with $\gamma$ energies less than 300 keV despite typical count rates that exceed 5 $min^{-1}$. This region displays many $\gamma$ activity peaks from various sources, the common ones being $^{228}$Ac, $^{235}$U, $^{212}$Pb, K, and Th. These data were not included as they exist in the region in the detector spectra that will be dominated by the Compton Shelf and is separate from the 511 keV peak of interest. Radioisotopes that are common in building materials are K, Th, U, and Ra. Fortunately these sources do not have significant activity rates in the relevant energy regime, and are unlikely to interfere with 511 keV signature of the $^{15}$O $\beta^+$

activity.

Several solutions exist that may be implemented during or after these experiments that can mitigate the effects of background radiation. The background due to Foil-Beam interactions can easily be characterized before the data collection takes place. This will be done by removing the gas cell and measuring the 511 keV activity from the tantalum catcher foil alone. The beam energy will have been adjusted to replicate production conditions before hand. Continue to introduce the gold foil and subsequently, the HAVAR foil. This approach would generate the contribution to the 511 keV from each foil separately as well as in concert. Background characterization could also be done periodically during the experiment if there were concerns that the windows were degrading.

Lead blocks will also be placed within the vacuum chamber between the gas cell and detector crystals. This must be done, obviously, before characterizing the 511 keV background from the foils. This may help to shield any 511 keV activity from the reaction site as well as from outside sources in the ATLAS facility. The standing $\gamma$-ray background from ATLAS must also be determined by collecting data without beam. If the data in Table 2.2 are comparable to what will be observed at ATLAS, then there is little concern that there will be any significant $\gamma$ signature at 511 keV. Another method to reduce the 511 keV background will be to make $\gamma$ - $\gamma$ coincidence measurements between the two detectors. As it is very unlikely that two extraneous 511 keV photons will simultaneously deposit all their energy in the two detectors, we can assume with a high degree of confidence that coincidence events are the signature of an $^{15}$O nucleus from within the catcher foil. The detection efficiency of coincidence counting is discussed in Section 3.2.5.

To choose ideal design specifications related to the target and detection phases of the experiment, simulations have been performed that replicate the reaction process and detector response. Details of these are given in the next chapter.

Chapter 3

# Simulation

Creating accurate simulations is an essential tool for nuclear astrophysics experiments. It is often necessary to be able to demonstrate, via simulation, that the observations to be made in a laboratory setting can be achieved feasibly. The experimentalist has the goal then to accurately model the laboratory environment in computer code, such that the prediction made by simulation will be as similar as possible to what will take place.

In this chapter a description of the simulations made to model the activity method approach will be given. Two simulations have been performed; the first was made to model the target reaction and energy distribution of the important reaction products and the second was generated to predict the detector response during the counting phase of the experiment.

## 3.1 Simulation of the $^{1}$H($^{19}$F,$^{19}$Ne)n Reaction

RUNSIM is a Monte Carlo simulation that was designed to digitally recreate the $^{1}$H($^{19}$F,$^{19}$Ne)n reaction that will take place in the experiments that will follow this project. Through the $^{1}$H($^{19}$F,$^{19}$Ne)n reaction excited states in $^{19}$Ne are populated and subsequently decay. The two excited states that will be incorporated are the 4.03-MeV and 5.35-MeV states. A previous version of this code contained the experimental geometry, the kinematics of the initial reaction and subsequent decays, range and energy loss calculations for ions in specified absorbers, and a n$^{th}$

order polynomial fitting routine for cross section data. Many alteration were made, however, to accommodate the necessary specifications of the test run phase of this project. This code operates in one of two possible batch modes. Both operating modes randomize the beam particle's energy, in the range of the gas cell target, at the moment of reaction. Kinematic calculations are performed to determine the decay products' energies and directions. Lastly, energy loss calculations account for the remaining length of hydrogen that must be traversed before entering the gold exit window.

The first batch mode, Mode-0, indicates whether or not the $^{19}$Ne decay products ($^{19}$Ne$_{g.s.}$ and $^{15}$O) were energetic enough to pass through the gold exit window of the hydrogen gas cell. Mode-0 uses range data procured from TRIM [45] simulations to interpolate the range of either decay ion based on its energy upon entering the exit window. If the gold thickness is greater than the calculated range, the ion's energy is set to 0 MeV indicating that the ion was stopped. Otherwise, the energy is set to 1 MeV indicating transmission. This method is used to count transmitted ions and determine a gold thickness that blocks all unwanted $^{19}$Ne$_{g.s.}$ ions.

The second batch mode, Mode-1, is characterized by calculating the specific energy loss of all ions in the exit window. This mode is capable of outputting the remaining energy and direction of the ions beyond the hydrogen gas cell's exit window. Through operation in Mode-1, the simulation predicts a size and thickness of the catcher foil that will stop all decay products before the detection phase.

### 3.1.1 Modifications for the 5.35 MeV Excited State

The experimental test run phase of this measurement technique requires the population of the 5.35-MeV excited state in $^{19}$Ne. This state gives an ideal test of the activity measurement technique as the $\alpha$-branching ratio of the 5.35-MeV state is approximately 1 [22]. The time required to acquire sufficient statistics, therefore, is roughly a factor of $10^4$ less than for the 4.03-MeV state. To accommodate the higher test run energy requirements various changes needed to be made so that the RUNSIM code can properly simulate the experiment.

The $^{19}$F beam energy before the gas cell entrance window had to be increased so that population of the 5.35-MeV level was energetically possible. Special care was

also taken in choosing the beam energy so that is was impossible to populate the next highest excited state in $^{19}$Ne (see Section 2.1.2).

Stopping power values were determined using the SRIM simulation software [45]. By indicating the projectile ion and the absorbing material details, SRIM outputs the nuclear and electronic contributions to the stopping power for a designated range of ion energies. So using the energy distributions determined in the Mode-1 operation, the stopping powers were found for the relevant energies for the two possible decay products.

Altering the range data for each ion was the most time consuming of the modifications that needed to be made. Beginning with the ion energy distributions directly before the gas cell exit window, the energy extremes were determined (see Section 3.1.2). Using the TRIM software, simulations were performed to find the ranges of $^{15}$O and $^{19}$Ne$_{g.s.}$ for the maximum and minimum energies allowed. TRIM outputs a distribution of linear ranges for mono-energetic projectiles. Four outputs were generated and each was fit using the Origin7 data processing software. The fits for the four data sets are given in Figures 3.1 and 3.2.

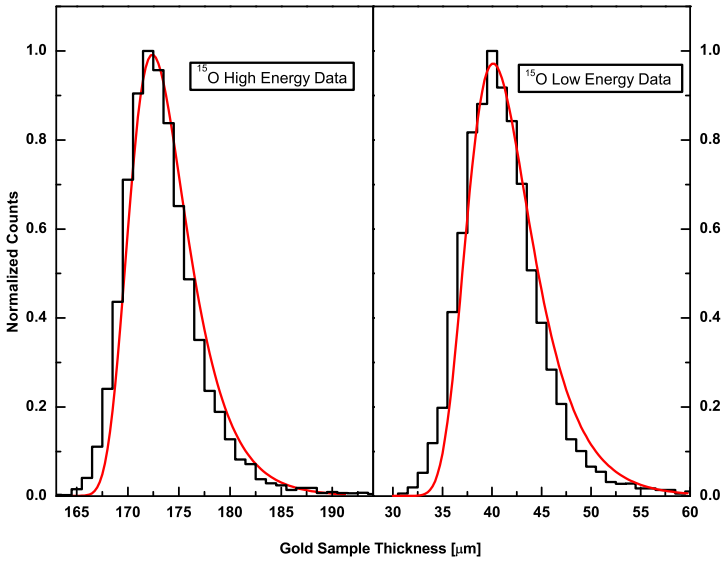


Figure 3.1: Histograms and fits of TRIM range data for $^{15}$O.

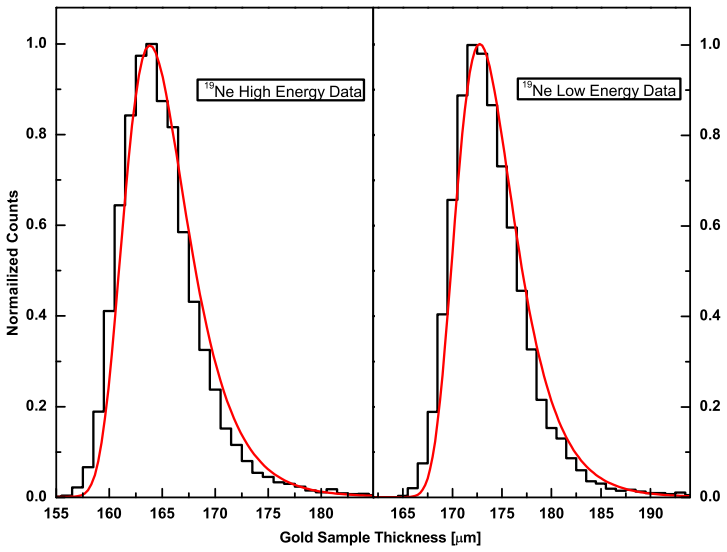


Figure 3.2: Histograms and fits of TRIM range data for $^{19}$Ne.

After these data were fit, the results were recorded and used as parameters for the Monte Carlo code. A description of the fitting function and its values are given in Appendix A.2. The horizontal axes indicate the distance that remains between the ion's range in the simulated sample and the sample's thickness; the ion range was later determined using these values. The fitting parameters were used while operating the code in Mode-0 to determine ion ranges in gold by calculating a linear relation between the extreme range data as a function of energy. From this relation, each simulated ion's range in gold could be interpolated. The recorded fitting parameters replaced the previously existing ones corresponding to the lower excitation energy situation.

Another alteration to the Mode-0 operating style was made to produce geometric efficiency estimates of the proposed detector setup. The schematics of the experiment and detector setup were used to supply geometric information. It was then assumed that any ion that exited the gold exit foil would be stopped at the center of the catcher foil and decay by $\beta^+$ emission. The $\beta$ particle was assumed to annihilate with an atomic electron in the catcher material and create two back-to-back 511 keV $\gamma$-rays. Based on the setup geometry, the solid angle coverage of the

detector about the catcher foil was calculated. The $\gamma$-rays were emitted isotropically and if they fell within the detectors' solid angle, they were counted as a hit. By this method the geometric efficiency of the detectors could be estimated.

### 3.1.2 Energy Distributions of $^{15}$O and $^{19}$Ne$_{g.s.}$

To determine the linear range of the decay products in the gold exit window the extremes of the energy distributions had to be acquired. After running the simulation in Mode-1 the energies of both $^{15}$O and $^{19}$Ne$_{g.s.}$ immediately before the exit window were tabulated and plotted in histograms. The two histograms present the data from four executions, or runs, of the simulation with $10^4$ events in each. A separate run was done for the two decay products from both the 4.03-MeV and 5.35-MeV excited states. The energy distributions are given in Figures 3.3 and 3.4, respectively.

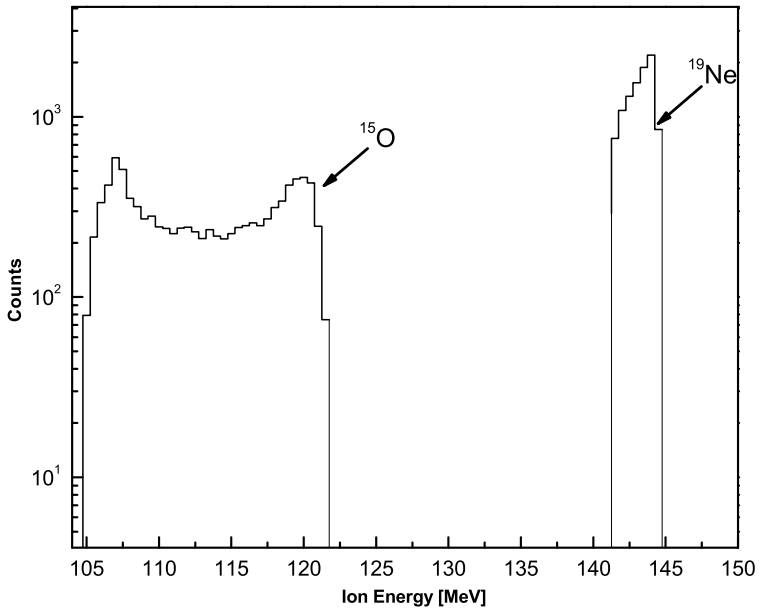


Figure 3.3: Energy distributions of the $^{15}$O and $^{19}$Ne$_{g.s.}$ ions before entering the exit window. These data are the results of populating the 4.03-MeV level of $^{19}$Ne.

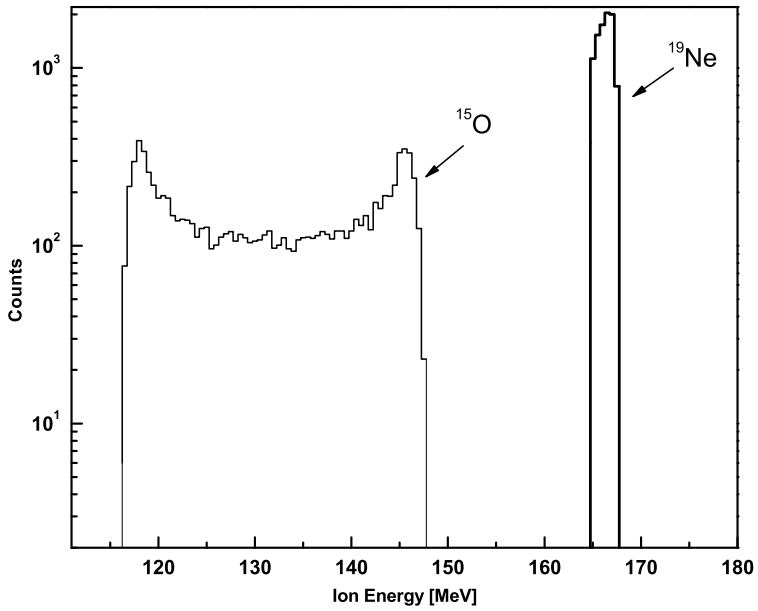


Figure 3.4: Energy distributions of the $^{15}$O and $^{19}$Ne$_{g.s.}$ ions before entering the exit window. These data are generated by populating the 5.35-MeV excited state of $^{19}$Ne.

The significant results from Figures 3.3 and 3.4 are summarized in Table 3.1. These bounds on the energy were then used as input parameters for TRIM simulations to attain range data fitting parameters for the monte carlo code to calculate ranges for ion energies between these limits. Another feature of note is the bifurcation in the $^{15}$O energy distribution which is a result of having two kinematic solutions to one set of initial reaction conditions.

| Excited State of $^{19}$Ne | Daughter Nucleus | Minima - Maxima |
|---|---|---|
| 4.03 | $^{15}$O | 104 – 122 $MeV$ |
| | $^{19}$Ne$_{g.s.}$ | 141 – 145 $MeV$ |
| 5.35 | $^{15}$O | 116 – 148 $MeV$ |
| | $^{19}$Ne$_{g.s.}$ | 164 – 169 $MeV$ |

Table 3.1: Energy extrema for the 4.03-MeV and 5.35-MeV excited states of $^{19}$Ne.

### 3.1.3 Ion Ranges in Gold

A linear fit between range values and distribution widths provide a means for interpolating range data for ion energies in between the maxima. Figure 3.5 gives a graphic representation of the linear fit. The probability of ions passing through the gold exit window is estimated by operating RUNSIM in Mode-0, the gold thickness is then adjusted such that the probability of $^{19}Ne_{g.s.}$ ions is zero. At this thickness of gold we can minimize the 511 keV background from the $\beta^+$ decay of $^{19}$Ne and isolate the activity that is observed from $^{15}$O nuclei. This thickness of gold, however, also results in a reduction of the $^{15}$O yield. This effect on the $^{15}$O yield will be quantified later in this section.

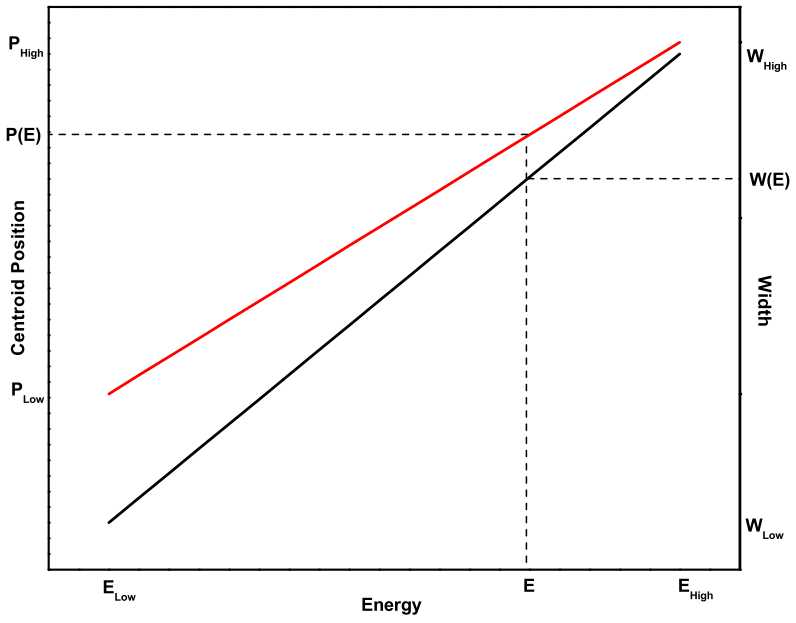


Figure 3.5: Linear range-fitting routine. Ion ranges and distributions are interpolated using extreme cases.

The gold exit window must be constructed with a mass thickness that exceeds that which stops the $^{19}Ne_{g.s.}$ nuclei. To first estimate this mass thickness, the range distributions of $^{15}$O and $^{19}Ne_{g.s.}$ in gold from the 4.03-MeV and 5.35-MeV excited states are shown in Figures 3.6 and 3.7, respectively.

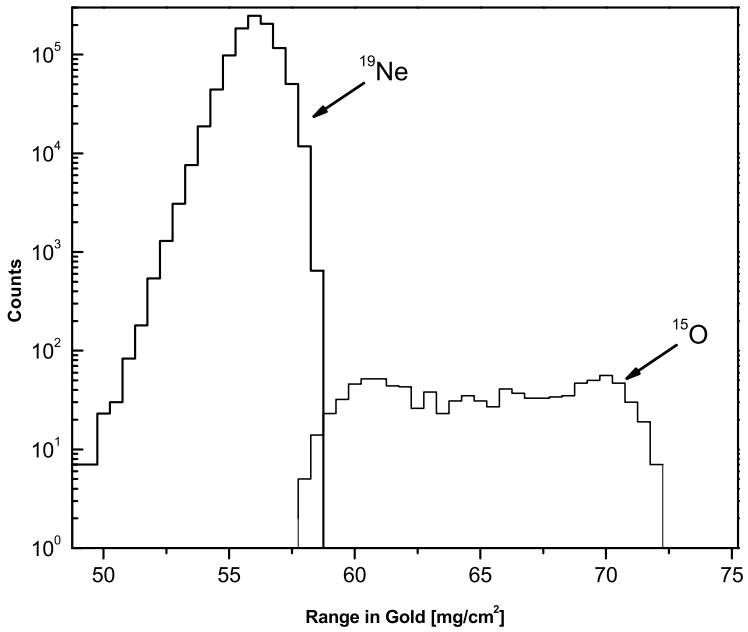


Figure 3.6: Ion ranges in gold, in mass thickness, for ions from the decay of the 4.03-MeV excited state of $^{19}$Ne.

From these range data, an estimate of the appropriate thickness of gold in the exit window is taken as the thickness for which no $^{19}\mathrm{Ne}_{g.s.}$ ions are observed. From the plots we see that thicknesses of 59 and 70 mg/cm$^2$ are sufficient to stop the $\gamma$-decay product ($^{19}\mathrm{Ne}_{g.s.}$) of the 4.03-MeV and 5.35-MeV excited states of $^{19}$Ne, respectively. Using these estimates the simulation can be run for gold foil thicknesses that are less and greater than those proposed to examine the transmission of each decay product as the thickness varies. The results of these simulations are as follows.

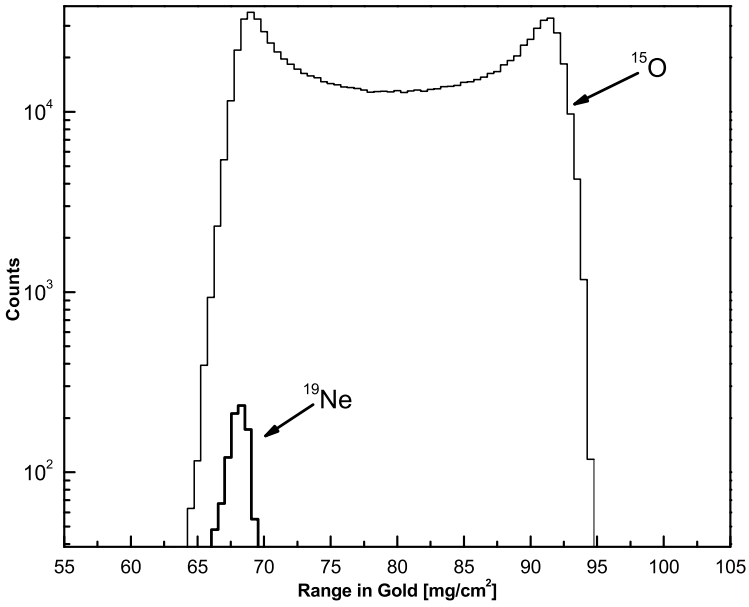


Figure 3.7: Ion ranges in gold, in mass thickness, for ions from the decay of the 5.35-MeV excited state of $^{19}$Ne.

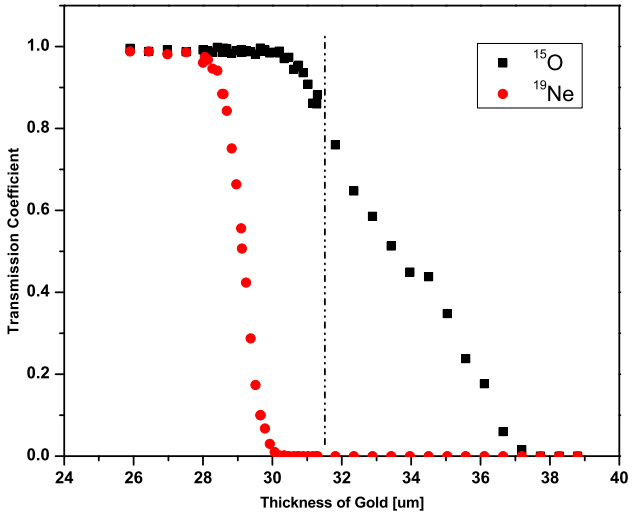


Figure 3.8: Transmission coefficients of decay products from the 4.03-MeV excited state as the gold foil thickness is varied. The Dot-Hash line marks the suggested exit window thickness to block $^{19}$Ne$_{g.s.}$ transmission.

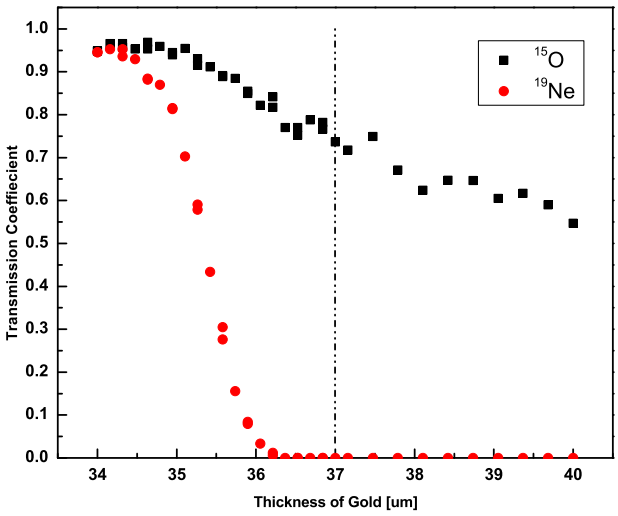


Figure 3.9: Transmission coefficients of decay products from the 5.35-MeV excited state as the gold foil thickness is varied. The ideal gold thickness is indicated.

These data were determined by simulating $10^4$ events for each decay product for various gold foil thicknesses in the range shown in the plots. Transmission coefficient trends provide a more precise recommendation of the ideal gold foil thickness. We can choose a thickness that ensures no transmission of $^{19}Ne_{g.s.}$ ions and simultaneously maximizes the resulting $^{15}O$ transmission. The suggested values are 31.5 $\mu m$ and 37 $\mu m$ for the 4.03 and 5.35 MeV excitation energies, respectively. These transmission coefficients will be used to correct the yield of $^{15}O$ observed experimentally (see Section 5.2.1).

These thickness selections also take into account the uncertainty in the foil thickness. An uncertainty of $\pm$ 3% was assumed which implies an absolute uncertainty of $\approx$ 1 $\mu m$. The dot-hash lines are clearly placed, such that, a decrease of 1 $\mu m$ will not result in an increase of the transmission coefficient of the $^{19}Ne_{g.s.}$ ions above zero. An increase or decrease of this magnitude will, however, have a strong effect on the transmission of $^{15}O$ through the gas cell exit window. In reviewing transmission data, like those shown above, it was found that a $\pm$ 3 % uncertainty of the gold foil thickness results in a $^{15}O$ transmission uncertainty of +21/-14 % for the case of the population of the 4.03 MeV state. Similarly, in populating the 5.35

MeV excited state an $^{15}$O transmission uncertainty of +11/-7 % is observed. These uncertainties are expected to be the greatest precision limiting uncertainties of the $\alpha$-branching ratio measurement in our experiment.

### 3.1.4 Determination of the Detector Efficiency

The RUNSIM code has been adapted to be able to estimate the geometric efficiency of the detector setup. The arrangement consists of two sodium iodide (NaI(Tl)) scintillation detectors. The scintillator crystals are cubic with side lengths of 2.54 cm and are enclosed in 0.3 cm thick aluminum shielding. Note that crystal sizes were determined following considerations of the spatial constraints of the vacuum chamber in which they will be housed. Using this geometry and assuming a crystal orientation as given in Section 2.3.2, the detectors' solid angle was calculated. During the simulation the 511 keV $\gamma$-rays that arise from positron annihilation are emitted isotropically and those emitted within the detectors' solid angle are counted as hits. The ratio of hits to the number of $^{15}$O nuclei implanted in the catcher foil gives an estimate of the geometric efficiency of the detector setup.

This estimate relies on several important assumptions that limit its predictive accuracy. The first assumption is that all of the $^{19}$Ne decay products are stopped at the center of the catcher foil, i.e., the exit angles of these nuclei are 0° in the laboratory frame. The second assumption is that the $\beta^+$ particles annihilate immediately upon emission. Lastly, this estimate assumes that only one quarter of the 511 keV photons that reach the NaI detector crystals will deposit all of their energy. The data used to estimate the geometric efficiency of the detector setup were collected by simulations of $10^3$ events, setting the $\alpha$-branching to 0.5, and varying the exit window thickness. Fifty-two simulations produced detectable events and the detection efficiency of each simulation is plotted below.

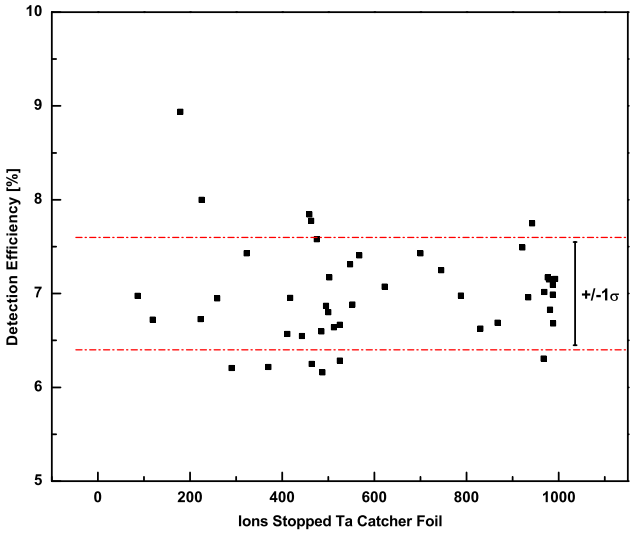


Figure 3.10: Detector efficiency *vs.* the total number of ions that pass the exit window and are stopped in the Tantalum catcher foil. The 1 $\sigma$ range about the mean efficiency is marked by the red dotted lines.

From Figure 3.10, one sees then that the geometric detection efficiency of our setup is 7.0 $\pm$ 0.6 %. Of all 52 simulations that contributed to this plot, 39 produce efficiency estimates that fall in the $\pm$ 1 $\sigma$ range (i.e. 75 %). Deviations from the mean efficiency are a result of exit window thicknesses that stop nearly all ions resulting in low detection statistics. The two most extreme deviations, not shown in Figure 3.10, are estimates of 12.5 and 3.5 %. The precision of this estimate could be improved by increasing the simulation size as the gold foil thickness is increased. Since, however, this is merely an estimate of the detector efficiency, corrections to thick gold foil effects seems unnecessary. A more comprehensive determination of the detection efficiency is given by Geant4 simulation, which will be described in the following section.

## 3.2 Detector Simulation With Geant4

The GEANT4 simulation package has arisen out of the need of nuclear and particle physicists to have a robust and accurate means of computationally representing increasingly complex experimental system and detectors [46]. This toolkit is

written in the C++ framework and contains a diverse class system that is used to create a simulation from beginning to end. The user is required to specify certain class categories that specify the unique geometry, particles involved, and physical processes that need to be included.

For the purposes of this project GEANT4 has been used to simulate the detection phase of the proposed experiment. GEANT4 provides a convenient way of dealing with all the necessary physical processes involved with $\beta$ decay of the relevant $^{15}$O nuclei as well as the response of the sensitive detector material to photon interactions. In the following, the GEANT4 framework will be described.

### 3.2.1 Geant4 Class Structure

The GEANT4 toolkit is capable of tracking particles through materials and computing continuous energy losses and interactions. The user is required to specify the materials and geometry of the setup, the primary particles involved, and the list of physical processes needed to describe all relevant interactions. Once this information is set the GEANT4 kernel provides a treatment of particle tracking, management of digitization and hits, event and track data, visualizations, and, lastly, a user interface.

Many of the predefined GEANT4 classes are "abstract", which allows the user to define or redefine their functions and variables to suit their specific needs. Optionally, the user has the ability to specify the actions taken by the simulation at the beginning or end of each event or run. The user is also capable of specifying the actions taken in regards to storing data at each step or track of a particle, which may include calculating energy depositions or particle positions. For the purposes of this project the GEANT4 toolkit's ability to simulate a scintillating material's response to the annihilation activity of positrons is of particular interest. The hierarchical structure of the GEANT4 class structure is given in Figure 3.11 below.

Categories at the bottom of Figure 3.11 are used by those at higher levels. The organization of these categories can be compared to that of any structure, in which those on the bottom provide foundation and support for those above. While categories higher up in the framework have roles that are for higher functionality; like communication with programs outside GEANT4. The categories will be described briefly from the bottom up.

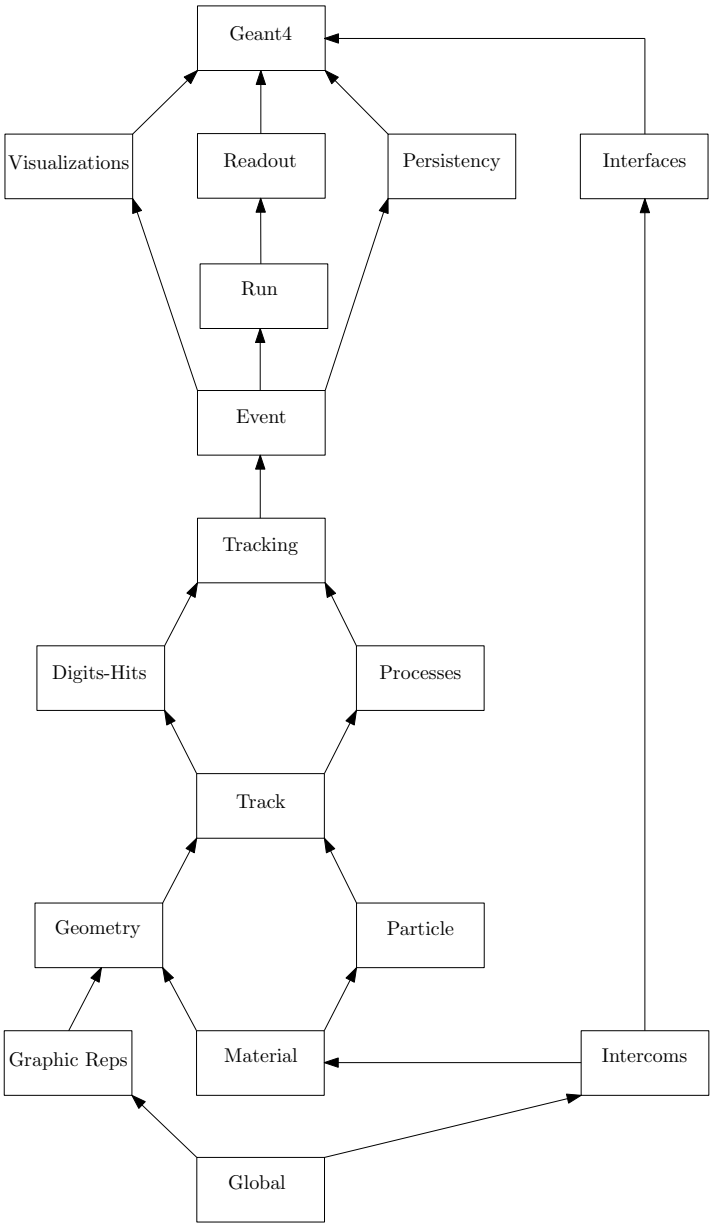


Figure 3.11: Class Category Diagram of the GEANT4 toolkit. The adjoining arrows of each category point to the category that uses it.

The foundation of the GEANT4 structure begins with the Global category that is responsible for controlling units, supplying standard constants, and handling of random numbers. All of the classes and functions needed to describe physical volumes in the detectors and navigate in the geometric model are contained in the Materials, Particles, Graphical Representations, and Geometry categories. Also in the foundation of this design is the Intercoms category which contains functions

responsible for communications between the various categories and class levels.

With these tools in hand, GEANT4 has the ability to describe the geometric space and material types, and to pass information upwards. It can now make use of the categories responsible for the tracking of particles through materials with various physical processes. The Tracks category contains the classes needed to describe the steps and tracks of a particle propagating through a material. Tracks is then used by the Processes category which implements the physical models that describe the interactions each particle can experience along a track or step. Lastly in this group, the Tracking category can invoke the Process category and manages the contribution of the processes involved to a track's state. Tracking may also pass information of sensitive detector volumes for Hits and Digitization.

Now that a particle's path can be described, the Event category has classes responsible for managing the collection of tracks and combining them. The Run category then manages the collection of events that share a common beam type and detector implementation. The Readout category allows the simulation to perform the compilation of run data. At the top level we have three categories that make use of all others below them and are responsible for connecting with facilities outside of the GEANT4 toolkit. These consist of the Visualization, Persistency, and (user) Interface categories. A more complete description of the Geant4 class structure is contained in reference [46].

### 3.2.2 Description of NaI Detector Simulation

The GEANT4 simulation of the response of the NaI detectors was needed, primarily, to accurately calculate the efficiency of the detector arrangement so that experimental data could be corrected for geometric or intrinsic losses. The simulation is also needed to determine an ideal thickness for the tantalum catcher foil, i.e., a length that would maximize the observed $^{15}$O activity.

To understand the function of the simulation it is best to describe the physical processes involved in the detection and counting phase of the experimental setup. This process begins when the nuclei, that are energetic enough to pass through the gold exit foil of the gas cell, are stopped by the tantalum catcher foil. During the experiment, following some preset exposure time ($\approx$ $^{15}$O half life of 122 s) the catcher

foil will be rotated away from the beam line and into the space between the two NaI detectors.

As $^{15}$O is unstable and decays via the weak interaction it is allowed to $\beta^+$ decay, and this $\beta$ activity is the fundamental mechanism for which $^{15}$O nuclei are detected. As the positron travels through the tantalum foil it losses energy and eventually annihilates with an atomic electron. This annihilation is characterized by the production of two 511 keV photons that travel in opposite direction to each other. These photons will be identified by a sharp peak in the energy spectra of a NaI detector, and it is in counting these events that we determine the yield of the $^{15}$O nuclei.

The simulation has been made to resemble the physical situation as closely as possible. This begins with generating the primary particles, $^{15}$O nuclei, with zero momentum inside the tantalum foil in a randomized configuration that incorporates the expected energy and spatial constraints. The beam spot size of the $^{15}$O nuclei can be calculated from the reaction kinematics and by factoring in the straggling effects of the gold foil. The energy distributions that were determined in the Fortran simulations, described in the previous section, help determine the linear penetration depths of the incident $^{15}$O projectiles. This information is used to specify the space in the tantalum catcher foil in which $^{15}$O nuclei should be generated. The simulation specifies that the radius of the $^{15}$O beam spot on the catcher foil is $\sim$ 3 mm and the maximum penetration depths are $\sim$ 6 and 12 $\mu m$ for the population of 4.03 and 5.35 MeV excited states in $^{19}$Ne (see section 3.2.5). Figure 3.12 depicts the $^{15}$O placement for both cases.

### 3.2.3 Visualization of NaI Detector Setup

As mentioned in the previous section, the GEANT4 toolkit is capable of producing high resolution images of the volumes and detectors involved in a simulation. The following images are "heprep" files that were generated during a run. They can be made to display the wireframe image of the detector arrangement alone, as well as include particle trajectories and interactions. Figures 3.13 and 3.14 display the detector setup alone and the detector material interacting with the $\beta^+$ emission of $^{15}$O nuclei implanted in the tantalum catcher foil that is positioned between the

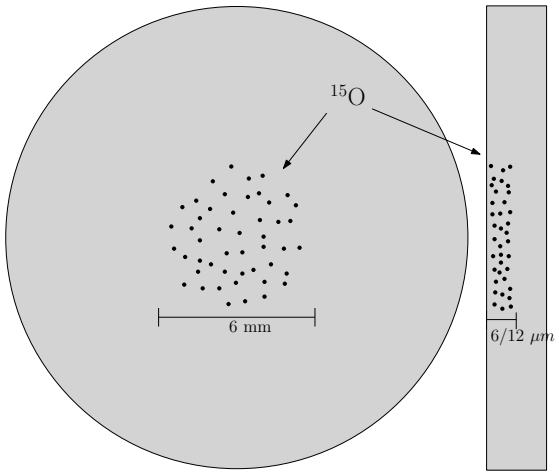


Figure 3.12: Schematic of Ta Catcher Foil with $^{15}$O placement.

detectors.

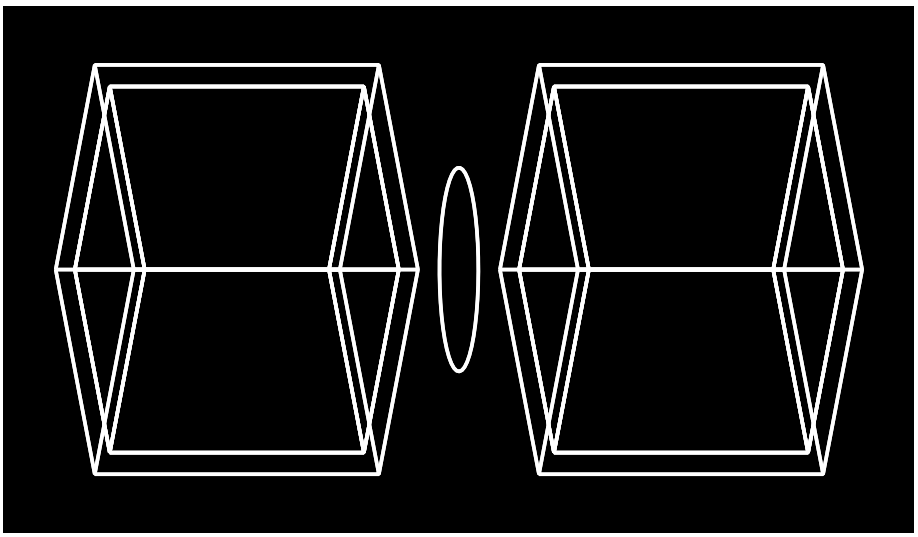

Figure 3.13: Wireframe representation of the two NaI crystals with the Ta catcher foil situated between them.

Depicted in Figure 3.13 is a wire-frame representation of the detectors as described in the Detector Construction class of the simulation. It shows the upstream and downstream detectors that are composed of a sensitive NaI cube surrounded by aluminum shielding. Between the two lies the tantalum catcher foil which has a thickness on the order of 10 $\mu m$. The image has been rotated to clearly demonstrate the three dimensional appearance of the image. The wireframe style of visualization was used so that interaction of positrons and photons could be seen more easily to

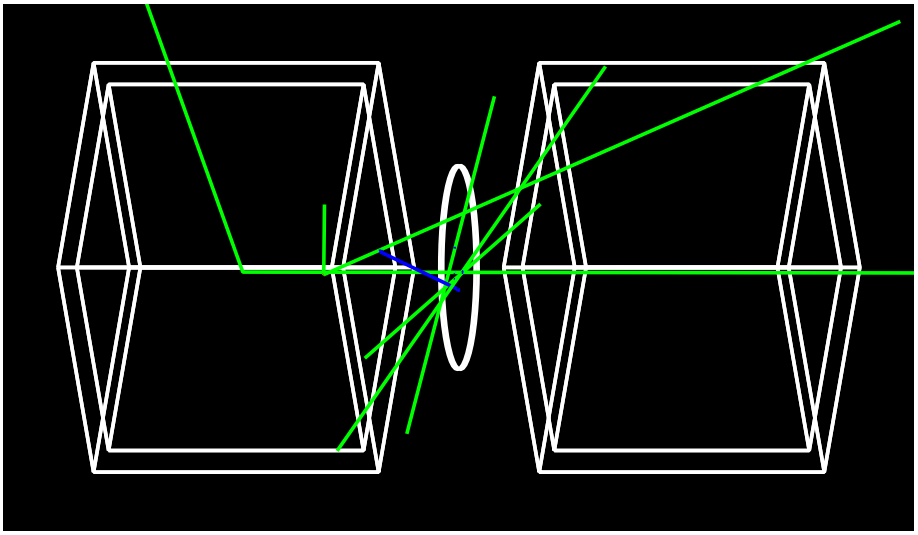

Figure 3.14: Detector geometry including visualization of ten $^{15}$O $\beta^+$ decay events.

check if the expected physical processes were included in the simulation.

The trajectories of ten events have been included in Figure 3.14. Green lines represent the tracks of photons and blue represents those of positively charged particles. The simulation begins by implanting $^{15}$O nuclei inside the tantalum catcher with a distribution that is similar to what would be observed during the experiment. The characteristic photons of the $e^+ + e^-$ annihilation are then shown to travel towards the detectors. The interactions of these photons with the detectors are shown as deflections or terminations of the trajectories.

The image has not been enhanced enough to depict the trajectories of the positrons within the catcher foil; however, a blue trajectory on the upstream (left) side of the foil is visible. This indicates that not all of the positrons annihilate within the tantalum foil. This is especially true in the case of the decay of $^{15}$O nuclei that were initially placed very near the surface of the catcher foil. The blue trajectory terminates when it reaches the aluminum shield and is then shown to produce the two characteristic photons traveling in opposite direction to each other.

Figure 3.14 also displays the trajectory of two mirror photons that do not travel in the direction of either detector. These photons will not contribute to the spectra created by either detector at the end of the simulation or, for that matter, in an experimental situation. During the simulation, however, these events are still taken into account and used to calculate the geometric efficiency of the detector

arrangement.

### 3.2.4 Detector Spectra

The simulation has been designed such that the total energy deposition for each event in the sensitive detector areas are accumulated and written to a file, for each detector. These data allow the user to generate histograms of the energy depositions so that the detector responses can be determined. By counting the number of 511 keV events in each detector we are able to determine the total efficiency of our detector arrangement. As the energy deposition data are written with the corresponding event numbers we can also count 511 keV photon coincidence detections in the two detectors. These coincidences are significant as they indicate with a high probability that the experimentalist has just observed the $\beta^+$ activity of an $^{15}$O nucleus, whereas non-coincidence events could potentially come from background sources.

Two example spectra are given in Figures 3.15 and 3.16. There is no significant difference in spectra for populating the two energy levels of $^{19}$Ne with the exception of the relative number of observed events in the 511 keV peak. Some variance is observed, however, due to the change in penetration depth of the $^{15}$O nuclei into the catcher foil for the higher and lower energy cases. This discrepancy may manifest itself as an increased likelihood of annihilation within the tantalum, and an increase in detection efficiency.

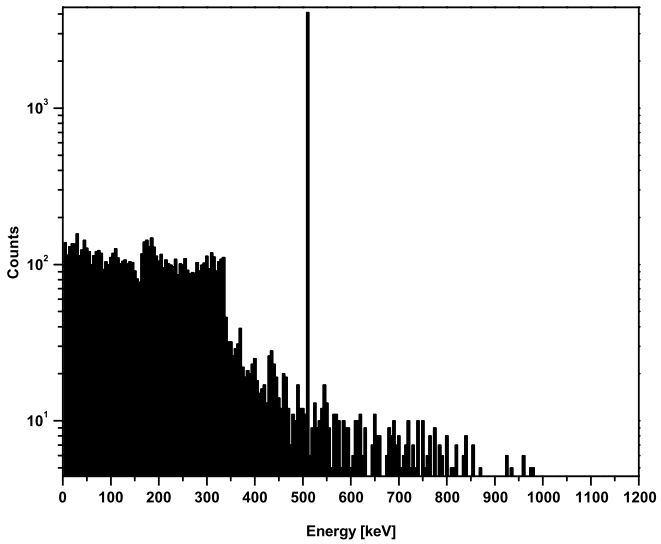


Figure 3.15: Spectra from the upstream detector.

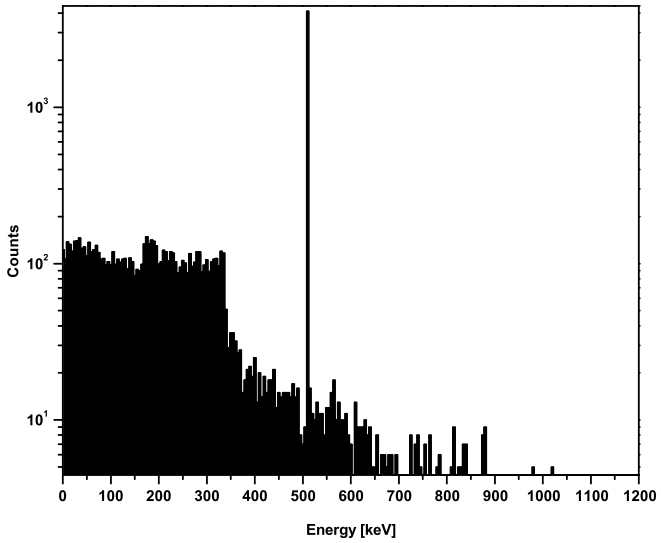


Figure 3.16: Spectra from the downstream detector.

These spectra demonstrate typical behaviours of intermediate-size scintillator crystals. We observe the Compton continuum in the energy range of 0 and 340 keV as well as the full photopeak at 511 keV. The energy gap between the Compton

edge and the photopeak is quantified as the difference between the maximum recoil electron energy and the photopeak energy, which is in this case expected to be 170 keV, in good agreement with the spectra. In this gap we see the effects of multiple Compton scattering which appears as the tapered region between the Compton edge and the incident gamma ray energy. As the incident photon energy is less than $2m_ec^2$ (1.022 MeV) the effects of pair production are not observed. These example spectra verify that the simulation is properly incorporating the physical interactions and processes involved in this measurement. It does not however incorporate typical peak-broadening effects of resolution limitations brought about by using NaI(Tl) detectors and the associated electronics.

The energy region beyond the 511 keV peak in the spectra is generated by multiple photon events in a crystal. These events can come about for two reasons. The first, positrons that escape the catcher foil and annihilate within the sodium iodide crystal can display an energy deposition greater than 511 keV. The second, a backscattered photon from one crystal can penetrate and interact with the other. Maximizing the likelihood of positrons annihilating within the tantalum catcher foil is a design concern. In the following section the effects on detection efficiency of adjusting the catcher foil thickness on observing 511 keV photons are examined.

### 3.2.5 Detection Effects of Adjusting the Catcher Foil Thickness

Choosing a thickness of tantalum for the catcher foil is another experimental detail that requires some care and thought. It may not be clear at the outset that using a foil that is thicker than the minimum required would have any effect on the subsequent measurement process but this possibility has been considered and the effects are discussed here.

Before considering the ideal thickness of tantalum, one must first determine the minimum amount that is needed to stop, or catch, all of the emerging $^{15}$O nuclei. From the RUNSIM simulation work, the energy distributions of the $^{15}$O nuclei are known. Along with the proposed gold foil thicknesses for the cases of populating the 4.03 and 5.35-MeV excited states of $^{19}$Ne, simple energy loss calculations can

be performed to determine the maximum kinetic energy of $^{15}$O that needs to be absorbed. This calculation was done with the Physical Calculator tool in the LISE++ software using energies of 122 and 148 MeV, and the gold foil thicknesses of 31.5 and 37 $\mu m$, respectively. The result is that we require a minimum thickness of 6 and 12 $\mu m$ of tantalum to stop the incident $^{15}$O nuclei. These lengths were included in Figure 3.12 without explanation.

To examine the effects of varying the catcher foil thickness the GEANT4 simulation was run for various lengths between 0 and 1000 $\mu m$, each with $10^5$ events. The number of events that deposit an energy of 511 keV in each detector was recorded. The plots in Figures 3.17 and 3.18 provide these results as well as the number of coincident events observed for each thickness., for the two $^{19}$Ne excited states relevant to our experiment. Note that efficiencies were calculated by comparing the number of observed 511 keV events to number of annihilation photons that are directed towards a particular detector. For example, a simulation with $10^3$ events should generate $10^3$ photons in both the upstream and downstream directions. In this example, if 50 511 keV photons were detected upstream, the efficiency would be 5 %.

Three simulations for each thickness were performed. The data points and uncertainties represent the mean and standard deviation observed within the three data sets. These data demonstrate that as the thickness of the tantalum foil increases beyond the minimum catcher foil lengths of 6 $\mu m$ and 12 $\mu m$ a disparity is created in the number of 511 keV events observed in each detector. The upstream detector, which faces the bombardment side of the catcher foil, observes more events while the downstream detector observes fewer. Interestingly the total number of detections seems to remain relatively constant through this process with total detection efficiency ranging from 8.0 to 8.6 %.

When reviewing these data it is important to consider that the center of the foil is always located at the middle point between the two detectors. As the thickness is increased we are effectively moving the implanted $^{15}$O nuclei towards to upstream detector and adding tantalum shielding between them and the downstream detector. This shift in ion placement relative to the detectors would imply that the upstream detector's solid angle coverage would increase and, conversely, the downstream detector's solid angle coverage is decreased. The data of Figures 3.17 and 3.18 also

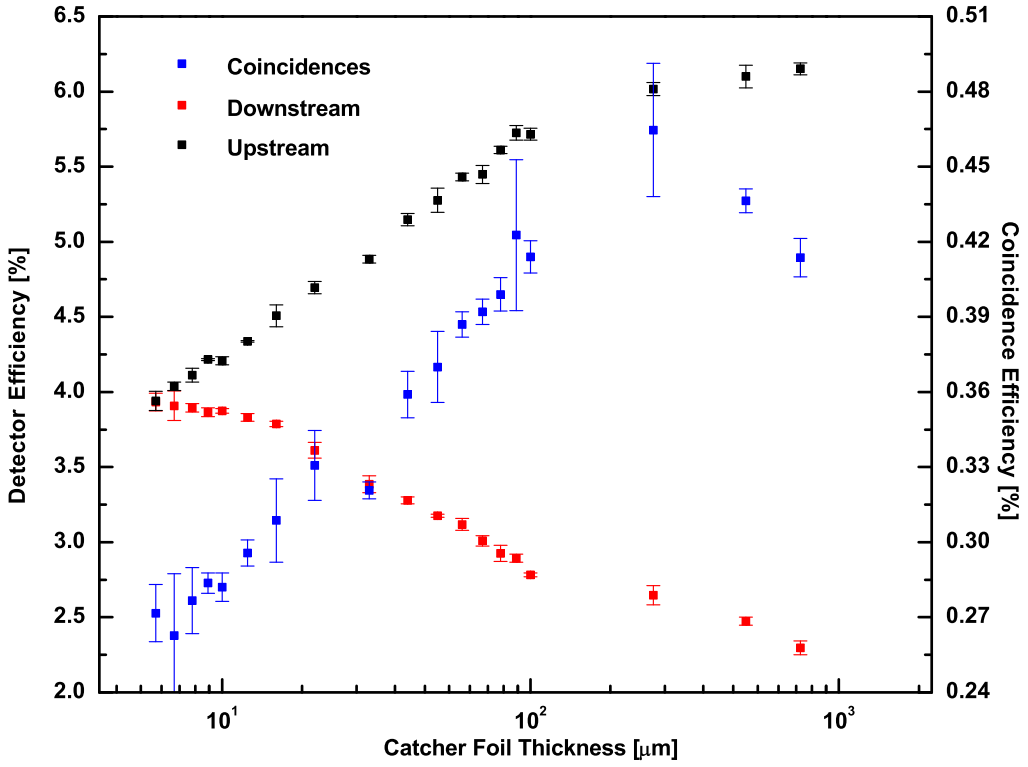


Figure 3.17: Detection and coincident efficiency for upstream and downstream detectors for the low energy case.

display an asymptotic behaviour of detected events as the thickness is increased, i.e. the upstream detector approaches a solid angle upper limit while the solid angle of the downstream detector approaches a lower limit. This suggests that the total solid angle coverage of the detector arrangement is fixed. In comparing the total detection efficiency predicted by the RUNSIM code, $7.0 \pm 0.6$ %, agreement is observed within the $2\sigma$ range. Considering that the RUNSIM code predicts only geometric efficiency coupled with an assumed 25 % likelihood of a full $\gamma$-ray interaction, the results agree within two standard deviations..

The total increase in detection efficiency in the upstream and downstream detectors cannot be completely accounted for by changes in the detector solid angles. There is another mechanism at hand that is responsible for the $\sim$ 50% change in efficiency that is observed over the whole tantalum thickness range. It was initially

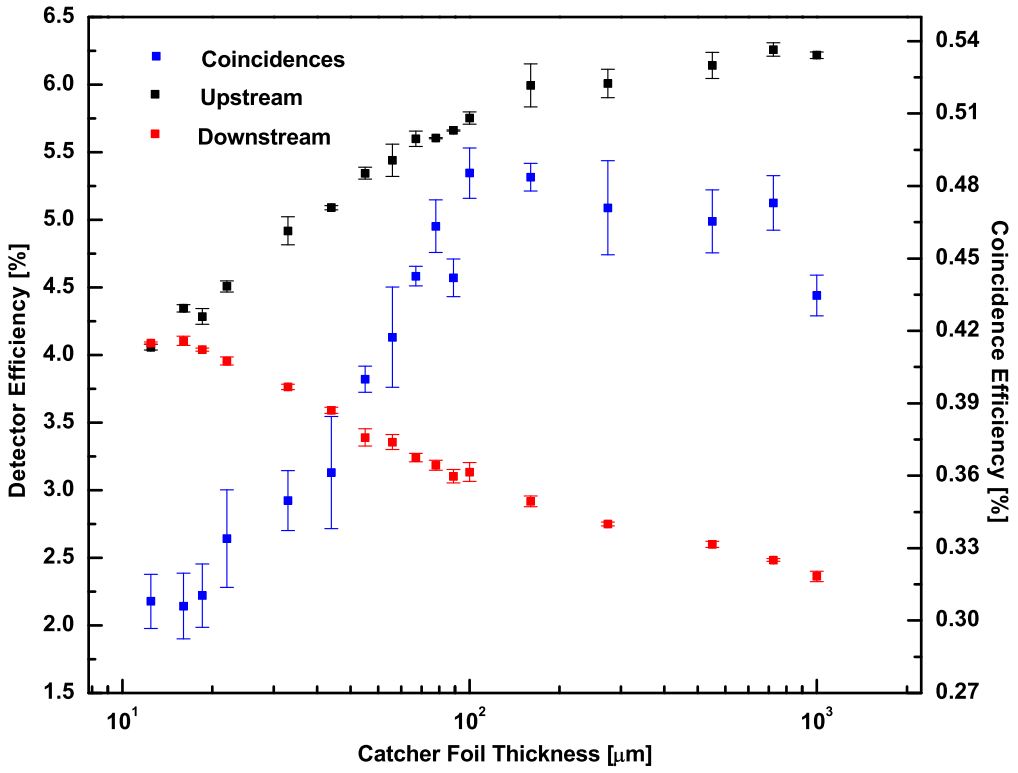


Figure 3.18: Detection and coincident efficiency for upstream and downstream detectors for the high energy case.

suspected that the large increase/decrease in efficiency was caused by positrons escaping the catcher foil and annihilating within a detector crystal. As the positrons are created via $\beta^+$ decay and are emitted with a distribution of energies below the $\beta$-decay Q-value they could not only deposit 511 keV of energy within the crystal, but could also generate 511 keV $\gamma$-rays within a crystal that are not likely to be observed in both detectors. With that said, increasing the catcher foil thickness increases the probability of positron annihilation in the upstream NaI(Tl) crystal and conversely decreases the probability of a similar event in the downstream detector.

This effect has been examined by simulating a 511 keV photon source within the tantalum catcher foil and producing a spectrum to subtract from the data used to generate Figure 3.18 to account for the effects of positron annihilation within the detectors. Presumably, once the total number of 511 keV events is reduced by the

amount due to photons generated within the tantalum, the remaining events are likely to be caused by positron interactions. This was done for two thicknesses of tantalum, 12.1 $\mu m$ and 250 $\mu m$, to generate a $\gamma$-ray spectrum for both the up and downstream detectors. The $\gamma$ spectra were normalized to the 511 keV photon peak in the $^{15}$O source spectra of the corresponding detector and tantalum thickness and were then subtracted from the $^{15}$O source spectra. It was assumed that all remaining detections, below the $\beta$-decay Q-value, were generated by positron interactions. For each case the total number of positron detections were counted and it was assumed that each of these generated two 511 keV $\gamma$-rays that fully deposited their energy and contribute to the detector efficiencies presented in Figure 3.18. The reduced $^{15}$O source spectra are presented in Figure 3.19.

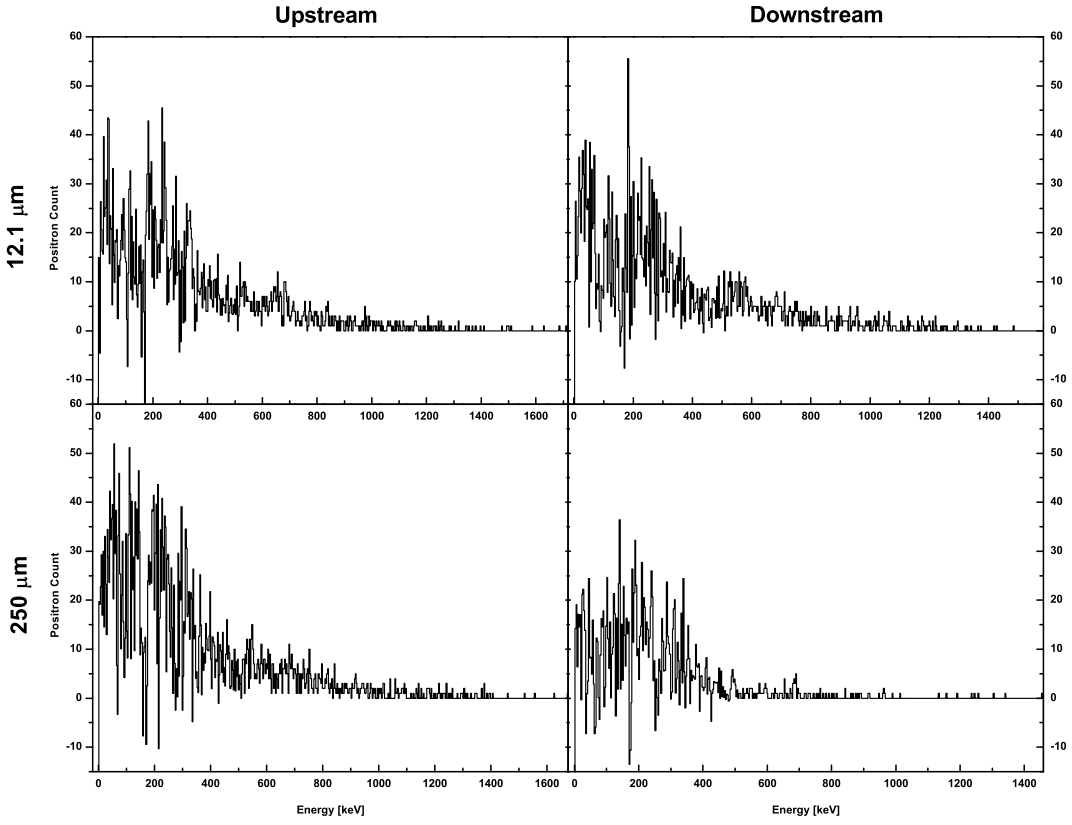


Figure 3.19: Reduced positron spectra corresponding to the data from Figure 3.18. Columns are labelled as Upstream or Downstream, rows are labelled as 12.1 $\mu m$ or 250 $\mu m$.

The upper left panel displays the (assumed) positron spectra for the upstream detector using a tantalum foil thickness of 12.1 $\mu m$; the reduced spectrum for the downstream detector with the same tantalum foil thickness is given in the upper right panel. The bottom left and right panels give the reduced spectra for the 250 $\mu m$ thick tantalum foil for the upstream and downstream detectors, respectively. The total counts of positron events for the case of 12.1 $\mu m$ thick tantalum for the upstream and downstream detectors are 3043 and 2904, respectively. Similarly, for the case of 250 $\mu m$ thick tantalum 3732 and 1500 events are observed in the upstream and downstream detectors, respectively. This indicates that 689 more positrons are observed in the upstream detector as a result of increases in the tantalum thickness from 12.1 to 250 $\mu m$. Assuming that each of these generate two $\gamma$-rays that fully deposit their energy, the efficiency would be expected to increase by $\sim 1.4$ %. By the same rationale, a downstream efficiency reduction of $\sim 2.8$ % is observed. Although these are not precisely equivalent to the changes in efficiency observed in Figures 3.18, this treatment seems to have qualitatively reproduced the effect of positron annihilation within the NaI crystals. The assumptions could be relaxed to produce results that may agree more closely with the efficiency changes that are shown in Figure 3.18 but these are more difficult to implement and little more information would be gained as a result. These results, however, agree well enough to support the fact that large changes in detection efficiency in the up and down stream directions should be expected for an increasing tantalum thickness that go beyond the effects due to solid angle coverage.

In the event of high background radiation during the experiment, coincidence measurements are made to distinguish relevant events from the background. If these types of measurements are made during the experiment the data in Figures 3.17 and 3.18 suggest that catcher foil thicknesses of 200 $\mu m$ and 100 $\mu m$ would be ideal to observe the most coincident events; 0.47 and 0.49 %, respectively. The probability of a coincident detection is generally given by the product of the individual efficiencies of the two detectors [9]. The detection efficiency data in Figures 3.17 and 3.18 suggest that the coincidence efficiency would peak at 0.19 % between 20 $\mu m$ and 60 $\mu m$ in both cases. It seems odd that not only are the coincidence efficiencies not greatest in the 20 to 60 $\mu m$ range but also that the observed efficiency is consistently

greater than expected for all catcher foil thicknesses. Considering that the detection efficiencies include many factors it is difficult to suggest a reason as to why the observed coincidence efficiency is greater than expected.

A final remark on coincidence detection is that this technique may miss many 511 keV events in either detector that would have been produced from an $^{15}$O $\beta^+$ decay. This loss in data can be corrected for by understanding the probability of coincidences taking place, but the experiment will take more time to attain the desired statistical significance of the measurement of the $\alpha$-branching ratio.

Chapter 4

# $\gamma$ Spectroscopy with NaI Detectors

The two NaI(Tl) scintillation detectors that are to be used during the experimental phases of this project have been characterized and tested. This was done in order to verify that the devices that will be used to observe $^{15}$O $\beta^+$ decays are in good working condition, according to the manufacturer's specifications. Various standard $\gamma$-ray sources have been used to also measure the resolution of the detectors at different $\gamma$-ray energies.

## 4.1 Photomultiplier Tube (PMT) Voltage

The two NaI(Tl) detectors are custom-built SCIONIX scintillation detectors. Their specifications, as outlined in Chapter 2, were given to the manufacturer such that these devices are compatible with the experimental setup at Argonne National Laboratory, where the experiments and test run will take place. These detectors contain a high voltage supply and spectroscopic amplifier. These serve to apply a bias voltage across the PMT's photocathode and anode, and to provide an initial amplification of the detector's output signal, respectively. While the settings of the spectroscopic amplifier can not be adjusted, the user has complete control over the high voltage bias on the PMT. The high voltage setting can be adjusted by a 20-turn potentiometer that is manually turned using a small flathead screwdriver, and ranges from 0 to 1500 V. A test voltage output that can be read by a digital voltmeter indicates, in real time, what the voltage is set to. These components can be seen in

Figure 4.1.

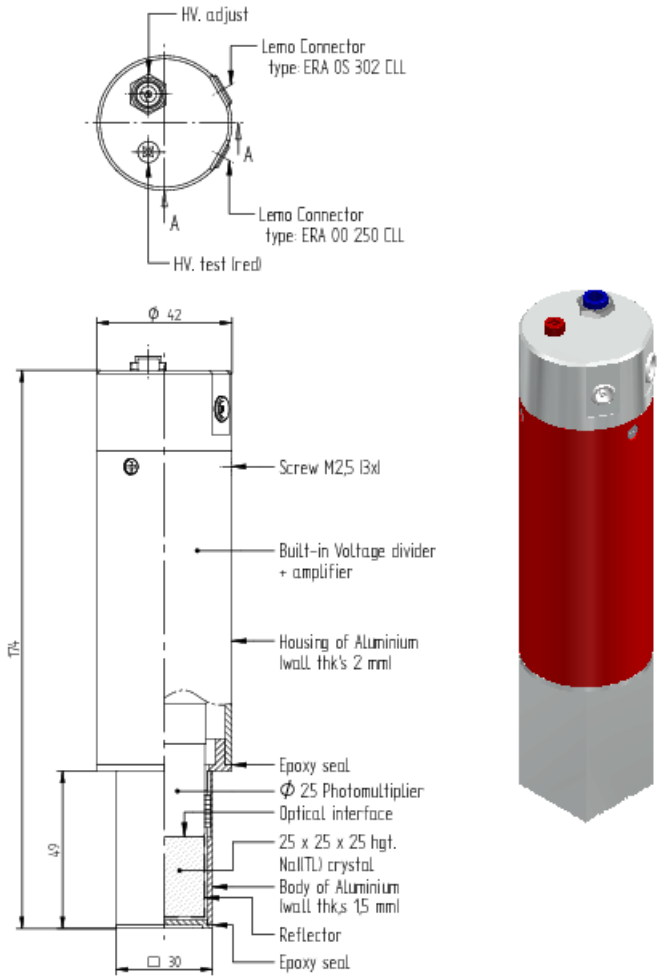


Figure 4.1: Schematic and 3D image of the NaI detectors. High voltage Adjust and Test controls are located on the PMT base. Measurements are given in millimeters.

This level of control is essential as the PMT voltage has a strong effect on the gain, total count rate and signal resolution [42]. It is relatively simple to determine the ideal PMT voltage that minimizes the detectors' dead time and enhances the

resolution of the signal so that $\gamma$-ray energies can be observed as distinct peaks in the spectra. This is done by measuring the total count rate from the detector and plotting these measurements as a function of the PMT voltage. Assuming a large enough region of PMT voltages is covered, the ideal "plateau" region can be identified [42]. For typical use, the PMT voltage should be set to the value at the middle of the plateau region. Using the entire energy range of room background as a source of radiation, this procedure was performed for the two detectors (referred to, hereafter, by their serial numbers, SFE759 and SFE760). The results are shown in Figure 4.2.

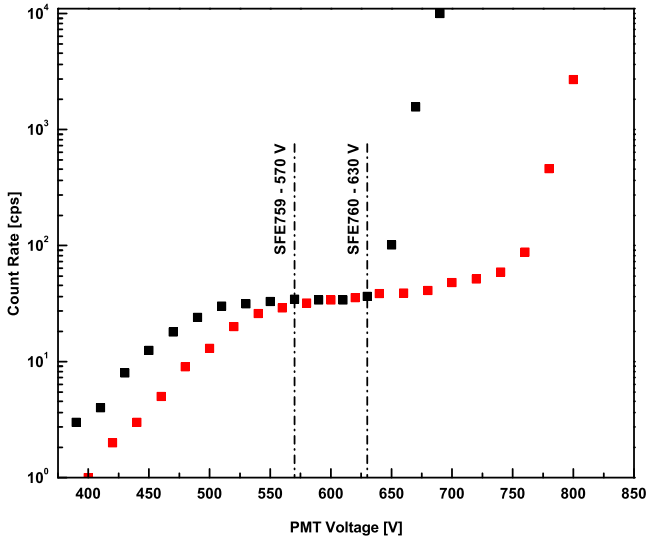


Figure 4.2: Room background count rates as a function of PMT voltage for the two detectors. Plateau mid-points are indicated for each detector.

The ideal PMT voltages are shown to be 570 V and 630 V for SFE759 and SFE760, respectively, though these voltages are not necessarily used for all applications. Depending on the environmental background and the activity (disintegrations per second) of the source, a different PMT voltage may be used to either increase or decrease the count rates of these detectors, which would result in an increase in resolution and decrease in running time, respectively. The fraction of dead time for the two detectors were also recorded and they ranged from 0 to 40% for both detectors and were only ever non-zero for voltages greater than the plateau values. At the PMT voltage of 570 V and 630 V the SFE759 and SFE760 detectors have a base-

line noise level of 20 mV and 25 mV, respectively, as measured by an oscilloscope. These baseline noise levels contribute to the overall resolution of the detectors; they represent the combined noise levels inherent in the detector and the ambient noise level in the environment in which they are operating. Other factors that contribute to the detector resolution are the intrinsic crystal resolution [47, 48] and statistical fluctuations in the outputs of the photocathode and electron multiplying system [42]. By comparing the noise levels observed in our lab to those observed at the ATLAS facility, we can gauge the effect on the resolution due to a change in environment.

## 4.2 Calibration

The output signal of the detector was processed by a digital Multi-Channel Analyzer (MCA) that is supported by the data acquisition software, Maestro30 (by Ortec). This software displays real-time data processing for the incoming signal. This was how the count rates, mentioned in the previous section, were measured. Maestro30 also displays the raw data in histograms that bin the events into channels, which directly correspond to a range in energy of the incident photons that interact with the NaI crystals.

By using known, long-lived, $\gamma$-ray sources (e.g. $^{137}$Cs, $^{60}$Co, and $^{133}$Ba) the relation between channel number and photon energy can be determined. An accurate calibration is necessary for source identification, especially when the source is an unknown isotope. For the purposes of this project, the 511-keV photopeak due to positron-electron annihilations will be the energy peak of interest. To this end, both detectors have been calibrated using the three sources mentioned above and then exposed to a $\beta^+$ source to see how closely the photopeak at 511 keV can be identified. Four $\gamma$ energy lines were used to calibrate the detectors. These energies and the corresponding sources are 80 keV, 356 keV, 1173 keV, and 1333 keV from the $^{133}$Ba $^{60}$Co sources. The calibration fit agreement was immediately checked with the $\gamma$ line at 662 keV from the $^{137}$Cs source. The calibrations for SFE759 and SFE760 are shown in Figures 4.3 and 4.4.

The peak positions were determined by fitting the energy peaks as Gaussian curves, the fit parameters of which, indicate the total area, centroid position, width

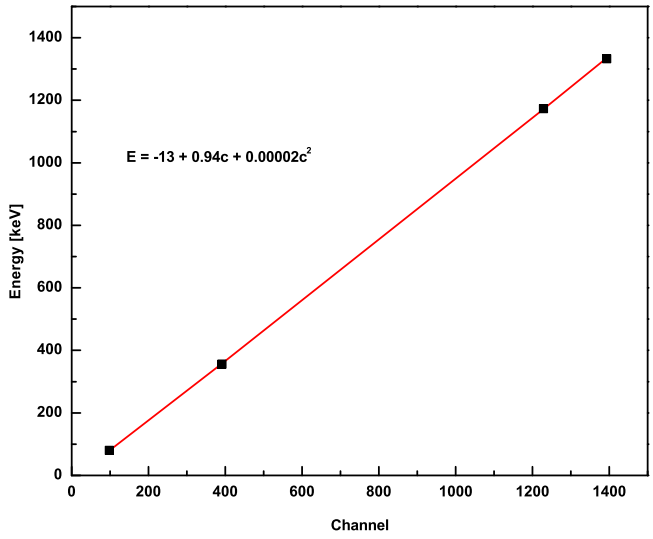


Figure 4.3: Energy-Channel calibration for SFE759.

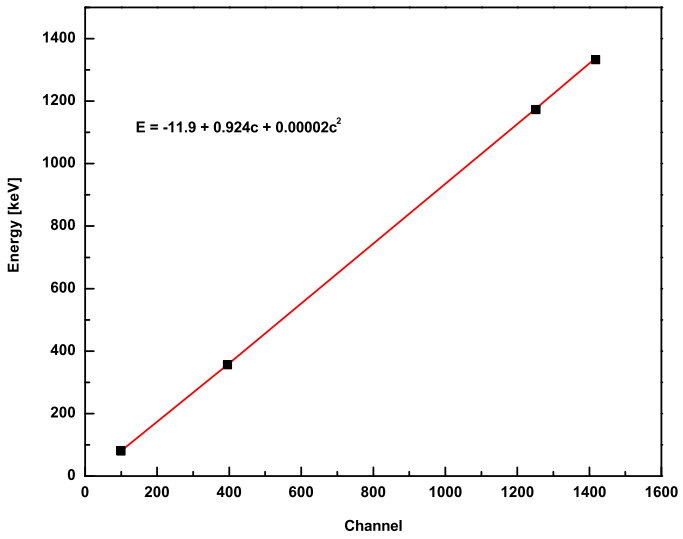


Figure 4.4: Energy-Channel calibration for SFE760.

and height. The centroids and their corresponding energies are plotted and fit with a polynomial curve of order 2 to provide an energy-channel relation. The coefficients of the quadratic term were both on the order of $10^{-4}$, indicating a near linear relation. For SFE759, the 662 keV energy peak was located at the position of 708.9. Based on

the calibration, this position corresponds to an energy of 663 ± 23 keV. This gives an excellent agreement and would allow this peak to be easily identified within the spectra. Similarly for SFE760, the 662 keV peak was located at the position of 717. Based on the calibration, this position corresponds to an energy of 661 ± 2 keV, once again in excellent agreement. Uncertainties for the interpolated energies of the 662 keV peak in each detector incorporated the uncertainties in the quadratic fitting constants. Uncertainties in the centroid positions are negligible in this example.

## 4.3 Response to 511 keV $\gamma$-rays

Sodium-22 ($^{22}$Na) is a $\beta^+$ emitter and is then a convenient $\gamma$ source at the energy of 511 keV. Spectra of the $^{22}$Na source, at the same PMT voltage used for the calibration, displays the 511-keV photopeak at channels 557.5 and 561.1 for the SFE759 and SFE760 detectors, respectively. Based on the detector calibrations, these positions correspond to energies of 517 ± 18 keV and 513 ± 2 keV, respectively. Figures 4.5 and 4.6 display the spectra from these two detectors as well as an indicator that denotes the 511-keV peak position and the resolution at that energy.

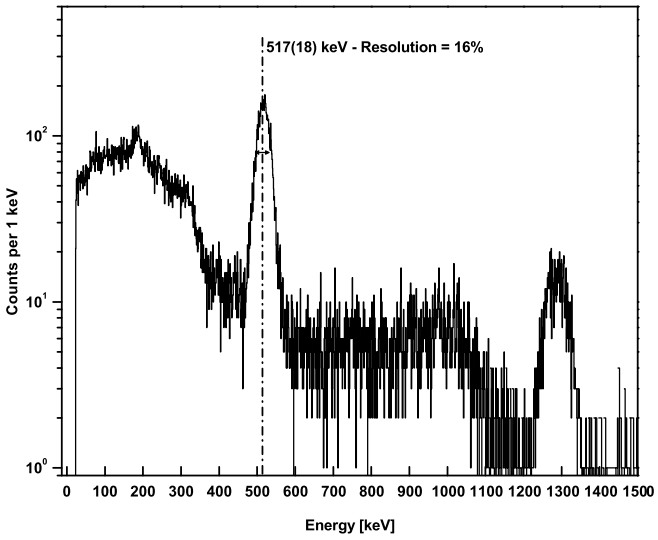


Figure 4.5: Spectrum from detector SFE759 using a $^{22}$Na source. The 511-keV peak found is at 517 ± 18 keV with a resolution of 16%.

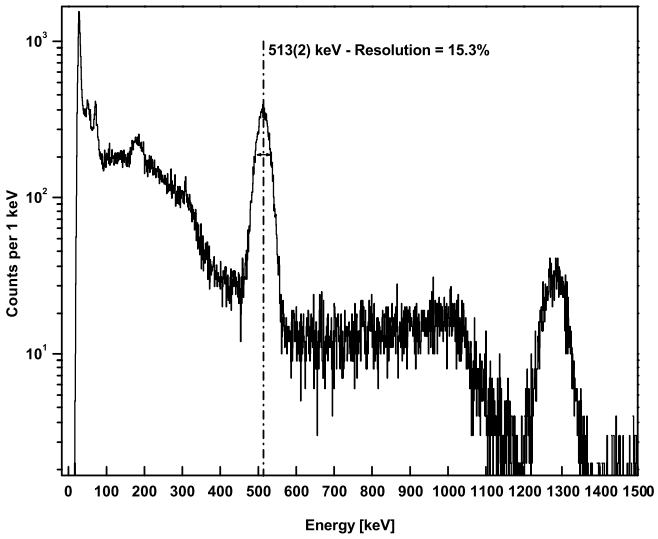


Figure 4.6: Spectrum from detector SFE760 using a $^{22}$Na source. 511 keV peak found at 513 $\pm$ 2 keV with a resolution of 15.3%.

The resolution of a detector is energy dependent and is an indicator for how precisely the detector, and the electronics it is coupled with, can measure the incident photon energy [42]. For a Gaussian distribution the resolution is determined by the ratio of the full width at half maximum (FWHM), which is the gaussian width at half the peak value, to the peak position. This expression is typically expressed as a percentage and is given by Eq. 4.1.

$$Resolution = \frac{FWHM}{E} = \frac{2\sqrt{2\ln 2}\sigma}{E} \tag{4.1}$$

where $\sigma$ is the standard deviation calculated during the peak fitting and $E$ is the centroid position in units of energy. Of the commonly used $\gamma$-ray detectors, scintillation detectors usually have the poorest energy resolution. A poor resolution typically results in broad peaks, as compared to detectors with high resolution [39]. The resolution can also be made worse for detectors that do not have a cylindrical crystal, which is the case for SFE759 and SFE760. SFE759 and SFE760 exhibit a resolution of 15 and 16 % which is high as compared to 6 % which has been observed in other NaI(Tl) detectors [48]. Since, however, the purpose of these detectors is to examine only the 511 keV $\gamma$-ray peak and not $\gamma$ spectroscopy, the reduced ability to resolve

photon energies should be inconsequential.

Once these detectors have been set into the vacuum chamber at Argonne National Laboratory's ATLAS facility, they will need to be characterized again. Calibrations will be performed routinely during the test run and experiment to ensure accurate peak identification and to check potential shifts in peak centroids.

Chapter 5

# Conclusions

Results and discussions have been given for the various experimental design features needed to determine the duration of the measurement of the $^{15}$O yield via the $^{1}$H($^{19}$F,n)$^{19}$Ne reaction. Specifically, the gas cell exit window thickness, catcher foil thickness and detection efficiencies have been determined for the two experimental cases where the 4.03-MeV and 5.35-MeV excited states will be populated. In this chapter a review of the results is given, along with a calculation of the expected yield of $^{15}$O nuclei. This calculation will provide an estimate for the amount of time needed for both cases for detecting a statistically significant number of $^{15}$O $\beta^{+}$ decays which will contribute to calculations of the $\alpha$-branching ratio for the 4.03-MeV state and subsequently the $\alpha$ partial width. Lastly, this chapter includes a discussion of the future work involved in this project.

## 5.1 Summary of Results

Drawing on previous information and discussion in Chapters 2 and 3, the following is a review of the design parameters that will be involved in the $^{15}$O yield calculations. Recall that in Section 2.1.2 the considerations around the choice of beam current and energy were given as well as the capabilities of the ATLAS facility. For the test run case, the $^{19}$F beam will have a current of 42 pnA (particle-nanoampere) and an energy of 160 MeV. For clarity, 1 pnA = $6.24 \cdot 10^{9}$ particles per second. Similarly, in populating the 4.03-MeV state a beam current and energy of 36 pnA

and 186 MeV are required, respectively. Currents were estimated by assuming a linear relation between beam energy and current within the ranges specified by the ATLAS facility (50 pnA at 114 MeV and 10 pnA at 334 MeV). The target mass thickness and gas pressure were discussed in Section 2.2.2. The results were that a hydrogen gas pressure of 130 Torr was needed to create a gas cell mass thickness of 0.23 mg/cm$^2$. This mass thickness was required to ensure that the 4.03-MeV excited state could be populated well within the gas cell and minimize the reduction in $^{15}$O yield due to energy losses in the gas cell.

Chapter 3 contained the descriptions and results of the simulation work that were performed to model the kinematics of the reaction process as well as the expected efficiencies during the detection phase. The ideal exit window thickness of gold was determined via Monte Carlo simulations of the $^{1}$H($^{19}$F,n)$^{19}$Ne reaction. The results of this work, given in Section 3.1 and the subsections therein, are that gold foil thicknesses of 31.5 $\mu m$ and 37 $\mu m$ are needed when populating the 4.03-MeV and 5.35-MeV excited states, respectively. Thickness of 31.5 $\mu m$ and 37 $\mu m$ in gold correspond to the mass thicknesses of 60.8 mg/cm$^2$ and 71.5 mg/cm$^2$. These thicknesses are assumed to have a 3% uncertainty associated with them; they have been selected such that the lower limit on the thickness would still stop all $^{19}$Ne$_{g.s.}$ from reaching the catcher foil. The thickness uncertainty leads to the largest source of uncertainties within the measurement due to its effect on the $^{15}$O transmission through the gold foil. The expected transmission coefficients of $^{15}$O nuclei are $80^{+21}_{-14}$% and $74^{+11}_{-7}$% for populating the 4.03-MeV and 5.35-MeV excited states, respectively.

Section 3.2 and the subsections therein, described the Monte Carlo simulations performed using the Geant4 toolkit that model the detector response to the $\beta^+$ activity from the decaying $^{15}$O nuclei that were implanted on the catcher foil. Section 3.2.5 discussed the effect on detection efficiency when varying the thickness of the tantalum catcher foil. Thicknesses of 200 $\mu m$ and 100 $\mu m$ are needed to maximize coincident detections between the two detectors for the cases of populating the 4.03-MeV and 5.35-MeV excited states, respectively. These two cases differ only in the fact that the maximum penetration depth of $^{15}$O nuclei into the catcher foil changes depending on the energy remaining after passing through the gas cell exit window. The coincident efficiencies appear to plateau in this thickness regime, as seen in

Figure 3.17 and 3.18, so more precise thicknesses are not reported here. These thicknesses also correspond to coincident detection efficiencies of 0.47 % and 0.49 %. When considering the individual detectors' efficiencies, upstream efficiencies of 5.7 % and 5.5 % are observed for the 200 $\mu m$ and 100 $\mu m$ thick foil, respectively. Downstream detection efficiencies of 2.6 % and 3.2 % are observed for the 200 $\mu m$ and 100 $\mu m$-thick foils, respectively.

These data will be used in the yield calculations to determine beam time requirements; the calculations are described in the following section.

## 5.2 $^{15}$O Yield and Beamtime Constraints

Counting $^{15}$O production is the main goal of the measurements described in this thesis. A prediction of this is needed before an experiment is performed, to demonstrate to project approval committees at accelerator facilities (ATLAS at Agronne National Laboratory, in this case) that the proposed experiment will be successful in a reasonable amount of time. The yield calculation has been performed for the test and experiment runs to determine the amount of beam time required to detect a statistically significant number of $^{15}$O $\beta^+$ decay events.

### 5.2.1 Calculating Yields

In brief, the production rate of $^{15}$O is estimated from cross section measurements, the beam current, target thickness and the approximate $\alpha$-branching ratios for the relevant excited states in $^{19}$Ne. The production rate is then adjusted to incorporate the loss of $^{15}$O nuclei due to transmission through the gold foil and $\beta^+$ decay for the various stages of collection and detection. The $^{15}$O production rate, $A(t)$ was given previously in Eq. 2.5 and is repeated here,

$$A(t) = I\sigma\rho\Delta t$$

. The rate of change in the number of $^{15}$O is given by the difference between the production rate and the $\beta^+$ activity

$$\frac{dN_{^{15}O}(t)}{dt} = A(t) - \lambda_{\beta+} N_{^{15}O}, \tag{5.1}$$

where $N_{^{15}O}$ is the number of $^{15}$O nuclei and $\lambda$ is the decay constant given by $\ln(2)/T_{1/2}$. The solution to this first order inhomogeneous differential equation is given by the sum of the homogeneous and particular solutions. Assuming a constant production rate and the initial condition that $N_{^{15}O}(t = 0) = 0$ the solution, and hence the activity, is given as,

$$\lambda_{\beta+} N_{^{15}O}(t) = A(t)\left(1 - e^{-\lambda_{\beta+} t}\right). \tag{5.2}$$

The functional form of this solution is an increasing curve that asymptotically approaches its upper limit. This expression will remain valid until the Ta catcher foil is removed from the "in-beam" location. It has been assumed that the time required to reach the Ta catcher is so much less than the $^{15}$O half life (122s) that the $^{15}$O nuclei reach the catcher at time t = 0. The transmission coefficient ($\xi$) of $^{15}$O through the gold foil is also introduced here as a scaling factor. Once the ideal exposure time ($t_0$) has been reached the catcher foil will rotate away from the "in-beam" position until it is situated between the two face-to-face NaI detectors. At the ideal exposure time, the activity expression changes to give the following form,

$$\lambda_{\beta+} N_{^{15}O}(t, t > t_0) = \xi A(t)\left(1 - e^{-\lambda_{\beta+} t_0}\right) e^{-\lambda_{\beta+}(t - t_0)}. \tag{5.3}$$

The effects of various stages on the activity can now be considered, i.e. the time needed for the Ta foil to rotate to the detector region and the counting time. Once the final activity is attained it can be used to determine the number of $^{15}$O nuclei present on the catcher foil or the number of disintegrations that will be observed during the counting time. By subtracting the activity at the beginning of detection from the activity at the end of the detection time and dividing by $\lambda_{^{15}O}$, we can calculate the number of disintegrations that took place during the detection time. As the two catcher foils rotate in opposition to each other, the detection and exposure time are equivalent. It is important then to determine what the ideal exposure/detection time is that maximizes the number of observed disintegrations.

The final expression that describes the number of disintegrations per cycle

($D$) has been determined and is given in Eq. 5.4.

$$D(t_c) = \frac{A\xi}{\lambda_{^{15}O}} e^{-\lambda_{^{15}O} t_r} \frac{\left(1 - e^{-\lambda_{^{15}O} t_c}\right)^2}{(t_r + t_c)} \tag{5.4}$$

where $t_c$ and $t_r$ represent the collection/counting time and rotation time, respectively. One cycle includes the time needed for one catcher foil to be irradiated, rotated, counted, and rotated to the low, "in-beam", position once more. Within this time the second catcher foil, which began in the high, detector, position, will also have been irradiated and counted in all cycles but the very first.

A plot of $D(t_c$ is given in Figures 5.1 and 5.2 for the experiment and test run cases, respectively. The curves were fit using an exponential function of the form, $y = a + bx + c\rho^x$, where a, b, c, and $\rho$ are cosntants. The peak of this function, i.e. the ideal collection/counting time is located at $x_0 = ln(-b/cln(\rho))/ln(\rho)$ and was found to be at $t_c = 3.7$ minutes for the case of populating the 4.03-MeV excited state in $^{19}$Ne. Similarly, in populating the 5.35-MeV excited state the ideal collection/counting time was also found at 3.7 minutes. The ideal exposure time was not expected to differ greatly between these two cases. The differences between these cases are the transmission coefficients through the gold and the probability of $\alpha$-decay from the 5.35-MeV energy level, which is approximately $10^4$ times greater than that of the 4.03-MeV level. The number of disintegrations between these two cases during the same time frame differs by about four orders of magnitude, which is a direct result of the increased $\alpha$-branching ratio.

### 5.2.2 Beamtime Requirements

A calculation is needed to predict the amount of beamtime that is required to achieve enough detection such that any measurement has a reasonable statistical significance. Using the information determined in Section 5.2.1, i.e., the maximum rate at which $^{15}$O nuclei can be observed, a cross section for the production reaction (which are 30 mb and $2{\cdot}10^{-4}$ mb for the test and experiment cases, respectively [49]) as well as the ideal number measured of total $^{15}$O events, the amount of time needed to perform an accurate experiment can be determined.

For the purposes of counting the number of 511-keV $\gamma$-ray coincidences be-

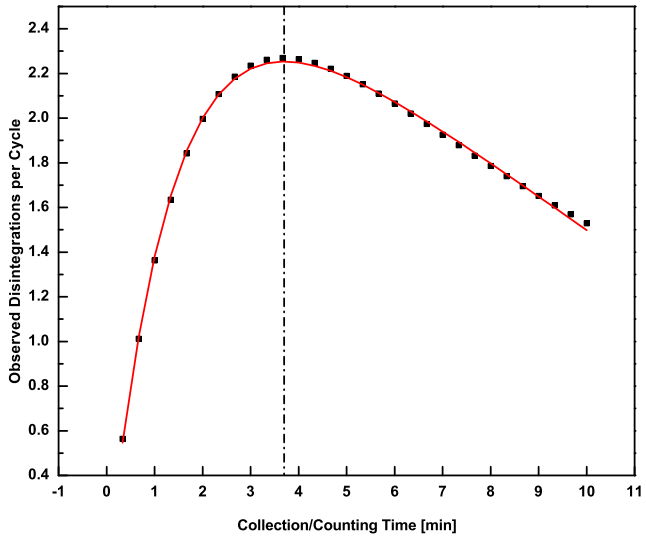


Figure 5.1: Disintegrations per catcher foil rotation cycle as a function of $t_c$ for populating the 4.03-MeV excited state in $^{19}$Ne. The peak location is indicative of the ideal exposure time and was found to be 3.7 minutes.

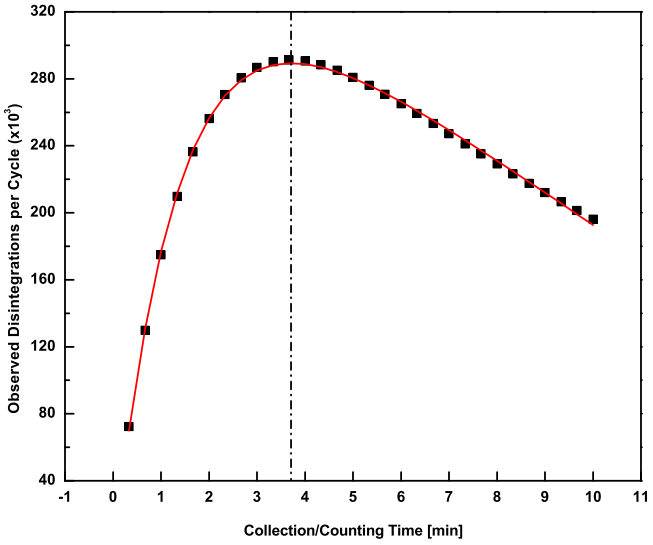


Figure 5.2: Disintegrations per catcher foil rotation cycle as a function of $t_c$ for populating the 5.35-MeV excited state in $^{19}$Ne. Ideal exposure time was found to be 3.7 minutes.

tween the two detectors, the uncertainty associated with observing some number of coincidences is well described by a Binomial Distribution that takes into account the number of trials ($^{15}$O $\beta^+$-decays) and the likelihood of a coincident event taking place. For a likelihood much less than one and a number of $\beta^+$-decays greater than 20 [50], the Binomial Distribution can be simplified as Gaussian distribution [39] with the following form.

$$P(x) = \frac{1}{\sqrt{2\pi\bar{x}}} e^{-\frac{(x-\bar{x})^2}{2\bar{x}}} \tag{5.5}$$

where $x$ represents the number of coincident detections and $\bar{x}$ represents the mean number of coincident detection over many measurements. Within this model the predicted standard deviation ($\sigma$) about the mean is given by,

$$\sigma = \sqrt{\bar{x}} \tag{5.6}$$

In the event that only one measurement is taken (say, one hour long detection period) then the number of coincident events detected ($x$) should be taken as the best estimate of the mean. The range included within $\pm$ 1$\sigma$ about $x$ is said to have a 68% probability of containing the true mean of $x$ and a 99% probability within $\pm$ 2.58$\sigma$. We can increase the statistical significance of a measurement then by extending the duration of a measurement and thus decreasing the fractional standard deviation. The fractional standard deviation is given as $\sqrt{x}/x$ or $1/\sqrt{x}$. Thus for a measurement of 100 coincident events there would be a standard deviation of 10 and a fractional standard deviation of 0.1 (10%). It follows then that there is a 68% chance that the true mean of the measurement lies between 90 and 110 events for that measurement.

For the purposes of this project, a general guideline is used that stipulates that the ideal statistical significance for any given measurement is a fractional standard deviation of 3%[51]. This guideline may be relaxed depending on feasibility and the relative size of other sources of systematic error (cf. $\sim$ 10% uncertainty in Au foil transmission coefficient). To achieve the the 3% uncertainty, however, any given measurement must contain at least 1000 coincident events before being corrected for detection efficiencies. Using this information we can predict the amount of beam-

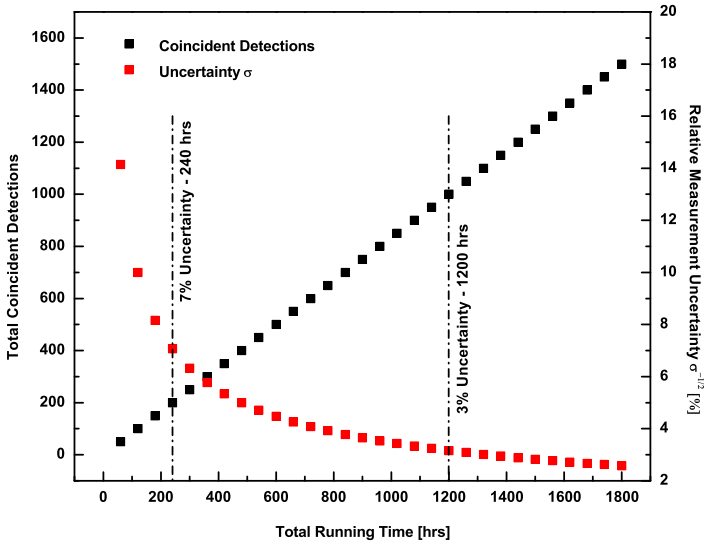


Figure 5.3: Total coincidence detection and the associated statistical uncertainty as a function of total runtime for the 4.03-MeV excited state experiment.

time required to satisfy the statistical constraints. So based on the maximum rates at which $^{15}$O nuclei will $\beta^+$-decay, the 1000 count requirement and the coincident detection probabilities of 0.49% and 0.47%, we require 1200 hours and 4.3 minutes for the experiment and test run cases, respectively. This information is displayed graphically in Figure 5.3 for the experimental case. Since a 1200 hour beamtime is roughly 7 weeks is not feasible, a lower statistical significance could be used to decrease beamtime requirements. Figure 5.3 indicates that a statistical uncertainty of 7% can be achieved with 240 hours of beamtime. This amount of beamtime may be realized within a 10+4 day span to prepare the apparatus, perform background and calibration measurements, as well as complete the 240 hour measurement.

In the event that the time required for reasonable statistics for the measurement is greater than the allotted experiment duration, non-coincidence measurements could also be used. This would consist of using the spectra from both upstream and downstream detectors to evaluate the total $^{15}$O yield that is observed. This method would require a statistical reduction technique to account for double counting that arise from coincident events. Figure 5.4 plots the total upstream/downstream detection, and the relative uncertainties in the measurement, vs. the amount of beamtime

used. This approach would produce measurements with relative uncertainties of 2% and 3% for the upstream and downstream detectors, respectively, after 180 hours of beamtime. An important fact to keep in mind here is that a non-coincident measurement may also contain a greater background at 511-keV, which constrains expected the 2% and 3% uncertainties as upper limits. A non-coincident measurement could be completed, nevertheless, with the ideal statistical uncertainty of 3%, within 7.5+4 days, approximately. The coincidence measurement for the test run case will easily be completed in a 3-day span, and as such, beamtimes and uncertainties for a non-coincidence measurement are not suggested here.

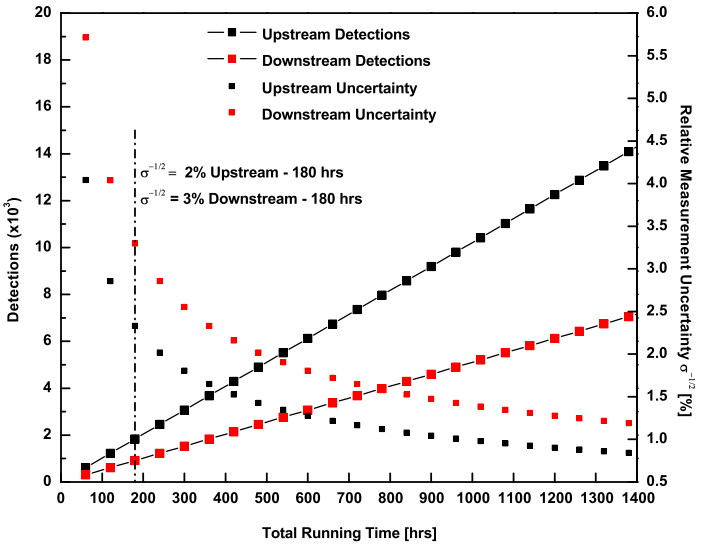


Figure 5.4: Total Upstream and Downstream detections and the associated statistical uncertainty as a function of total runtime for the 4.03-MeV excited state experiment.

## 5.3 Future Work

Following the determination of the experimental parameters that optimize $^{15}$O yield, provided in this thesis, the next phases of this project can be considered. As mentioned previously, the testing phase of this project, in which the 5.35-MeV excited state of $^{19}$Ne is populated, can now proceed. This experiment has already been approved for 2+1 days of beamtime at Argonne National Laboratory (ANL),

but the dates have not yet been finalized.

Assuming the test run proves to be successful in demonstrating the feasibility of the $\beta^+$ activity technique, another request for beamtime to complete a $^{15}$O yield measurement via $\alpha$-decay from the 4.03-MeV excited state will be submitted to the Project Approval Committee (PAC) at ANL. The initial request for time will be made to perform a coincidence measurement that achieves an acceptable statistical significance, i.e. $\sigma \approx 7\%$. If this is not approved then a second request will be made that either has a higher statistical uncertainty or is a non-coincident measurement. Once the beamtime request has been approved the experiment will proceed.

Once the $^{15}$O yield from the 4.03-MeV excited state of interest has been measured, a measurement of the cross section for populating this state must be performed. This measurement will allow for a calculation of the $\alpha$-branching ratio $B_\alpha$ and thus a calculation of the $\alpha$ partial width $\Gamma_\alpha$ for this state. These calculated values will be compared with any previous measurement to check for agreement. This measurement may also be able to validate the accepted order of magnitude estimate of $10^{-4}$ for $B_\alpha$ as well as confirm or refute the only recorded measurement of $B_\alpha = 2.9 \pm 2.1 \cdot 10^{-4}$ made by Tan et al., [26]. The cross section may be measured using the same hydrogen gas cell target as used in the $^{15}$O yield measurements or a solid $CH_2$ target, depending on spatial constraints since reaction products will be detected with Enge Split Pole Magnetic Spectrometer at ANL. This measurement will be technically similar to that of Smith et al., (1993) [52].

If this project is successful in producing a statistically significant measurement of $\Gamma_\alpha$, future work may also include the application of this value in modern hydrodynamic modelling that is used to predict the behaviour of Type I x-ray bursts and other astrophysical phenomena that rely on the $^{15}$O$(\alpha,\gamma)^{19}$Ne reaction for breakout from the HCNO cycles. Once again, these modelling projects are necessary to test and compare our understanding of the physical processes that govern the behaviour and duration of stellar explosions, stellar energy production, and the elemental abundances that are observed in the universe.

Appendix A

# RUNSIM

## A.1 Kinematic Calculation

This section has been created to describe the formalism that gives rise to the kinematic expressions found in the nuclear reaction simulation RUNSIM. Following the two body centre-of-mass frame description given in the text, *Nuclear Physics of Stars* [9]. The lab frame energies, and scattering angles of the recoil product and subsequent daughter product of a decay will be described in terms of beam energy and centre-of-mass scattering angles.

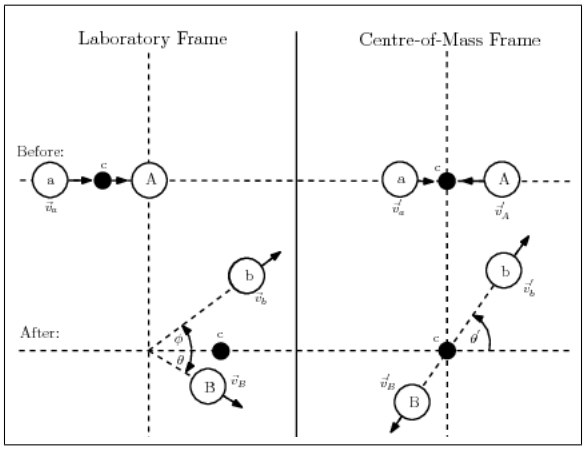


Figure A.1: Kinematic trajectories in two-body reaction before and after the collision.

So we consider a two body reaction A(a,b)B, where A, a, b, and B describe the target, projectile, ejectile, and recoil nucleus, respectively. We consider a stationary target (A), with an incident nucleus (a), projected towards it. By conservation of

momentum in the lab frame we can say that,

$$(m_a + m_A)\vec{v}_c = m_a\vec{v}_a + m_A\vec{v}_A. \tag{A.1}$$

Where $v_c$ is the velocity of the centre-of-mass in the lab frame. Noting that $v_A$ is zero in the lab frame we find that,

$$\vec{v}_c = \frac{m_a}{m_a + m_A}\vec{v}_a. \tag{A.2}$$

We must now describe the conservation of energy in the centre-of-mass frame. Note that centre-of-mass variables are denoted with a prime, e.g. $x^{'}$. This gives rise to a relationship between kinetic energy after the collision, the initial kinetic energy and the reaction $Q$-value.

$$E_a^{'} + m_a c^2 + E_A^{'} + m_A c^2 = E_b^{'} + m_b c^2 + E_B^{'} + m_B c^2 \tag{A.3}$$

With $Q = (m_a + m_A - m_b - m_B)c^2$ we find that,

$$E_f^{'} = Q + E_i^{'}. \tag{A.4}$$

Where $E_i^{'} = E_a^{'} + E_A^{'}$ and $E_f^{'} = E_b^{'} + E_B^{'}$. In keeping with the fact that the controlled variables of the simulation are $E_a$ the beam energy in the lab frame and $\theta^{'}$ the centre-of-mass scattering angle we seek to describe $E_i^{'}$ in terms of these. For this we must first describe the velocity transformation between frames. In general the non-relativistic velocities transform like,

$$\vec{v}^{'} = \vec{v} - \vec{v}_c. \tag{A.5}$$

So applying this transformation to the projectile and target nuclei we find that,

$$\vec{v}_a^{'} = \vec{v}_a - \vec{v}_c \tag{A.6a}$$

$$\vec{v}_A^{'} = \vec{v}_A - \vec{v}_c = -\vec{v}_c. \tag{A.6b}$$

Recall that in eq. (2) an expression for $\vec{v}_c$ was determined. Substituting this ex-

pression here, gives the centre-of-mass frame velocities in terms of the lab frame projectile velocity.

$$\vec{v}_a^{'} = \vec{v}_a - \frac{m_a}{m_a + m_A}\vec{v}_a = \frac{m_A}{m_a + m_A}\vec{v}_a \tag{A.7a}$$

$$\vec{v}_A^{'} = -\frac{m_a}{m_a + m_A}\vec{v}_a \tag{A.7b}$$

We may now find $E_i^{'}$ in terms of the lab frame beam energy by evaluating $E_a^{'}$ and $E_A^{'}$. With $E = \frac{1}{2}mv^2$, the non-relativistic kinetic energy, we have,

$$E_a^{'} = \frac{1}{2}mv_a^{'2} \tag{A.8a}$$

$$E_A^{'} = \frac{1}{2}mv_A^{'2}. \tag{A.8b}$$

Using eq. (7a) and (7b) these now become,

$$E_a^{'} = \frac{1}{2}m_a\left(\frac{m_A}{m_a + m_A}v_a\right)^2 = E_a\left(\frac{m_A}{m_a + m_A}\right)^2 \tag{A.9a}$$

$$E_A^{'} = \frac{1}{2}m_A\left(-\frac{m_a}{m_a + m_A}v_a\right)^2 = E_a\frac{m_a m_A}{(m_a + m_A)^2}. \tag{A.9b}$$

Which gives us,

$$E_i^{'} = E_a^{'} + E_A^{'} = E_a\left(\frac{m_A}{m_a + m_A}\right)^2 + E_a\frac{m_a m_A}{(m_a + m_A)^2}$$

$$E_i^{'} = E_a\frac{m_A^2 + m_a m_A}{(m_a + m_A)^2} \tag{A.10}$$

$$E_i^{'} = E_a\frac{m_A}{m_a + m_A}.$$

We will now undergo a similar process to determine $E_f^{'}$ in terms of the centre-of-mass

recoil energy. In the centre-of-mass frame we require that the total linear momentum must be zero. So after the collision has taken place we can say that,

$$m_b\vec{v_b^{'}} = m_B\vec{v_B^{'}} \; or \; \vec{v_b^{'}} = \frac{m_B}{m_b}\vec{v_B^{'}} \tag{A.11}$$

So it follows that the kinetic energy of the ejectile (b), in the centre-of-mass frame can be given as,

$$E_b^{'} = \frac{1}{2}m_b v_b^2 = \frac{1}{2}m_b\left(\frac{m_B}{m_b}v_B^{'}\right)^2 = E_B^{'}\frac{m_B}{m_b}. \tag{A.12}$$

We now have,

$$E_f^{'} = E_b^{'} + E_B^{'} = E_B^{'}\frac{m_b + m_B}{m_b}. \tag{A.13}$$

Substituting eqs. (10) and (13) into eq. (4) for $E_i^{'}$ and $E_f^{'}$, respectively, we can solve for $E_B^{'}$ in terms of the beam energy. We get that,

$$E_B^{'} = \frac{m_b}{m_b + m_B}\left(Q + E_a\frac{m_A}{m_a + m_A}\right). \tag{A.14}$$

It becomes convenient, at this point, to introduce a variable $\gamma = v_c/v_B^{'}$. We can now evaluate this new variable in terms of the beam energy using eqs. (2) and (14) as well as the fact that $v = \sqrt{\frac{2E}{m}}$.

$$\begin{aligned}
\gamma &= \frac{v_c}{v_B^{'}} = \frac{m_a}{m_a + m_A}\sqrt{\frac{2E_a}{m_a}}\sqrt{\frac{m_B}{2E_B^{'}}} \\
\gamma &= \sqrt{\frac{m_B}{m_a}\left(\frac{m_a}{m_a + m_A}\right)^2\frac{E_a}{E_B^{'}}} \\
\gamma &= \sqrt{\frac{m_B m_a}{m_A m_b}\left(\frac{m_b + m_B}{m_a + m_A}\right)\frac{E_a}{Q(1 + m_a/m_A) + E_a}}
\end{aligned} \tag{A.15}$$

A common approximation is used here that states, $m_a + m_A \approx m_b + m_B$ which gives rise to the simplified expression,

$$\boxed{\gamma = \sqrt{\frac{m_B m_a}{m_A m_b} \frac{E_a}{Q(1 + m_a/m_A) + E_a}}} \tag{A.16}$$

We now turn to the kinetic energy expression for $E_B^{'}$ to generate a relationship between the recoil energy in its centre-of-mass frame and lab frame. As we have already developed an expression for $E_B^{'}$ in terms of the beam energy, we will be able to find $E_B$ in terms of the centre-of-mass scattering angle and the beam energy. So using the kinetic energy definition and eq. (5) for the recoil particle we have,

$$E_B^{'} = \frac{1}{2} m_B (\vec{v}_B^{'})^2 = \frac{1}{2} m_B (\vec{v}_B - \vec{v}_c)^2 = \frac{1}{2} m_B (v_B^2 + v_c^2 - 2 v_B v_c \cos\theta). \tag{A.17}$$

Factoring $v_B^2$ out from the term in parentheses we find that,

$$E_B^{'} = E_B \left( 1 + \left( \frac{v_c}{v_B} \right)^2 - 2 \frac{v_c}{v_B} \cos\theta \right). \tag{A.18}$$

Note here that $\gamma$ can be described as the following,

$$\gamma = \frac{v_c}{v_B^{'}} = \frac{v_c}{v_B} \frac{v_B}{v_B^{'}}. \tag{A.19}$$

Recognizing the fractional term in eq. (18) i.e. $v_c/v_B$, we now know that,

$$\frac{v_c}{v_B} = \gamma \frac{v_B^{'}}{v_B}. \tag{A.20}$$

We already have an ideal expression for $\gamma$ and we can determine and expression for $v_B^{'}/v_B$ by using eq. (5) once more, but rearranged for $\vec{v}_B$. So taking $\vec{v}_B = \vec{v}_B^{'} + \vec{v}_c$ and squaring both sides gives.

$$v_B^2 = v_B^{'2} + v_c^2 - 2 v_B^{'} v_c \cos\theta^{'}. \tag{A.21}$$

Dividing the left and right hand sides of this expression by $v_B^{'2}$.

$$\frac{v_B^2}{v_B^{'2}} = 1 + \frac{v_c^2}{v_B^{'2}} - 2 \frac{v_c}{v_B^{'}} \cos\theta^{'} \tag{A.22}$$

So substituting in $\gamma$ for $v_c/v_B^{'}$ and taking the square root of both sides gives us,

$$\frac{v_B}{v_B^{'}} = \sqrt{1+\gamma^2-2\gamma\cos\theta'}. \tag{A.23}$$

It is important to note that at this point our energy relationship is only dependant on the lab frame recoil scattering angle, but we are seeking a centre-of-mass frame scattering angle dependence, so we need to rewrite $\cos\theta$ in eq. 18 in terms of $\cos\theta^{'}$. This is easily achieved by considering the components of the velocity vectors. By projecting the velocity transformation equation onto the direction $\hat{v}_c$ i.e. the direction of the centre-of-mass velocity vector and also the direction perpendicular to the motion of the centre-of-mass, we can generate a system of equations and solve for $\cos\theta^{'}$. The results is,

$$-v_B^{'}\cos\left(\theta^{'}+\pi\right) = -v_B^{'}\cos\theta^{'} = v_B\cos\theta - v_c \tag{A.24a}$$

$$\textit{and,} \qquad -v_B^{'}\sin\left(\theta^{'}+\pi\right) = v_B^{'}\sin\theta^{'} = v_B\sin\theta. \tag{A.24b}$$

Rearranging for $\cos\theta$ gives,

$$\cos\theta = \frac{v_c}{v_B} - \frac{v_B^{'}}{v_B}\cos\theta^{'} = \gamma\frac{v_B^{'}}{v_B} - \cos\theta^{'}\frac{v_B^{'}}{v_B}. \tag{A.25}$$

Substituting in the reciprocal of eq. (23) here for $v_B^{'}/v_B$, gives us our scattering angle relationship.

$$\cos\theta = \frac{\gamma-\cos\theta^{'}}{\sqrt{1+\gamma^2-2\gamma\cos\theta'}} \tag{A.26}$$

Substituting eqs. (20), (23), and (26) into eq. (18) we finally arrive at our expression for $E_B^{'}$ in terms of $E_B$.

$$E_B^{'} = E_B\left(\frac{1}{1+\gamma^2-2\gamma\cos\theta'}\right) \tag{A.27}$$

We now have two expressions for $E_B^{'}$, eqs. (14) and (27). By equating these and solving for $E_B$ we find,

$$E_B = \frac{m_b m_A}{(m_b + m_B)(m_a + m_A)} \left( Q \left( 1 + \frac{m_a}{m_A} \right) + E_a \right) \left( 1 + \gamma^2 - 2\gamma \cos\theta^{'} \right)$$

$$E_B = \frac{m_b m_A}{(m_b + m_B)(m_a + m_A)} \left( Q \left( 1 + \frac{m_a}{m_A} \right) + E_a \right) \gamma^2 \left( 1 + \frac{1}{\gamma^2} - \frac{2\cos\theta^{'}}{\gamma} \right). \tag{A.28}$$

Expanding $\gamma$ as given by eq. (16), the expression is simplified to the form,

$$E_B = \frac{m_a m_B}{(m_b + m_B)(m_a + m_A)} E_a \left( 1 + \frac{1}{\gamma^2} - \frac{2\cos\theta^{'}}{\gamma} \right). \tag{A.29}$$

This expression reaches its final form by making use of the approximation; $m_a + m_A \approx m_b + m_B$.

$$\boxed{E_B = \frac{m_a m_B}{(m_a + m_A)^2} E_a \left( 1 + \frac{1}{\gamma^2} - \frac{2\cos\theta^{'}}{\gamma} \right).} \tag{A.30}$$

The last quantity that need be determined for the two-body reaction is the final lab frame scattering angle, which is given its simplest form by solving eq. (24a) for $v_B \cos\theta$ and the then dividing eq. 24(b) by the rearranged (24a) such that,

$$\tan\theta = \frac{v_B^{'} \sin\theta^{'}}{v_c - v_B^{'} \cos\theta^{'}} = \frac{\sin\theta^{'}}{\gamma - \cos\theta^{'}} \tag{A.31}$$

Which gives then a lab frame scattering angle $\theta$ as,

$$\boxed{\theta = \arctan\left( \frac{\sin\theta^{'}}{\gamma - \cos\theta^{'}} \right)} \tag{A.32}$$

We have then concluded the derivation of the energy of the recoil particle in the lab frame and now continue with the kinematics of the subsequent decay process that the recoil product undergoes. This decay reaction has the form B(d)D, where d and D describe the decay ejectile and daughter nucleus, respectively.

We will go about this in a very similar fashion to the two-body reaction. Consider the lab frame before the decay takes place; by conservation of momentum we can say that,

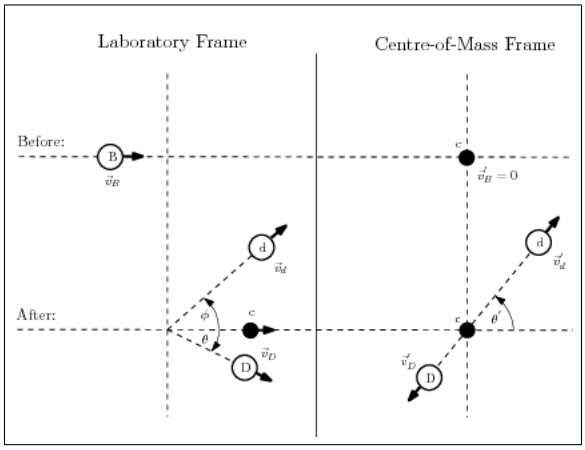


Figure A.2: Kinematic trajectories of decay process before and after it takes place.

$$m_{tot}\vec{v}_c = m_B\vec{v}_B. \tag{A.33}$$

Since in the time before the collision the total mass, described by $m_{tot}$, is only comprised of the recoil particle mass $m_B$. So we must have,

$$\vec{v}_c = \vec{v}_B. \tag{A.34}$$

Using the transformation equation, eq. (5), we can find the velocity of the recoil particle in this secondary centre-of-mass frame.

$$\vec{v}_B^{\,\prime} = \vec{v}_B - \vec{v}_c = \vec{0}. \tag{A.35}$$

We can now consider the time after the decay has taken place. In the centre-of-mass frame the total linear momentum must equal zero and as such we observe,

$$m_d\vec{v}_d^{\,\prime} = m_D\vec{v}_D^{\,\prime} \; or \; \vec{v}_D^{\,\prime} = \frac{m_d}{m_D}\vec{v}_d^{\,\prime} \tag{A.36}$$

So from the definition of non-relativistic kinetic energy and eq. (36b) we find that,

$$E_D^{\prime} = \frac{1}{2}m_D v_D^{\prime 2} \tag{A.37a}$$

$$\textit{and,} \qquad E_d^{'} = \frac{1}{2} m_d v_d^{'2} = \frac{1}{2} m_d \left( \frac{m_d}{m_D} \vec{v}_d^{'} \right)^2 = E_D \frac{m_D}{m_d}. \tag{A.37b}$$

The total kinetic energy after the collision, $E_f^{'}$, can be given by the sum of the kinetic energies of the two decay particles, such that

$$E_f^{'} = E_D^{'} + E_d^{'} = E_D^{'} \left( \frac{m_d + m_D}{m_d} \right). \tag{A.38}$$

By eq. (4), we now have,

$$E_f^{'} = E_B^{'} + Q = \frac{1}{2} m_B (\vec{0})^2 + Q = Q. \tag{A.39}$$

Where by eq. (35), $\vec{v}_B^{'}$ is zero and the Q-value is given by $(m_B - m_d - m_D)$. Using eqs. (38), and (39) we can now describe the energy of the daughter nucleus $E_D^{'}$, entirely by known masses.

$$E_D^{'} = Q \left( \frac{m_d}{m_d + m_D} \right) \tag{A.40}$$

We will build an alternate expression for $E_D^{'}$ in terms of the lab frame energy for the daughter nucleus (D). By using eq. (5) in the definition for the kinetic energy of the daughter nucleus we get,

$$\begin{aligned} E_D^{'} &= \frac{1}{2} m_D (\vec{v}_D^{'})^2 = \frac{1}{2} m_D (\vec{v}_D - \vec{v}_B)^2 = \frac{1}{2} m_D (v_D^2 + v_B^2 - 2 v_D v_B \cos\theta) \\ \textit{and,} \qquad E_D^{'} &= E_D \left( 1 + \left( \frac{v_B}{v_D} \right)^2 - 2 \frac{v_B}{v_D} \cos\theta \right) \end{aligned} \tag{A.41}$$

This expression is clearly very similar to what was seen in the previous case in eq. (18). So from here we seek to rewrite this expression in terms of an analogous $\gamma$ and the centre-of-mass scattering angle, which is again referred to as $\theta^{'}$ here. We define $\gamma$ in a similar way here.

$$\gamma = \frac{v_B}{v_D^{'}} = \sqrt{\frac{2E_B}{m_B}} \sqrt{\frac{m_D}{2E_D^{'}}} \tag{A.42}$$

Using eq. (40),

$$\boxed{\gamma = \sqrt{\frac{m_D}{m_B}\frac{E_B}{Q}\frac{m_d + m_D}{m_d}}} \tag{A.43}$$

Once more, $\gamma$ can be described by,

$$\gamma = \frac{v_B}{v_d^{'}} = \frac{v_B}{v_D}\frac{v_D}{v_D^{'}}, \tag{A.44}$$

and thus

$$\frac{v_B}{v_D} = \gamma\frac{v_D^{'}}{v_D}. \tag{A.45}$$

We can determine $v_D^{'}/v_D$ by applying eq. (5) to the daughter nucleus (D), rearranging for the lab frame velocity and then squaring both sides, as follows.

$$\vec{v}_D = \vec{v}_D^{'} + \vec{v}_B \tag{A.46a}$$

$$v_D^2 = v_D^{'2} + v_B^2 - 2v_D^{'}v_B\cos\theta^{'} \tag{A.46b}$$

$$\left(\frac{v_D}{v_D^{'}}\right)^2 = 1 + \gamma^2 - 2\gamma\cos\theta^{'} \tag{A.46c}$$

$$\frac{v_D}{v_D^{'}} = \sqrt{1 + \gamma^2 - 2\gamma\cos\theta^{'}} \tag{A.46d}$$

We also require that our final energy expression depend on $\theta^{'}$ rather than $\theta$ so we need to rewrite the $\cos\theta^{'}$ factor. To do this we take the transformation equation and project it onto the unit vector in the direction of the recoil particle B, and a unit vector perpendicular to it to obtain,

$$-v_D^{'}\cos\left(\theta^{'} + \pi\right) = -v_D^{'}\cos\theta^{'} = v_D\cos\theta - v_B \tag{A.47a}$$

$$-v_D^{'}\sin\left(\theta^{'} + \pi\right) = v_D^{'}\sin\theta^{'} = v_D\sin\theta \tag{A.47b}$$

Using eqs. (46a), (44), and (45d) we can solve for $\cos\theta$ to find,

$$\cos\theta = \frac{\gamma - \cos\theta'}{\sqrt{1+\gamma^2 - 2\gamma\cos\theta'}} \tag{A.48}$$

Substituting eqs. (44), (45d), and (47) into eq. (41) we find

$$E_D^{'} = E_D\left(\frac{1}{1+\gamma^2-2\gamma\cos\theta'}\right) \tag{A.49}$$

equating eqs. (40) and (48) and solving for $E_D$ we get

$$\begin{aligned} E_D &= \frac{m_d}{m_d+m_D}Q\left(1+\gamma^2-2\gamma\cos\theta'\right) \\ E_D &= \frac{m_d}{m_d+m_D}Q\gamma^2\left(1+\frac{1}{\gamma^2}-\frac{2\cos\theta'}{\gamma}\right) \end{aligned} \tag{A.50}$$

Squaring eq. (42) and substituting into eq. (49) for $\gamma^2$ we find our final energy expression for the daughter nucleus that results from the decay in terms of the beam recoil energy and centre-of-mass scattering angle.

$$\boxed{E_D = \frac{m_D}{m_B}E_B\left(1+\frac{1}{\gamma^2}-\frac{2\cos\theta'}{\gamma}\right)} \tag{A.51}$$

Lastly we need to solve for the scattering angle of the daughter nucleus in the lab frame, the most simplified expression for this is found by using eqs. (46a) an (46b). Solving for $v_D\cos\theta$ in eq. (46a), then dividing eq. (46b) by eq. (46a) we find (like in the two-body reaction case) that,

$$\tan\theta = \frac{v_B^{'}\sin\theta'}{v_c - v_B^{'}\cos\theta'} = \frac{\sin\theta'}{\gamma-\cos\theta'} \tag{A.52}$$

And thus,

$$\boxed{\theta = \arctan\left(\frac{\sin\theta'}{\gamma-\cos\theta'}\right)} \tag{A.53}$$

We may now determine the final lab frame angle between the decay product and the initial beam particle. In the following calculation, the angles found in eqs. (32) and (53) will serve as $\theta_1$ and $\theta_2$, respectively. To recap, $\theta_1$ represents the angle

between the beam particle (a) and the recoil particle (B) and $\theta_2$ describes the angle between the recoil particle and its decay product (D) in the lab frame. It has been shown in Figures 1, and 2 that nuclear reactions occur in planes. Separate events, however, will not necessarily happen in the same plane. So to maintain generality of this article we will assume that the decay process takes place in a plane that is oriented at an angle $\phi$ with respect to the initial. Our task then becomes to represent the velocity of the decay product (D) in the basis vectors in the initial two-body reaction plane and then determine the angle between the beam particle and the decay product.

Consider the following spherical Cartesian coordinate system. We have placed the origin at the lab frame location of the decay itself. We align the vertical (z-axis) with the direction of the recoil particle (B), which we will label $\hat{v}_{B\|}$. We will denote a secondary axis with $\hat{v}_{B\perp}$, and the third axis by $\hat{x}$.

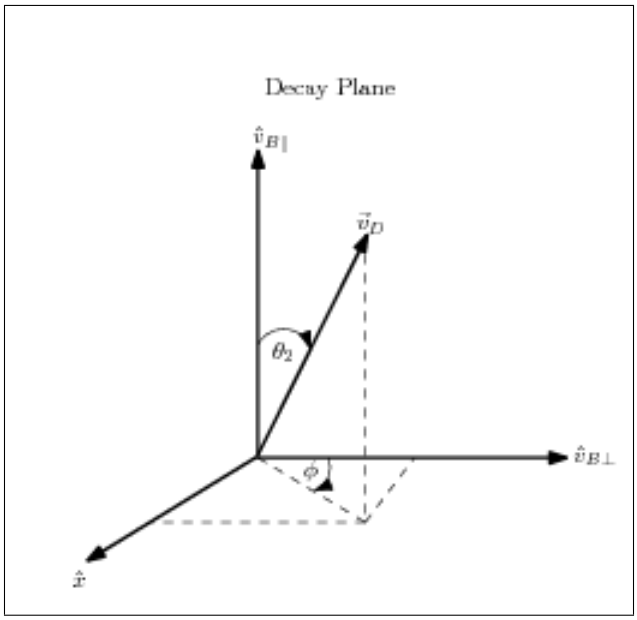


Figure A.3: Coordinate system of the decay process with axes corresponding to the recoil direction.

We know that the nucleus (D) is emitted at an angle $\theta_2$ relative to the direction of (B). The angle $\phi$ describes the difference in orientation between the two planes as the initial plane may be spanned by the constructed vectors $\hat{v}_{B\|}$ and $\hat{v}_{B\perp}$. So from this coordinate system we can describe $\hat{v}_D = \frac{\vec{v}_D}{|(v_D)|}$ as,

$$\hat{v}_D = \cos\theta_2 \hat{v}_{B\parallel} + \sin\theta_2 \cos\phi \hat{v}_{B\perp} + \sin\theta_2 \sin\phi \hat{x}. \tag{A.54}$$

If we consider the initial plane with the beam particle velocity $\vec{v}_a$ oriented along the y-axis we have,

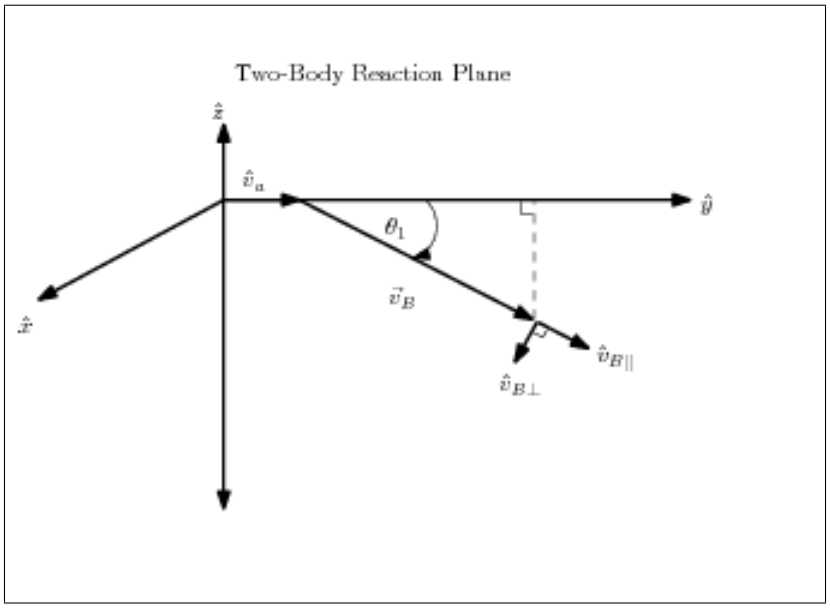


Figure A.4: Coordinate system of the two-body reaction process.

Using this coordinate system we can define $\hat{v}_{B\parallel}$ and $\hat{v}_{B\perp}$ in terms of the basis vectors of the initial plane. Clearly then $\hat{v}_B$ or $\hat{v}_{B\parallel}$ is given by,

$$\hat{v}_{B\parallel} = \cos\theta_1 \hat{y} - \sin\theta_1 \hat{z}. \tag{A.55}$$

To ensure orthogonality between $\hat{v}_{B\parallel}$ and $\hat{v}_{B\perp}$, we can construct $\hat{v}_{B\perp}$ by inspection as,

$$\hat{v}_{B\perp} = \sin\theta_1 \hat{y} + \cos\theta_1 \hat{z}. \tag{A.56}$$

Substituting eqs. (55) and (56) into eq. (54), we can re-write $\hat{v}_D$ in terms of the initial plane basis vectors.

$$\hat{v}_D = \cos\theta_2 \left(\cos\theta_1 \hat{y} - \sin\theta_1 \hat{z}\right) + \sin\theta_2 \cos\phi \left(\sin\theta_1 \hat{y} + \cos\theta_1 \hat{z}\right) + \sin\theta_2 \sin\phi \hat{x} \tag{A.57}$$

To find the angle between $\hat{v}_a$ and $\hat{v}_D$, the final lab frame exit angle $\theta_f$, we simply take an inner product between the two unit vectors.

$$\hat{v}_a \cdot \hat{v}_D = \cos\theta_f = \cos\theta_1 \cos\theta_2 + \sin\theta_1 \sin\theta_2 \cos\phi \tag{A.58}$$

Which can be solved to give,

$$\boxed{\theta_f = \arccos\left(\cos\theta_1 \cos\theta_2 + \sin\theta_1 \sin\theta_2 \cos\phi\right).} \tag{A.59}$$

With this we have then derived all calculated vales contained in the 'kinematics' subroutine of the simulation program RUNSIM. Application these expressions to the $^{1}$H($^{19}$F,$n$)$^{19}$Ne($\alpha$)$^{15}$O reaction gives the energy-scattering angle relationships shown in Figure A.5. It can be seen that the $^{19}$Ne* nuclei are emitted at angles less than 0.34° and similarly $^{15}$O nuclei are emitted at angles less that 1.43°. Figure A.5 demonstrates that populating excited states of $^{19}$Ne with an inverse reaction results in reaction products that are forward focused in the laboratory frame.

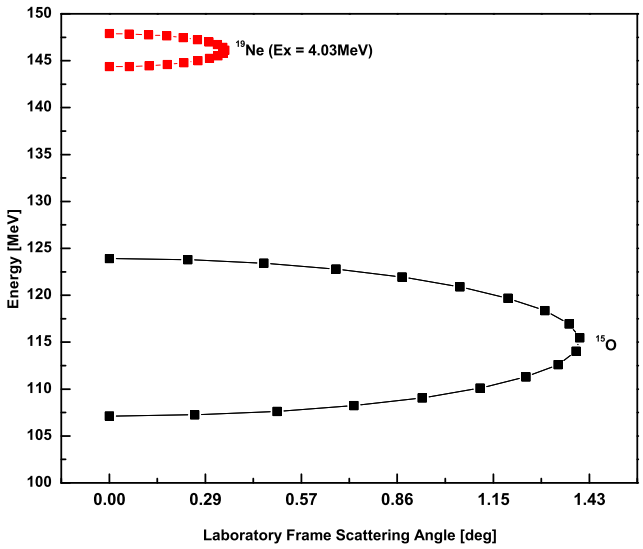

## A.2 Fits of TRIM Range Data

Once range data was collected from TRIM for both $^{15}$O and $^{19}$Ne$_{g.s.}$ nuclei at the maximum and minimum energies, the data were plotted in a histogram and fit using the Origin7 data processing software. The best fits were generally achieved using the 'Extreme' peaks function that is defined as,

$$y(x) = y_0 + Ae^{-e^{-(x-xc)/w}-(x-xc)/w+1}. \tag{A.60}$$

Where $y_0$ is the baseline for the curve, $A$ represents the peak height above the baseline, "$xc$" represents the centroid position, and $w$ is the curve width. Values for the centroid positions and widths are recorded for each ion at each energy level. A linear fit between values at the maximum and minimum energies provide a means for which ranges can be determined for ions with any energy. The actual fitting results for the experiment and test run are tabularized below.

| Energy [MeV] | Ion | xc | w |
|---|---|---|---|
| 104.2 | $^{15}$O | 82458.84473 | 2670.09137 |
| 121.6 | $^{15}$O | 13793.00405 | 2878.61406 |
| 140.2 | $^{19}$Ne$_{g.s.}$ | 99832.85512 | 2771.52576 |
| 140.3 | $^{19}$Ne$_{g.s.}$ | 90436.51174 | 2839.19294 |

Table A.1: Range fitting data for experiment run where the 4.03-MeV excited state of $^{19}$Ne is populated.

| Energy [MeV] | Ion | xc | w |
|---|---|---|---|
| 116.5 | $^{15}$O | 172414.47113 | 2802.28742 |
| 147 | $^{15}$O | 40106.19217 | 3208.36736 |
| 164.8 | $^{19}$Ne$_{g.s.}$ | 172756.40585 | 2939.00485 |
| 168.1 | $^{19}$Ne$_{g.s.}$ | 163841.92384 | 3019.30281 |

Table A.2: Range fitting data for test run where the 5.35-MeV excited state of $^{19}$Ne is populated.

# Bibliography


[1] C. E. Rolfs and W. S. Rodney. *Cauldrons in the Cosmos*. University of Chicago Press, 1988.

[2] A. S. Eddington. The internal constitution of the stars. *The Observatory*, 43, 1920.

[3] G. W. Collins, II. The virial theorem in stellar astrophysics. In *Astronomy and Astrophysics Series Volume 7*. Pachart Publishing House, Tuscan, Arizona, 1978.

[4] D. B. Guenther. Age of the sun. *Ap. J.*, 339, 1989.

[5] F. W. Aston. The Atoms of Matter; their Size, Number, and Construction. *Nat.*, 110, 1922.

[6] H. A. Bethe. Energy Production in Stars. *Phys. Rev.*, 55, 1939.

[7] E. M. Burbidge, G. R. Burbidge, W. A. Fowler, and F. Hoyle. Synthesis of the Elements in Stars. *Rev. Mod. Phys.*, 29, 1957.

[8] A.G.W. Cameron. *Stellar evolution, nuclear astrophysics, and nucleogenesis*. Atomic Energy of Canada Ltd., Chalk River, Ontario, 1957.

[9] Christian Iliadis. *Nuclear Physics of Stars*. Wiley-VCH Verlag GmbH, 2008.

[10] M. Wiescher, J. Gorres, E. Uberseder, G. Imbriani, and M. Pignatari. The Cold and Hot CNO Cycles. *Annu. Rev. Nucl. Part. Sci.*, 60, 2010.

[11] E. E. Salpeter. Nuclear Reactions in the Stars. I. Proton-Proton Chain. *Phys. Rev.*, 88, 1952.

[12] R. K. Wallace and S. E. Woosley. Explosive hydrogen burning. *Ap. J. Suppl. Ser.*, 45, 1981.

[13] A. Parikh, J. José, G. Sala, and C. Iliadis. Nucleosynthesis in Type I X-ray bursts . *Prog. Part. Nucl. Phys.*, 69, 2013.

[14] J. José and C. Iliadis. Nuclear astrophysics: the unfinished quest for the origin of the elements. *Rep. Prog. Phys.*, 74(9):096901, 2011.

[15] B. Davids, R. H. Cyburt, J. José, and S. Mythili. The Influence of Uncertainties in the 15O($\alpha$, $\gamma$)19Ne Reaction Rate on Models of Type I X-Ray Bursts. *Ap. J.*, 735, 2011.

[16] L. Maraschi and A. Cavaliere. X-Ray Bursts of Nuclear Origin. In *Highlights of Astronomy*. Springer Netherlands, 1977.

[17] S. E. Woosley and R. E. Taam. Gamma-ray bursts from thermonuclear explosions on neutron stars. *Nat.*, 263, 1976.

[18] M. Wiescher, J. Görres, and H. Schatz. TOPICAL REVIEW: Break-out reactions from the CNO cycles. *J. Phys. G: Nucl. Part. Phys.*, 25, 1999.

[19] J. L. Fisker, Tan W. P., J. Grres, M. Wiescher, and R. L. Cooper. The 15O($\alpha$,$\gamma$)19Ne Reaction Rate and the Stability of Thermonuclear Burning on Accreting Neutron Stars. *Ap. J.*, 665, 2007.

[20] O. Koike, M.-a. Hashimoto, R. Kuromizu, and S.-i. Fujimoto. Final Products of the rp-Process on Accreting Neutron Stars. *Ap. J.*, 603, 2004.

[21] P. V. Magnus, M. S. Smith, A. J. Howard, P. D. Parker, and A. E. Champagne. Measurement of $^{15}$O($\alpha$,$\gamma$)$^{19}$Ne resonance strengths. *Nucl. Phys. A*, 506, 1990.

[22] A. M. Laird, S. Cherubini, A. N. Ostrowski, M. Aliotta, T. Davinson, A. Di Pietro, P. Figuera, W. Galster, J. S. Graulich, D. Groombridge, J. Hinnefeld, M. Lattuada, P. Leleux, L. Michel, A. Musumarra, A. Ninane, M. G. Pellegriti, A. C. Shotter, Spitaleri, A. Tumino, J. Vervier, and P. Woods. Indirect study of the astrophysically important $^{15}$O($\alpha$,$\gamma$)$^{19}$Ne reaction through $^{2}$H($^{18}$Ne,$^{19}$Ne)$^{1}$H. *Phys. Rev. C*, 66:048801, 2002.

[23] K. E. Rehm, A. H. Wuosmaa, C. L. Jiang, J. Caggiano, J. P. Greene, A. Heinz, D. Henderson, R. V. F. Janssens, E. F. Moore, G. Mukherjee, R. C. Pardo, T. Pennington, J. P. Schiffer, R. H. Siemssen, M. Paul, L. Jisonna, and R. E. Segel. Branching ratio $\Gamma_\alpha/\Gamma_\gamma$ of the 4.033 MeV $3/2^+$ state in $^{19}$Ne. *Phys. Rev. C*, 67:065809, 2003.

[24] B. Davids, A. M. van den Berg, P. Dendooven, F. Fleurot, M. Hunyadi, M. A. de Huu, K. E. Rehm, R. E. Segel, R. H. Siemssen, H. W. Wilschut, H. J. Wörtche, and A. H. Wuosmaa. $\alpha$-decay branching ratios of near-threshold states in $^{19}$Ne and the astrophysical rate of $^{15}$O($\alpha$,$\gamma$)$^{19}$Ne. *Phys. Rev. C.*, 67:012801, 2003.

[25] D. W. Visser, J. A. Caggiano, R. Lewis, W. B. Handler, A. Parikh, and P. D. Parker. Particle decay branching ratios for states of astrophysical importance in $^{19}$Ne. *Phys. Rev. C*, 69:048801, 2004.

[26] W. P. Tan, J. L. Fisker, J. Görres, M. Couder, and M. Wiescher. $^{15}O(\alpha,\gamma)^{19}Ne$ Breakout Reaction and Impact on X-Ray Bursts. *Phys. Rev. Lett.*, 98:242503, 2007.

[27] M. Wiescher, F. Kaeppeler, and K. Langanke. Critical Reactions in Contemporary Nuclear Astrophysics. In *Ann. Rev. Astron. Astrophys.*, volume 50. Annual Reviews, Palo Alto, CA, 2012.

[28] D. D. Clayton. *Principles of stellar evolution and nucleosynthesis*. University of Chicago press, 1968.

[29] G. Gamow. Zur Quantentheorie des Atomkernes. *Z. Phys.*, 51, 1928.

[30] Z. Q. Mao, H. T. Fortune, and A. G. Lacaze. Resonant Rate for $^{15}O(\alpha,\gamma)^{19}Ne$. *Phys. Rev. Lett.*, 74, 1995.

[31] F. de Oliveira, A. Coc, P. Aguer, C. Angulo, G. Bogaert, J. Kiener, A. Lefebvre, V. Tatischeff, J.-P. Thibaud, S. Fortier, J. M. Maison, L. Rosier, G. Rotbard, J. Vernotte, M. Arnould, A. Jorissen, and N. Mowlavi. Comparison of low-energy resonances in $^{15}N(\alpha,\gamma)^{19}F$ and $^{15}O(\alpha,\gamma)^{19}Ne$ and related uncertainties. *Phys. Rev. C*, 55, 1997.

[32] W. P. Tan, J. Görres, M. Beard, M. Couder, A. Couture, S. Falahat, J. L. Fisker, L. Lamm, P. J. LeBlanc, H. Y. Lee, S. O'Brien, A. Palumbo, E. Stech, E. Strandberg, and M. Wiescher. Measurement of the decay branching ratios of the $\alpha$-unbound states in $^{19}Ne$ and the $^{15}O(\alpha,\gamma)$ reaction rate. *Phys. Rev. C*, 79:055805, 2009.

[33] X. D. Tang, K. E. Rehm, I. Ahmad, C. R. Brune, A. Champagne, J. P. Greene, A. Hecht, D. J. Henderson, R. V. F. Janssens, C. L. Jiang, L. Jisonna, D. Kahl, E. F. Moore, M. Notani, R. C. Pardo, N. Patel, M. Paul, G. Savard, J. P. Schiffer, R. E. Segel, S. Sinha, and A. H. Wuosmaa. Determination of the E1 component of the low-energy $^{12}C(\alpha,\gamma)^{16}O$ cross section. *Phys. Rev. C*, 81:045809, 2010.

[34] R. Kanungo, T. K. Alexander, A. N. Andreyev, G. C. Ball, R. S. Chakrawarthy, M. Chicoine, R. Churchman, B. Davids, J. S. Forster, S. Gujrathi, G. Hackman, D. Howell, J. R. Leslie, A. C. Morton, S. Mythili, C. J. Pearson, J. J. Ressler, C. Ruiz, H. Savajols, M. A. Schumaker, I. Tanihata, P. Walden, and S. Yen. Lifetime of $^{19}Ne^*$(4.03 MeV). *Phys. Rev. C*, 74:045803, 2006.

[35] W. P. Tan, J. Görres, J. Daly, M. Couder, A. Couture, H. Y. Lee, E. Stech, E. Strandberg, C. Ugalde, and M. Wiescher. Lifetime of the astrophysically important 4.03-MeV state in $^{19}Ne$. *Phys. Rev. C*, 72:041302, 2005.

[36] S. Mythili, B. Davids, T. K. Alexander, G. C. Ball, M. Chicoine, R. S. Chakrawarthy, R. Churchman, J. S. Forster, S. Gujrathi, G. Hackman, D. Howell, R. Kanungo, J. R. Leslie, E. Padilla, C. J. Pearson, C. Ruiz, G. Ruprecht,

M. A. Schumaker, I. Tanihata, C. Vockenhuber, P. Walden, and S. Yen. Lifetimes of states in Ne19 above the O15+$\alpha$ breakup threshold. *Phys. Rev. C*, 77:035803, 2008.

[37] Goodfellow inc. http://goodfellowinc.com/en/, 2013.

[38] J. S. Lilley. *Nuclear Physics: Principles and Applications.* Wiley, 2001.

[39] G. F. Knoll. *Radiation Detection and Measurement - Second Edition.* Wiley, 1989.

[40] F. Ajzenberg-Selove. Energy levels of light nuclei A = 1315. *Nuclear Physics A*, 523, 1991.

[41] P. Schontanus. *SCIONIX.* SCIONIX HOLLAND B.V., 1998.

[42] W. R. Leo. *Techniques for Nuclear and Particle Physics Experiments.* Springer-Verlag, 1987.

[43] J. D. Tuli. *Nuclear Wallet Cards.* National Nuclear Data Center, 2005.

[44] R.R. Finck, K. Lidn, and R.B.R. Persson. In situ measurements of environmental gamma radiation by the use of a Ge(Li)-spectrometer. *Nucl. Instrum. Meth.*, 135, 1976.

[45] J.F. Ziegler, J.P. Biersack, and M.D. Ziegler. *SRIM - The Stopping and Range of Ions in Matter.* SRIM Co., 2008.

[46] S. Agostinelli, J. Allison, K. ea Amako, J. Apostolakis, H. Araujo, P. Arce, M. Asai, D. Axen, S. Banerjee, G. Barrand, et al. GEANT4: a simulation toolkit. *Nucl. Instrum. Meth. Phys. Res. A*, 506, 2003.

[47] J.R. Prescott and G.H. Narayan. Electron responses and intrinsic line-widths in NaI(Tl). *Nucl. Instr. Meth.*, 75, 1969.

[48] M. Moszyski, J. Zalipska, M. Balcerzyk, M. Kapusta, W. Mengesha, and J.D. Valentine. Intrinsic energy resolution of NaI(Tl). *Nucl. Instr. Meth. Phys. Res. A*, 484, 2002.

[49] J.G. Jenkin, L.G. Earwaker, and E.W. Titterton. The F19(p, n)Ne19 reaction between 5 and 11 MeV. *Nucl. Phys. A*, 44, 1963.

[50] W. Feller. *An Introduction to Probability and Its Application, 2nd Ed.* Wiley, New York, 1957.

[51] A. Chen. Private communication, 2013.

[52] M. S. Smith, P. V. Magnus, K. I. Hahn, R. M. Curley, P. D. Parker, T. F. Wang, K. E. Rehm, P. B. Fernandez, S. J. Sanders, A. Garcia, and E. G. Adelberger. Gamma width of $^{14}O^{*}$(5.17 MeV) and the stellar $^{13}N$(p,$\gamma$)$^{14}$O reaction rate. *Phys. Rev. C*, 47, 1993.